Summer 7-23-2019

Assessing and Mitigating Impacts of Electric Vehicles on Active Distribution Systems

Dima Alame
University of Windsor

Assessing and Mitigating Impacts of Electric Vehicles on Active Distribution Systems

By

Dima Alame

A Thesis
Submitted to the Faculty of Graduate Studies
through the Department of Electrical and Computer Engineering
in Partial Fulfillment of the Requirements for
the Degree of Master of Applied Science
at the University of Windsor

Windsor, Ontario, Canada

2019

Assessing and Mitigating Impacts of Electric Vehicles on Active Distribution Systems

by

Dima Alame

APPROVED BY:

—————————————————————
A. A. Asfour
Department of Civil and Environmental Engineering

—————————————————————
B. Balasingam
Department of Electrical and Computer Engineering

—————————————————————
M. A. Azzouz Abdelkhalek, Co-Advisor
Department of Electrical and Computer Engineering

—————————————————————
N. Kar, Co-Advisor
Department of Electrical and Computer Engineering

July 23, 2019

DECLARATION OF CO-AUTHORSHIP / PREVIOUS PUBLICATION

I. Co-Authorship

I hereby declare that this thesis incorporates material that is result of joint research, as follows:

Chapters 3 and 4 of the thesis were co-authored with Dr. Abdelkhalek and Dr. Kar. In all cases, the key ideas, primary contributions, data analysis, interpretation, and writing were performed by the author, and the contribution of co-authors was providing supervision and guidance.

I am aware of the University of Windsor Senate Policy on Authorship and I certify that I have properly acknowledged the contribution of other researchers to my thesis, and have obtained written permission from each of the co-authors to include the above materials in my thesis.

I certify that, with the above qualification, this thesis, and the research to which it refers, is the product of my own work.

II. Previous Publication

This thesis includes two original papers that have been previously published in peer reviewed journals, as follows:

Thesis Chapter	Publication title/full citation	Publication status
Chapter 3	D. Alame, M. Azzouz, and N. C. Kar, "Impact Assessment of Electric Vehicle Charging on Distribution Transformers Including State-of-Charge," *Midwest Symp. Circuits Syst.*, vol. 2018-Augus, no. 2, pp. 607–610, 2019.	*Published*
Chapter 3 & 4	D. Alame, M. A. Azzouz, and N. C. Kar, "Assessing the Impacts of Electric Vehicle Battery Charging on Distribution Transformers and on Distribution Systems," in *Proceedings of 2018 Energy & Sustainability Symposium*, 2018, pp. 1–8.	*Published*

I certify that I have obtained a written permission from the copyright owners to include the above published materials in my thesis. I certify that the above material describes work completed during my registration as a graduate student at the University of Windsor.

III. General

I declare that, to the best of my knowledge, my thesis does not infringe upon anyone's copyright nor violate any proprietary rights and that any ideas, techniques, quotations, or any other material from the work of other people included in my thesis, published or otherwise, are fully acknowledged in accordance with the standard referencing practices. Furthermore, to the extent that I have included copyrighted material that surpasses the bounds of fair dealing within the meaning of the Canada Copyright Act, I certify that I have obtained a written permission from the copyright owners to include such materials in my thesis.

I declare that this is a true copy of my thesis, including any final revisions, as approved by my thesis committee and the Graduate Studies office, and that this thesis has not been submitted for a higher degree to any other University or Institution.

ABSTRACT

The transportation sector is expected to undergo a worldwide shift to zero-carbon emission automobiles. Major research advancements and government policies have been addressing the financial and technical barriers to electric vehicle (EV) use. Battery packs constitute an important component of EV technology. Improvements in battery pack technology are leading to lower battery cost, higher battery density, and increased driving range, making EVs more appealing to the consumers. On the other hand, EV charging loads can cause power quality issues such as harmonic distortion, voltage drop, power unbalance, power losses and transformer aging. EV increased charging load is urging the need of assessing its negative impacts on the grid to protect power system components. A comparison of the impacts of different levels of EV charging on the grid can allow EV users and utilities to understand the risks associated with their choices. Harmonic distortion due to nonlinear devices can be evaluated using harmonic power flow methods. Decoupled harmonic power flow technique is widely used in power systems analysis due to its simplicity and computational efficiency.

Mitigation techniques to reduce harmonic impacts on the grid are crucial for power system reliability and maintenance. Incorporating distributed generation (DG) units into the network can achieve harmonic compensation of EV charging. A genetic algorithm is proposed to determine the current harmonic spectrum of each DG unit, accomplishing an optimal harmonic compensation of EV charging. DG integration improves grid power quality and voltage profile. It also helps in reducing voltage and current disturbances produced by EV loads.

DEDICATION

"There come *very* few individuals in life that awaken our *very* inner sense."

My research contributions are dedicated to my mother and my brother.

ACKNOWLEDGEMENTS

TABLE OF CONTENTS

LIST OF TABLES

LIST OF FIGURES

CHAPTER 1

INTRODUCTION

1.1 Overview

With Ontario's Climate Change Action Plan, the transition to low-carbon technologies could be achieved smoothly [1]. This action plan offers programs and incentives to motivate households and industries to help in this transition. The scarcity of electric vehicle (EV) charging infrastructure is an important limiting factor of EV demand. In this regard, the province planned to set a four-year free overnight EV charging program for residential clients since 2017. It also intended to invest in increasing the accessibility of charging stations. According to studies, electric vehicles available in Canada can sufficiently cover 90% of the daily driving needs of the population [2].

The predicted increase in the adoption of EV cars will potentially cause a rise in EV charging load demand. An overall target of a 50% reduction in greenhouse gas emissions produced due to global energy is set by the *Energy Technology Perspectives 2010* BLUE Map to be reached by 2050 [3]. The rapid progression and high penetration rates of EV/ Plug-in Hybrid Electric Vehicle (PHEV) technologies for a light-duty vehicle is necessary to achieve the BLUE Map's target. The sales of EVs are expected to reach 9 million while PHEVs are expected to attain 25 million by 2030. Both vehicle types are each projected to reach 50 million sales annually by 2050. Figure 1 shows the annual light-duty vehicle sales based on technology type according to the BLUE Map scenario.
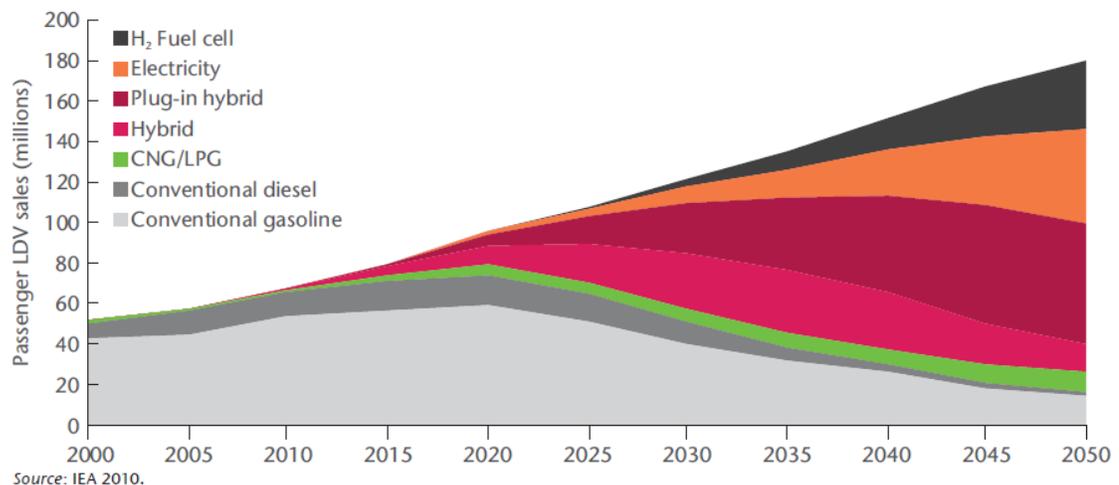
Fig. 1.1 Annual light-duty vehicle sales per technology type, BLUE Map scenario [3].

Due to the non-linearity nature of battery charging, EVs induce transformer losses and temperature to rise, and thus its lifetime to decrease [4]. Harmonics generated by non-linear loads result in reduced power factor and lower performance of the power system. Consequently, the quality of power supplied by the grid suffers. Evaluating the effects of current harmonics on the network is crucial to ensure grid reliability and safety [5].

Renewable energy-based distributed generator (DG) technology have also gained popularity due to the high electricity cost. Solar photovoltaic (PV) systems represent one worldwide attractive residential and commercial application that has witnessed recent technological advancements. Since PV-based DGs can generate harmonics, their integration into the network can compensate the harmonic components produced by EV charging loads [6]. The system distortion with the presence of PV-based DGs and EV loads can be evaluated to ensure network reliability.

1.2 Objectives

Modeling and quantification of EV negative impacts on distribution transformers (DTs) are presented in this work. Transformer loss increase, temperature rise, and lifetime reduction due to current harmonics generated by EV battery charging are calculated. A sample 1500 kVA DT is used to evaluate the effects of additional EV charging load along with other conventional loads. System distortion due to the presence of plug-in electric vehicle (PEV) charging lots is evaluated using a 33-bus radial distribution system (DS) consisting of different types of linear loads including residential, commercial and industrial. Decoupled Harmonic Power Flow (DHPF) technique is implemented to obtain the bus voltage profile at each harmonic order. Voltage total harmonic distortion (THD) is calculated at each bus to determine if the distortion violates the limits imposed by the standards. The harmonic currents through the substation transformer are also obtained and the current distortion is calculated.

The integration of PV-based DGs into the system provides a harmonic compensation technique, through their interfacing inverters, in the presence of PEV loads. A Genetic Algorithm (GA) is proposed to find the optimal harmonic spectrum of each PV-based DG unit in order to minimize the value of the voltage THD occurring at the bus, where the highest disturbance takes place, and the current THD value at the substation transformer.

2

A comparative analysis of the results is performed to show the benefits of incorporating PV-based DGs into the distribution network.

Evaluating the negative impacts of the projected rise in EV charging loads is important to maintain the safe operation, reliability, and high performance of power system components. Understanding the risks associated with the increase of EV applications allows governments and utilities to take safety measurements to prevent high technical and economical challenges [4]. An affordable and practical mitigation technique is essential to reduce deterioration on transformers' lifetime and grid's power quality.

1.3 Novelties and Contributions

The impacts of EV battery charging on distribution transformers are modeled and quantified using different levels of commercially-used battery chargers. Harmonic spectrums resulting from EV battery charging vary depending on the charger's level and design. When purchasing EV chargers, consumers should be aware of the harmonic impacts associated with the charger and consider the severity of the effects in their investment choice.

The state-of-charge (SOC) influences the THD of charging current, increasing the THD, and decreasing the magnitude of the distorted current throughout the charging cycle [7]. The effect of SOC is considered in the harmonic spectrums through applying weighted arithmetic mean on time-variant harmonic order magnitudes. Including the effect of SOC in the harmonic distribution improves the accuracy of the harmonic spectrum of EV battery chargers, and thus enhances the accuracy of the harmonic impact assessment on DTs.

The study is extended to assess harmonic distortion of EV battery charging on distribution systems. THD of voltage is determined at each bus of the IEEE 33-bus benchmark DS to measure voltage distortion due to EV charging. Harmonic current profile at the system's main substation transformer is also obtained to measure current THD. PV-based DGs are connected to the system to reduce voltage and current distortions on the network. The harmonic current values injected by each PV-based DG unit are optimized using the GA algorithm. THD of voltage at each bus and THD of current at the substation transformer

are then measured for a comparative analysis. An overview of this study is provided in Fig. 1.2.
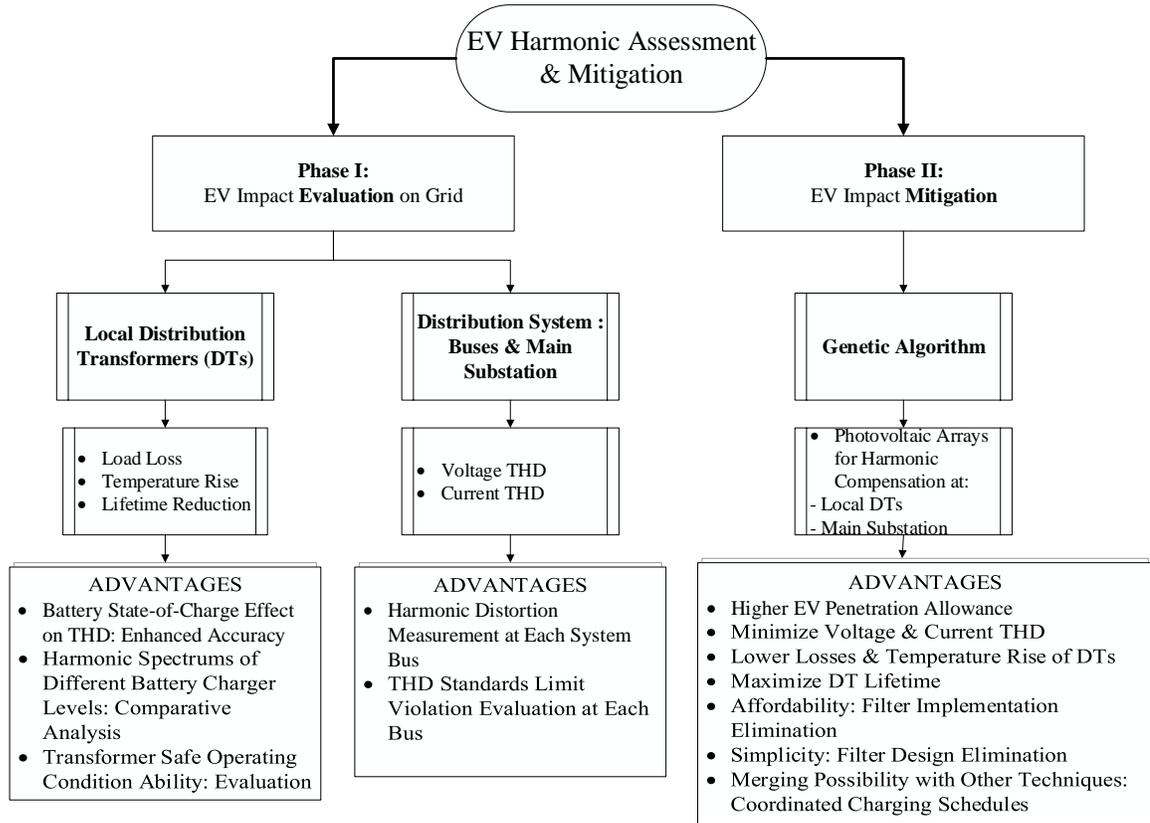
Fig. 1.2 Overview of assessing and mitigating the impacts of electric vehicles on active distribution systems.

1.4 Structure of the Thesis

Chapter 2 provides a literature and background review including EV technology history and trend, a review of different electrified vehicle powertrain architectures, EV battery charging and background study on its impacts on distribution transformers and distribution systems, DHPF algorithm technique to solve the harmonic power flow of non-linear loads, and mitigation techniques for harmonic compensation.

Chapter 3 discusses EV battery charging impacts on the main power system component: DT. It briefly explains the harmonic components generated by non-linear equipment and devices, then proposes a per-unit (p.u.) model of transformer load losses, temperature rise, and lifetime reduction. The impacts are first calculated in the absence of EV loads and then compared with the effects of a single-phase Level I/II charging at 20% EV penetration level. Then, the assessment is performed to compare the impacts due to three-phase Level

III charging with the ones of single-phase Level I/II charging including the state-of-charging effect on the harmonic spectrum.

Chapter 4 presents the effects of EV charging on the distribution system. It includes harmonic power flow analysis to estimate the voltage harmonic disturbance at each bus and the current distortion through the main substation transformer. The assessment is performed in both cases: Level III and Level I/II chargers.

Chapter 5 proposes a compensation technique using PV-based DGs to compensate for the adverse impacts of EV harmonic currents on active distribution networks (ADNs). PV-based DGs are attached at certain buses, and their harmonic spectrums are estimated using the GA algorithm to minimize voltage THD and current THD through the main substation.

Chapter 6 summarizes the results of this study and offers potential future work in the field of harmonic assessment and mitigation.

CHAPTER 2

LITERATURE REVIEW

2.1 EV History and Trend

EV technology has been regarded as an alternative transportation type to combustion-engine vehicles to achieve greenhouse gas emissions reduction goals. Different automotive manufacturers around the world are launching a variety of new vehicle concepts and technologies into the transportation market. Research advancements have resolved major bottlenecks associated with the size, weight, cost, and driving range of EVs [8]. More than 350 electric cars were introduced worldwide by different-sized companies between the years of 2002 and 2012. During this period, manufacturers in different regions of the world introduced specific vehicle segmentation, including executive, luxury and sports hybrid EVs in Europe and sport utility vehicles in the U.S. Battery electric vehicles (BEVs) are limited to small vehicle segment due to expensive production battery costs, high weight, and low energy density. EVs including fuel cell electric, pure battery-electric and hybrid-electric (HEV), and their powertrain concept development have an important history in the automotive field. Electrification of automobiles has become a vital component in the propulsion strategies of automakers around the world to lower fuel consumption, reduce climate change caused by greenhouse gas emissions and increase energy security through variation of the available energy sources [9]. Global automakers are investing in the EV sector, including Ford Motor Company that planned to increase its investments in EVs to reach $11 billion by 2022 and have 40 hybrid and fully EVs in its global lineup [10].

Hybrid Electric Vehicles, Fuel Cell-based vehicles, and EVs are gaining popularity in the automotive sector. These technologies are evolving and are predicted to completely modify the perspective of the automotive industry, offering an alternative to gasoline vehicles. HEVs and PHEVs include both, an internal combustion engine (ICE) motor and electric motors, but have different working operation models. HEV components can be integrated using one of the four different topologies: series, parallel, series-parallel and complex. PHEVs represent the notable prosperity in the automotive sector and an advancement to the HEV technology due to the All-Electric Range feature allowing an important mode of operation of the HEV. PHEVs have an electric motor on top of the HEV configuration and

an electrical powertrain that serves as a primary energy source substituting the mechanical powertrain integrated into HEVs, thus yielding lower fuel consumption and emission [9], [11].

PEVs represent an alternative to combustion-engine vehicles that allows to lower carbon emissions and oil consumption. Despite having a similar drivetrain topology to HEVs, PEVs possess larger battery capacity that is electrically rechargeable from the power system [12]. BEVs solely utilize electric motors without configurations and electrical grids as a power source. BEVs present a green technology with its zero-carbon emission since they solely rely on batteries to supply energy to the vehicle. Numerous challenges arise from the use of BEVs, mainly due to their high initial cost, limited driving range, and charging stations [13]. Fuel cell vehicles are similar to BEVs, but their power source consists of fuel cells [11].

Due to the recent technological advancements in the areas of electric machines, power electronics, and energy storage, electrified vehicles constitute a considerable portion of today's automotive market, and their penetration into the market will potentially increase with continuous research and development, governmental regulations and incentives as well as customer preference. The technology of EVs has appeared in the early 20th century but was quickly dominated by ICE technology, famous for its energy-storage capacity allowing the driver to travel long distances at an affordable fuel price. The end of the 20th century, however, brought technological advancements allowing EV development. Different types of motors are integrated into EVs and HEVs. Induction motor design, one of the oldest motor technologies, is employed in a very small number of EV models including electric cars manufactured by Tesla and the Chevy Spark made by General Motors [14]. Most auto-manufacturers utilize an interior permanent-magnet machine in their EVs and HEVs [15], [16].

2.2 Hybrid, Plug-in and Battery Electric Vehicle Powertrain Configurations

Hybrid powertrains have three different architectures depending on the hybrid system configuration and the interaction of the components and modules. The three configurations —parallel, serial, or combined (power-split)— have specific traits with respect to weight, cost, efficiency, and convenience to the user. Each powertrain architecture presents certain

advantages and disadvantages. A serial hybrid powertrain configuration, used in extended-range EVs like Chevrolet Volt, includes a generator coupled to the conventional ICE. The generator onboard powers the electric machine connected in series to induct the power into a battery system or electric motor. This design allows the ICE to be smaller in size and limit its operation need to charge the battery system. A parallel hybrid powertrain operates the combustion engine and the electric motor to propel the car, achieving higher efficiency and torque [9]. The sizing of parallel HEVs is simpler than that of series HEVs, as this first configuration type does not require the generator as a propulsion system [11]. The most promising of all EV types, PEV, has two basic designs: parallel or series. In both architectures, regenerative braking is utilized to enhance system efficiency through feeding back any supplemental energy produced upon braking and adding it to the battery charge [17].

The combination of serial and parallel hybrid designs is known as the power-split topology adopted in EVs such as the Toyota Prius. This design utilizes two electric machines to support the ICE and allows continuously varying transmission ratios as well as optimal engine operating conditions. Since the series-parallel topology requires numerous propulsion systems, its sizing becomes very complex [11], [18]. From 2003 to 2012, the parallel HEV powertrain architecture was globally dominating in the automotive market. The power-split type, commonly used by Asian vehicles such as Toyota, is the second most dominating architecture integrated throughout those years [9].

A variety of different powertrain designs consisting of various quantities and layouts of the systems and elements are used for BEVs. The central motor usually consists of the electric machine installed in the vehicle. The power is then conducted using an axle transmission and a differential. Two electric motors can optionally be installed on the vehicle's axle next to the wheels to propel the car. In this powertrain architecture, two transmissions can be integrated onboard eliminating the need for a differential. The axle motor is more commonly integrated than the central motor. Alternatively, electric machines can be installed into the wheel hub allowing the elimination of transmissions and differentials, resulting, however in lower driving dynamics and comfort levels. This topology is mainly utilized in huge luxury vehicles and high-performance prototype cars such as the Infiniti

8

Emerg-E consisting of two motors inside the wheel-hub with a total of 300 kW power and 1000 Nm torque output [9]. Figure 2.1 shows the common configurations of EVs [17].
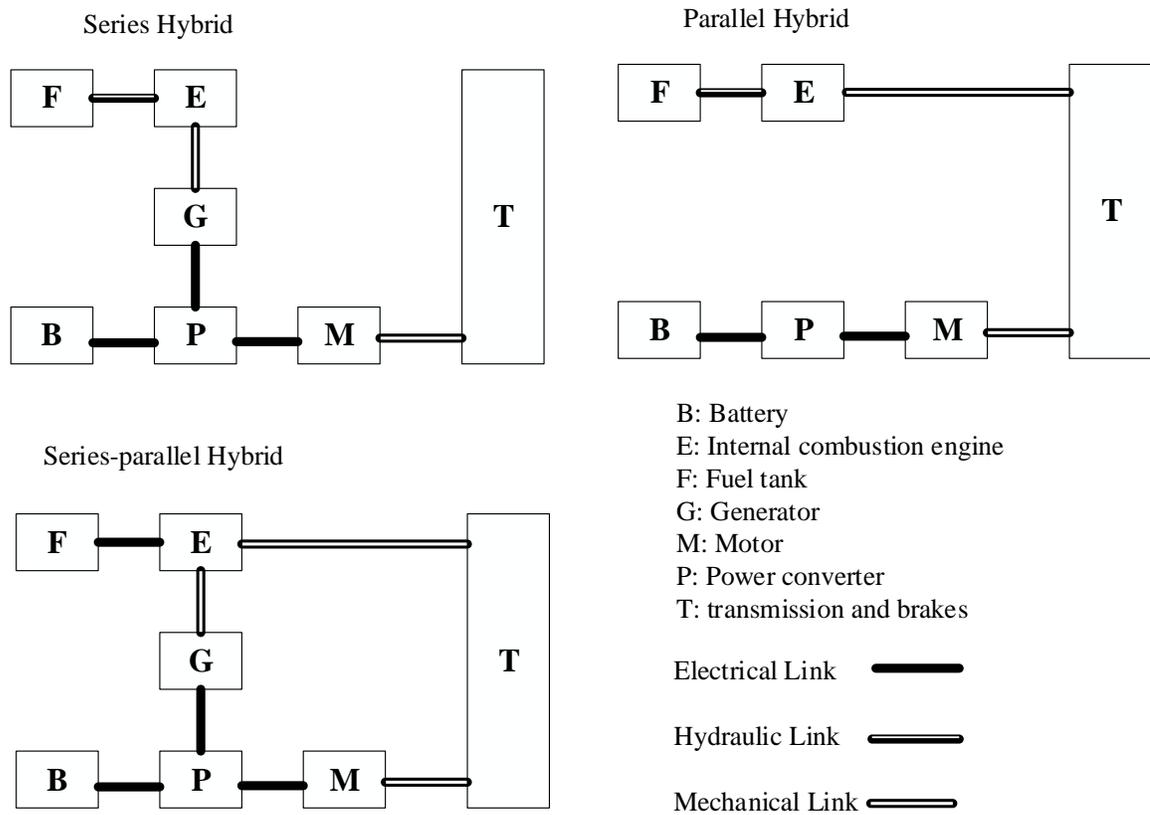
Fig. 2.1 Common architectures of EVs [18].

2.3 EV Battery Charging Review

Battery packs are the core components of EVs. Many factors such as battery cost, lifetime, driving range, charging time and location affect the user's choice to adopt plug-in and hybrid EV technologies rather than combustion-engine vehicles. Energy storage system represents the most vital and expensive part of HEVs and all-electric vehicles [14]. Complexities in battery charging system design and limited availability of charging stations impose limitations on interest in EVs [19]. Also, the increased use of battery chargers may cause harmful impacts on electric utilities. Different types of batteries are utilized in vehicles to meet client requirements, including longer drive range with an affordable total cost.

Batteries from the nickel-metal-hydride (NiMH) or the lithium-ion (Li-ion) family are the two main types of batteries that have been integrated into EVs. While each family has

different chemical and electrical characteristics, Li-ion and NiMH properties are influenced by the type of vehicle in which they are integrated. Li-ion batteries have a higher energy density, specific energy, and specific power than NiMH batteries. Li-ion batteries are adopted in various EVs, including Chevy Volt 2013 and Nissan Leaf 2011, while NiMH batteries are used in Toyota Prius 2010 HEVs [14].

EV battery chargers are divided into two categories — on-board and off-board — and can be characterized by unidirectional or bidirectional power flow. Due to weight, size, and financial limitations, on-board chargers limit high power [20], [21]. Onboard EV battery chargers that are heavy and big occupy space, limiting the number of passengers in the vehicle. Minimizing the weight and size of power-electronic converters integrated into vehicles is an important factor in the power electronics technology to improve the development of EVs [14]. On-board chargers can be conductive or inductive. Charging systems with unidirectional power flow does not require complex hardware and interconnection requirements [22], [23]. On the other hand, bidirectional chargers offer energy injection back to the grid [24].

EV charging systems can provide one of the three power levels: Level I, slow charging; Level II, semi-fast charging and Level III, DC fast charging. Residential consumers can charge their EVs overnight in their garage by simply plugging a Level I charger to a standard 120-V/15-A single-phase grounded outlet. Level I charging eliminates the need for infrastructures, as the system can be installed in the vehicle. Private and public institutions normally use Level II charging that requires a 208 V or 240 V outlet. Since semi-fast charging systems offer an adequate amount of power and can be easily integrated with most facilities, it has been drawing researchers and developers interest in the literature [25]. Tesla vehicles are equipped with on-board Level II charging systems that solely require an outlet. Level II charging is the most often used in Canada and is recommended by automobile manufacturers [19].

Although Level III chargers provide a significantly reduced charging time of less than an hour, this power level requires expensive charging infrastructures [26]. Chargers with high power levels reduce charging time but may increase on-peak demands, thus overloading local DTs leading to a rise in transformer losses, temperature, and lifetime reduction [27].

Level III charging may use multilevel converters that can reduce switching frequency and stress on devices as well as smaller filter size and cost. However, this requires extra complex elements leading to expensive control circuitry [28]. Table 2.1 categorizes charging based on its power level [8].

TABLE 2.1. Charging Power Level Characteristics.

Charging Characteristics	Power Level Type		
	Level I	*Level II*	*Level III*
Charging Time	8 –12 hours	3 – 8 hours	0.2 – 1 hour
Charger Location	On-board	On-board	Off-board
Rated Voltage	110/120 Vac	208 - 240 Vac	440 Vdc
Rated Current	15 – 20 A	15 – 30 A	125 A
Installation Requirement	Not Required - Std 120 V Electrical Outlet	Special Installation Required	Special Installation Required

Uncontrolled charging may overload the existing power system, especially during on-peak summer periods, leaving certain power grid in some regions incapable of accommodating the additional charging load. According to studies in [29], EV consumers tend to charge their PEVs between the hours of 6 p.m. – 8 p.m., which may result in a daily charging peak. Uncontrolled charging causes impacts on power systems regardless of occupying a low demand on the overall power generation capacity. The effects on power distribution systems vary with the charging technologies and penetration levels used and include poor power quality, voltage, transformer losses, temperature rise, and lifetime degradation [30]. A high penetration level of PEVs requires large energy consumption due to the need for adding additional load on distribution systems [31]. With the predicted increased EV load demand in the future, PEVs are anticipated to consume additional energy and uncoordinated charging may result in serious impacts on the grid including higher power losses, lower power quality, phase imbalance and transformer lifetime reduction [30].

2.4 EV Battery Charging Impact Assessment and Mitigation Techniques Review

Numerous studies have been conducted to evaluate the effects of EV battery charging on the distribution system and its components. These studies consider different criteria to quantify these effects. This section provides an overview of studies performed about the

effects of EV charging on DTs, DS, as well as DHPF algorithm, and EV charging harmonic compensation techniques.

2.4.1 EV battery charging effects on distribution transformers

In the literature, many studies were conducted to assess the negative impacts of EV battery charging on power systems. The effects of increased EV load demand, including current harmonics, on load loss, temperature and aging acceleration factor of a 100 kVA DT is presented in [4], and the capability of the power system to safely accommodate the extra EV load is studied. The harmonic impacts on the grid of Level II and Level III chargers are studied in [32], and voltage THD for each level is obtained. The aging acceleration factor and loss of life (LOL) of DT is calculated in [33] for different battery charging load profiles. The effect of EV charging on the thermal aging of a DT is modeled in [34] taking into consideration uncertainties of charging loads such as charging modes, initial SOC, and charging starting time. The impact of charging second-generation PEVs on the insulation aging of DTs is studied in [35], using Monte Carlo to estimate the LOL of a 50 kVA DT for various vehicle makes, and Level I as well as Level II charging levels. The impacts are investigated, including Time-of-Use (TOU) under two charging cases; one is charging time starting at 7 p.m., and the other is charging time starting at midnight. The DT LOL is determined at different charging times and penetration levels of PHEVs in [36]. Fast EV charging effects on the insulation lifetime of a 115/22 kV power transformer in the Provincial Electricity Authority of Thailand substation are studied in [37]. The effect of harmonic distortion on DTs is presented in [38] considering the transformer life degradation as a function of battery charger characteristics and charging algorithm. Conclusions are made to present a quadratic relationship between the transformer lifetime reduction and THD of the battery charger current. The distribution-level secondary transformer LOL is obtained in [39] due to EV charging effects, taking into account different charging scenarios such as residential loading, and geographical locations.

This research presents the impacts of current harmonics produced by EV battery charging on DTs in addition to conventional loads connected to the network. The harmonic spectrums of three charging levels are used to obtain the load loss, temperature rise, and lifetime of a sample DT at different loading conditions. Current harmonic data are collected

throughout the charging cycle to include the effect of SOC on the current harmonic distortion. Weighted arithmetic mean is computed on the time-variant harmonic magnitudes to determine the harmonic magnitude at each harmonic order [40].

2.4.2 EV battery charging effects on distribution systems

Harmonic pollution due to nonlinear devices such as PEVs can cause serious effects on the distribution systems, including voltage deviations, voltage imbalances, increased power losses, lines, and equipment overloading, supply-demand imbalances and instability problems [41]. A stochastic model for EV charging load demand impact analysis on distribution systems is presented in [42]. In this study, the average losses and voltage drops of an IEEE 13-bus test system and a 25-bus test system are obtained. Besides, network congestion and undervoltage and overcurrent events of the 13-bus system are also calculated. A steady-state analysis of impacts of various levels of PEVs on distribution grids of a Greek distribution network is evaluated in [43]. Results such as voltage level of buses and branch loadings are obtained after performing load flow analysis. Feeder active losses are determined under different charging strategies and EV penetration levels. Voltage magnitude profile and voltage unbalance factor for different EV charging cases are determined in [44], and conclusions are drawn about their compliance with EN50160. Furthermore, voltage droop charging and onboard peak shaving strategies are discussed in this study, and their potential of reducing the negative effects on the residential grid is noted. The effects of increasing EV penetration on the grid are studied in [45] using a stochastic model based on Monte Carlo simulations. The model is then used to assess the effects of uncoordinated and coordinated EV charging. EV impact assessment in [46] considers several factors that impact primary and secondary distribution voltage quality, including EV load location, size and penetration level. A comparative analysis is conducted on each of typical North American and European distribution circuits. The impacts of EV charging station on the grid are modeled in [47] using MATLAB/Simulink. The harmonic disturbance is quantified due to connecting a different number of EV chargers in the network. Voltage profile with zero EV penetration is compared to the one with EV charging integration. The decrease in the transformer's kVA rating at different EV loads is also shown. A comprehensive model for PHEV incorporating its different characteristics is presented in [48] to evaluate the EV effects on distribution systems. This model is used on

a 34 node IEEE distribution network to assess PHEV effects on peak load demand, voltage deviation, and total power losses in different scenarios. Voltage deviations including under/over voltage and voltage imbalance are estimated in [49] using Monte Carlo simulations to study the effects of EVs on power quality of the grid. DT overload and unbalance are evaluated considering different characteristics including various EV types, penetration and charging levels.

The effects of EV battery charging on the power quality of the EV-interfacing transformers and substation distribution transformer are analyzed in this work. A case study is performed on a 33-bus DS at which different types of linear loads are connected combined with four EV parking lots. Each parking lot is modeled as a current source injecting harmonic components into the grid. The voltage profile at each bus is obtained for each harmonic order, followed by a calculation of voltage THD and current THD at the main substation.

2.4.3 Decoupled harmonic power flow algorithm technique for non-linear loads

The extensive use of nonlinear devices such as power electronic components produces harmonic currents due to their nonlinear voltage-current ratios. These harmonic currents can spread through the network and result in harmful harmonic voltages, leading to poor power quality. Harmonic calculations should be considered to estimate non-linear devices' negative impacts and predict the risks they may impose on the power system. However, computational time suffers, and the complexity level increases due to the presence of nonlinear loads in the calculations. Several techniques, including modeling techniques, system condition, and solution approaches, have been detailed in the literature to solve the harmonic power flow problem. Solution approaches fall under two categories: coupled and decoupled methods. A coupled solution approach is suitable to provide an accurate solution to nonlinear systems with strong couplings between harmonics. Although Newton-based harmonic power flow provides an accurate solution since it includes harmonic couplings at all frequencies, convergence problems in large power systems with several nonlinear loads may arise [50]. For simplicity, harmonic couplings are ignored to lower computing time and memory storage requirements [51]. Harmonic distortion produced by inverter-

based DGs is evaluated in [52], and validation is performed on an IEEE 30-bus distribution network.

The accuracy of DHPF is discussed in [51] by simulating an IEEE 18-bus system, computing the results under distortion and comparing them with the results produced by other standard techniques such as HARMFLOW and ETAP. The investigation is also applied on an IEEE 23-bus system with the presence of multiple nonlinear loads, demonstrating the suitability of using this technique on large distorted systems. It is also concluded that decoupled methods provide a compromise between the complexity level of calculations and reliability of results. The DHPF is employed in [41] to estimate harmonic distortion of PEVs and wind turbines. THD of voltage at each bus is measured to estimate harmonic distortion of voltages, and a sensitivity factor is defined to determine the bus with the largest effect of average individual harmonic voltage distortion. The approach is then verified on an IEEE 13-bus system and a 394-bus three-phase unbalanced DS with chargers and wind turbine loads. The analysis shows that harmonics result from PEV chargers and wind turbines and that voltage THD values at buses located close to nonlinear loads violate the 5% limitation outlined in the IEEE Standard 519-1992.

2.4.4 Harmonic compensation techniques of EV charging

Several techniques have been proposed in the literature to reduce the negative effects of current harmonics due to EV battery charging on the distribution network. Controlled EV charging schedules could allow a higher EV penetration into the network. Utilities apply a TOU rate on electricity consumption that results in a different price for peak and off-peak hours. Consequently, the time-variant pricing of electricity affects consumers' choices and motivates them to charge their EVs during the off-peak hours [46]. Adopting an off-peak charging schedule could lead to a smoother load demand profile. A mitigating technique, consisting of infrastructural upgrades, is proposed in [46] to address the impacts of EV charging on the secondary service voltages and service transformer load demands. This method involves increasing the kVA rating of the service transformer and employing an additional service transformer to reconfigure the secondary circuit. The impacts of EV penetration into the DS are simulated under both uncoordinated and coordinated charging as well as two EV penetration levels in [53]. A centralized method is proposed in [54] to

15

co-optimize transformer LOL with EV charging and discharging management to minimize the total cost of operations. The model considers the transformer's thermal temperatures, accelerated aging factor, and LOL. This model is compared with the decentralized strategy. The centralized management proposed in this study is dependent on a distribution system operator or an independent aggregator. The DS operator must also evaluate the potential costs arising from the need of investing in communications and control infrastructure to implement this strategy.

PV integration into the network to which EVs are connected represents a mitigation approach to reduce the significant effects on power systems caused by the harmonic current injection of EV battery charging. An advanced control method of PV inverter used as active filter is presented in [55] to lower current harmonics produced by EV fast charging. In this study, a fast-charging station consisting of five EV fast chargers and a PV power plant equipped with a PV inverter is connected to the grid. THD for current and voltage are reduced with the proposed control approach, achieving a voltage THD lower than the limit. PVs can also be connected at buses with the presence of EVs to achieve harmonic compensation produced by both non-linear devices. Solar PV microgeneration is proposed in [56] to reduce overloading and LOL of the DT through charging EVs. The effect of EV penetration on dielectric oil degradation of a DT in an industrial unit is also calculated. Studies [54] – [55] do not address the current disturbance through the substation transformer caused by EV loads, but are rather limited to compensating the harmonics causing the deterioration of the EV-interfacing transformers. The impacts of DG penetration with EVs on the grid are studied in [57] through probabilistic studies performed on the IEEE 34-distribution system.

CHAPTER 3

EV BATTERY CHARGING IMPACTS ON DISTRIBUTION TRANSFORMERS

3.1 Harmonic Components due to Non-Linear Devices

The extensive use of power electronic components, including rectifiers, thyristors, and diodes with capacitor smoothing, and renewable energy sources have nonlinear characteristics that produce nonsinusoidal current and voltage waveforms in power systems. Harmonics are one main type of waveform distortion. The harmonics generated by nonlinear equipment lead to increased losses and decreased lifetime in utility equipment such as transformers. A Fourier series is employed to formulate the periodic nonsinusoidal waveforms, and each term of the Fourier series represents the harmonic component of the distorted waveform. Nonsinusoidal voltage and current waveforms are respectively presented in (3.1) and (3.2):

$$v(t) = V_{DC} + \sum_{h=1}^{h_{max}} V_{rms}^h \cos\left(hw_0 t + \phi_h\right) \tag{3.1}$$

$$i(t) = I_{DC} + \sum_{h=1}^{h_{max}} I_{rms}^h \cos\left(hw_0 t + \phi_h\right) \tag{3.2}$$

where h is the harmonic order, ω_0 is the fundamental frequency, V_{rms}^h and I_{rms}^h are respectively the rms amplitude values of voltage and current for the hth harmonic order, and ϕ_h is the phase shift of voltage in (3.1) and the phase shift of current in (3.2) for the hth harmonic order.

Harmonic components of Fourier series of a nonsinusoidal function can be even or odd. Odd harmonics result from the Fourier series of a half-wave symmetry. Harmonics of order 1 corresponds to the fundamental frequency of the waveform, while harmonics of order 0 are linked to the DC component of the waveform. Triplen harmonics are the odd multiples of the third harmonic. The effects of voltage and current harmonics produced by a nonlinear load can spread in the entire power system due to the power system impedance. The harmonic components of a distorted waveform can be quantified using the THD harmonic index, which measures the effective value of the harmonic contents of a distorted waveform. THD for voltage and current can be expressed in percentage as in (3.3) and (3.4), respectively. This commonly used index can be easily calculated, serving as a quick tool to measure the amount of distortion in power systems.

17

$$THD_v = \frac{\sqrt{\sum_{h=2}^{h_{max}}(V_h)^2}}{V_1} \qquad (3.3)$$

$$THD_i = \frac{\sqrt{\sum_{h=2}^{h_{max}}(I_h)^2}}{I_1} \qquad (3.4)$$

Power quality issues are originated from four sources: unpredictable events, electric utility, customers, and the manufacturer. Customer loads constitute a significant portion of power quality issues in the current power systems due to harmonics produced by nonlinear loads, including power electronic equipment and renewable energy technologies. An accurate assessment of harmonic effects caused by EV battery charging on power system components is useful for the utility to design, maintain, and operate the power system under minimal power quality issues. Developing manufacturing standards for the use of electronic devices should incorporate the effects of nonlinear devices on power quality. Standards such as IEEE Std C57.110 and C57.91 have been developed to assess distribution transformers' ability to supply nonsinusoidal load currents. Electric utilities and manufacturers should work in harmony with the end-users to address power quality problems [50].

3.2 Impacts Modeling and Quantification of EV Charging on Distribution Transformers

Current harmonics produced by EV battery charging loads can result in an increased transformer load loss, rise in temperature, and decreased lifetime. This section discusses modeling and quantifying these three transformer parameters. The p.u. modeling and quantification of impacts of EV charging on DTs are summarized in a chart presented in Fig. 3.1.

3.2.1 Transformer loss modeling and quantification

Transformers losses are categorized into no-load loss (P_{NL}) and load loss (P_{LL}). The transformer total loss (P_{total}) corresponds to the sum of excitation loss and impedance loss, which can be represented as given in watts in equation (3.5). Load loss consists of I^2R

copper loss (PI^2_R), and stray loss caused by stray electromagnetic flux in the windings, core, magnetic shields and tank walls. Stray loss (P_{STRL}) is divided into winding stray loss and non-windings stray loss. Winding eddy-current loss (P_{EC}) is a characteristic that can lead

Per-unit Modeling of DT Losses
Incorporating Current Harmonics

$$P_{LL-pu} = I^2_{pu}\left(1 + F_{HL}P_{EC-R-pu} + F_{HL-STR}P_{OSL-R-pu}\right)$$

Temperature Rise Modeling of DT

$$\theta_{total} = \theta_{TO} + \theta_g$$

Modeling of DT Loss of Life

P.U. insulation life

$$Life_{pu} = 9.8\times10^{-18}\exp\left(\frac{15000}{\theta_H + 273}\right)$$

Aging acceleration factor

$$F_{AA} = \exp\left(\frac{15000}{383} - \frac{15000}{\theta_H + 273}\right)$$

Percent loss of life

$$Loss_{Life-\%} = \frac{F_{AA}\times t\times100}{insulation\_life_{normal}}$$

Transformer real life

$$Life_{real} = \frac{insulation\_life_{normal}}{F_{AA}}$$

Fig. 3.1. DT modeling and quantification due to EV battery charging.

to excessive winding loss and thus winding overheating and hot spot temperature in transformers. In dry-type transformers, winding eddy-current loss (P_{EC}) solely contributes to the stray loss since heating due to other stray losses is released in the cooling air, while other stray loss (P_{OSL}) in non-winding components such as the core, clamps, and structural parts is produced in liquid-filled transformers in addition to eddy-current loss. The transformer load loss in watts is given by (3.6) and (3.7).

$$P_{total} = P_{NL} + P_{LL} \tag{3.5}$$

$$P_{LL} = P_{STRL} + P_{I^2R} \tag{3.6}$$

$$P_{LL} = P_{I^2R} + P_{EC} + P_{OSL} \tag{3.7}$$

The excessive temperature rise of the windings draws significant concerns about transformers operating under nonsinusoidal load conditions. The transformer losses are expressed on a p.u. basis, where base loss is the copper loss at rated current, which is also the base current. Transformer p.u. load loss can be calculated considering loss density in the windings on a p.u. basis, due to the overheating of windings of a transformer working under harmonic load conditions. The I^2R loss at rated load is one p.u. The transformer load loss at rated load conditions in p.u. is given by

$$P_{LL-R-pu} = 1 + P_{EC-R-pu} + P_{OSL-R-pu} \tag{3.8}$$

where $P_{LL-R-pu}$ is the load loss, $P_{EC-R-pu}$ is the eddy-current loss, and the $P_{OSL-R-pu}$ is the other stray loss. These losses are expressed in p.u. under rated conditions.

Harmonic loss factor is a characteristic that is useful to determine the ability of a transformer to supply power to a load. The harmonic loss factor for winding eddy currents, F_{HL}, is applied to the winding eddy loss to determine the heating due to the harmonic load current. It is the ratio of the winding eddy current losses under harmonic conditions to the winding eddy current losses at the power frequency. Winding eddy-current loss under a certain frequency is proportional to the square of the load current and approximately proportional to the square of the frequency. In liquid-filled transformers, other stray losses can induce extra heating of the cooling liquid and the hottest spots in the structural parts. Similarly to the harmonic loss factor for winding eddy-current losses, other stray losses are proportional to the square of the load current but increase by a harmonic exponent factor of 0.8. The harmonic loss factors for winding eddy currents and other stray losses, F_{HL-STR}, are presented in (3.9) and (3.10), respectively.

$$F_{HL} = \frac{\sum_{h=1}^{h=h_{max}} I_h^2 h^2}{\sum_{h=1}^{h=h_{max}} I_h^2} \tag{3.9}$$

$$F_{HL-STR} = \frac{\sum_{h=1}^{h=h_{max}} I_h^2 h^{0.8}}{\sum_{h=1}^{h=h_{max}} I_h^2} \tag{3.10}$$

where, h_{max} is the highest harmonic order, and I_h is the ratio of the hth harmonic current to the fundamental current.

The rms load current in per-unit, I_{pu}, is expressed as

$$I_{pu} = \sqrt{\sum_{h=1}^{h=h_{max}} \left(I_{h-pu}\right)^2} \tag{3.11}$$

where I_{h-pu} is the per-unit rms current at harmonic order h.

Harmonic currents produced by non-linear devices can increase eddy-current losses in the windings and other-stray losses. The p.u. copper loss ($P_{I^2R\text{-pu}}$), eddy-current loss ($P_{EC\text{-pu}}$), and other stray loss ($P_{OSL\text{-pu}}$), including the current harmonics and the harmonic loss factors are expressed in equations listed in (3.12) – (3.14), respectively.

$$P_{I^2R-pu} = I_{pu}^2 P_{I^2R-R-pu} \tag{3.12}$$

where $P_{I^2R\text{-}R\text{-}pu}$ is the copper loss at rated conditions in per-unit.

$$P_{EC-pu} = I_{pu}^2 F_{HL} P_{EC-R-pu} \tag{3.13}$$

$$P_{OSL-pu} = I_{pu}^2 F_{HL-STR} P_{OSL-R-pu} \tag{3.14}$$

Using (3.12)–(3.14), the transformer load losses under non-linear load current can be obtained, as follows [58]:

$$P_{LL-pu} = I_{pu}^2 \left(1 + P_{EC-R-pu} F_{HL} + P_{OSL-R-pu} F_{HL-STR}\right). \tag{3.15}$$

3.2.2 Transformer temperature rise modeling and quantification

The transformer losses caused by current harmonics induce heat in the system resulting in thermal tensions. 50% of transformer lifetime reduction is due to heat stresses produced by non-linear loads [59]. The top-oil-rise over ambient temperature of a transformer, Θ_{TO}, is proportional to the total losses to the 0.8 exponent, and is expressed in degree Celsius, as follows:

$$\theta_{TO} = \theta_{TO-R} \left(\frac{P_{LL-pu} + P_{NL-pu}}{P_{LL-R-pu} + P_{NL-pu}}\right)^{0.8} \tag{3.16}$$

where $\Theta_{TO\text{-}R}$ is the top-oil-rise over ambient temperature at rated conditions in degree Celsius and $P_{NL\text{-}pu}$ is the no-load loss in per-unit.

The hottest-spot conductor rise over top-oil temperature, Θ_g, is given in degree Celsius by

$$\theta_g = \theta_{g-R} \left(\frac{1 + F_{HL} P_{EC-R-pu}}{1 + P_{EC-R-pu}} I_{pu}^2 \right)^{0.8} \tag{3.17}$$

where Θ_{g-R} is the hottest-spot conductor rise over top-oil temperature during rated conditions in degree Celsius. Using the top-oil-rise over ambient temperature and the hottest-spot conductor rise over top-oil temperature, the hottest-spot conductor rise over ambient, Θ_{total}, is expressed in degree Celsius [58], [60] by

$$\theta_H = \theta_{TO} + \theta_g . \tag{3.18}$$

3.2.3 Transformer lifetime modeling and quantification

Power primary and secondary distribution is a major component of an electric power system that starts at distribution substations and extends to end-users' electric devices. Distribution substations include step-down transformers that lower the range of sub-transmission voltages to primary distribution voltages level suitable for local distribution. Distribution transformers represent the point of connection between the primary system and the secondary system. They can be mounted outdoors on overhead poles or at ground level on pads, indoors in buildings, or underground. IEEE C-57.91, *IEEE Guide for Loading Mineral-Oil-Immersed Transformers*, explains the risks of transformer loads above nameplate ratings and sets regulations to reduce the risks associated with overloading transformers. Distribution reliability is an important characteristic that end-users need to have their desired continuous power supplied to their electric equipment and facilities. Electric utilities set a goal of not exceeding an average interruption of two hours per year [61].

Transformer thermal rise can contribute to lifetime reduction, and thus threatening distribution reliability. A relation of the transformer p.u. insulation life and the winding hottest-spot temperature is established with time as

$$Life_{pu} = 9.8 \times 10^{-18} e^{\left(\frac{15000}{\theta_H + 273} \right)} \tag{3.19}$$

where $Life_{pu}$ is the per-unit transformer insulation life. Transformer insulation life for a given temperature is the total duration between the initial condition at which the insulation is considered new and the final condition at which dielectric or short circuit stresses or mechanical movement occurring in normal service may result in an electrical maloperation.

The p.u. insulation life curve displays the aging rate acceleration level for temperatures exceeding a reference temperature of 110 ℃. This rate of aging is reduced below normal for temperatures below 110 ℃. This curve reflects temperature as the main variable impacting thermal life.

The per-unit transformer insulation life curve is used to calculate the aging acceleration factor F_{AA}. For a given transformer with an insulation system rated for 65 ℃ average winding temperature rise, F_{AA} is equal to one at a reference hottest-spot temperature of 110 ℃. This factor is proportional to the hottest-spot temperature and exceeds the value of one for temperatures above 110 ℃, implying that the transformer insulation aging rate is accelerated beyond normal. The aging acceleration factor is below one for hottest-spot temperatures lower than the reference temperature, indicating that the transformer is safely operating. In [60], the aging acceleration factor is given by:

$$F_{AA} = \exp\left(\frac{15000}{383} - \frac{15000}{\theta_H + 273} \right)$$
(3.20)

The percent loss of life, given in (3.21), is obtained from the insulation per-unit life curve,

$$LifeLoss_\% = \frac{F_{AA} \times t \times 100}{InsulationLife_{normal}}$$
(3.21)

where t is the total time given as 24 h and $InsulationLife_{normal}$ is the normal insulation life in hours of a well-dried oxygen-free 65°C average winding temperature rise system at the reference temperature of 110°C. The normal insulation life of a 65 ℃ average winding temperature rise system is 20.55 years (180 000 hours) at the reference temperature. Normal percent LOL operating at a rated hottest-spot temperature of 110 ℃ for 24 h is 0.0133%.

The distribution transformer real life, $Life_{real}$, can be determined in years, as in (3.22) [62].

$$Life_{real} = \frac{InsulationLife_{normal}}{F_{AA}}$$
(3.22)

3.3 Case Study: Impact Assessment of EV Battery Charging on a Sample 1,500-kVA Distribution Transformer

EV penetration affects transformer losses, temperature rise, and lifetime reduction. Comparing those impacts with the presence of EVs to the ones with zero EV penetration

is important to understand the issues associated with the non-linear nature of EV loads. Next, the transformer impacts of two harmonic spectrums corresponding to different charging levels are compared. The harmonic spectrum distributions include the effect of SOC on THD. The study is performed on a sample 1,500 kVA DT.

3.3.1 Comparative Analysis of Non-Linear Load Effects on DT before and after EV Integration

Harmonic distribution of a Level I/II single-phase charger consisting of an onboard AC-DC controlled rectifier and that of conventional loads are given in Tables 3.1 [7] and 3.2 [58], respectively. The harmonic distribution of the charger is considered only at one point during the charging time, neglecting the impact of SOC on THD for simplicity. This Level I/II charger, with a 4 – 20 kW power at 208 V, can take up to four hours to recharge EV batteries [7]. The harmonic spectrum consisting of EV battery charging is then added to that of conventional household items to construct the total harmonic spectrum that includes current harmonics caused by EV charging. The effects of EVs are studied on a sample 1,500 kVA DT whose characteristics at rated conditions are given in Table 3.3 [62]. An approximated daily load per unit curve of the USA in 2011 is shown in Fig. 3.2 [4].

TABLE 3.1. Harmonic Distribution of Level I/II Single-phase Charger, at t = 61 mins.

Harmonic Order	Harmonic Ratio
3	0.0935
5	0.0172
7	0.012
9	0.0043

TABLE 3.2. Harmonic Distribution of Conventional Household Items, Normalized to Fundamental.

Harmonic Order	Harmonic Ratio
1	1
3	0.35
5	0.17
7	0.12
9	0.092
11	0.071
13	0.051
15	0.043
17	0.04
19	0.039

| 23 | 0.032 |
| 25 | 0.029 |

TABLE 3.3. Characteristics of a Sample 1,500 kVA Distribution Transformer.

Characteristic	Rated Value
Power	1500 kVA
No Load Loss	1600 W
Copper Loss	6250 W
Eddy Current Loss	3216 W
Other Stray Loss	1584 W
Winding Temperature Rise	65 °C
Ambient Temperature	30 °C
Normal Insulation Life	180 000 hours
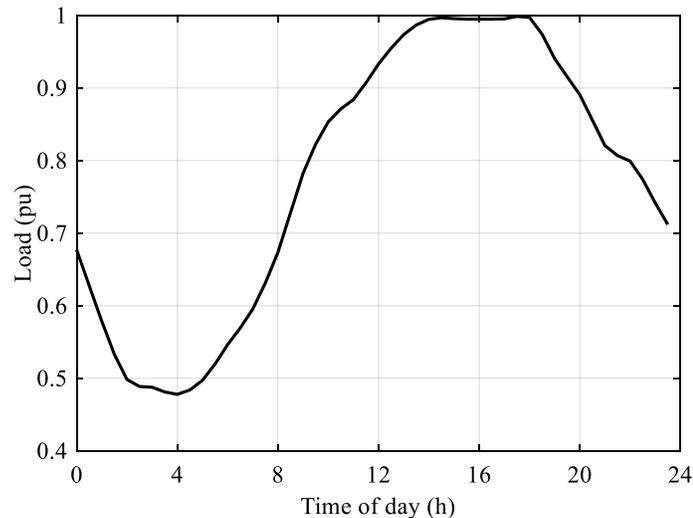
Fig. 3.2. Approximated USA daily load curve in 2011.

Since the assessment is performed under 20% EV penetration level, 20% of the total EV charging load demand estimated in Fig. 3.3 is added to the daily load curve in Fig. 3.2 [4]. EV total load profile is then normalized to obtain the load curve in per unit, as shown in Fig. 3.4. It is assumed that EV users charge their vehicles during the off-peak load hours from 9 p.m. to 4 a.m.

Eddy-current loss and other stray loss are obtained for each of 0% EV penetration (Case 1) and 20% EV penetration (Case 2), as shown in Fig. 3.5. Using these two losses, the load losses of the transformer are also calculated with respect to time. The transformer eddy-current loss and other stray loss are greater in Case 2 than in Case 1, resulting in a rise of load losses. When EV charging is introduced, $P_{EC\text{-}pu}$ increases from 2.60 p.u. to 4.05 p.u.

and $P_{OSL\text{-}pu}$ increases from 0.27 p.u. to 0.42 p.u., causing $P_{LL\text{-}pu}$ to rise from 3.65 p.u. to 5.68 p.u. at 9:30 p.m. At this point, $P_{LL\text{-}pu}$ reaches its apogee (Case 2), while the maximum load loss ($P_{LL\text{-}pu}$=5.58 p.u.) occurs at 5:30 p.m. during the period where there is no EV charging (Case 1).
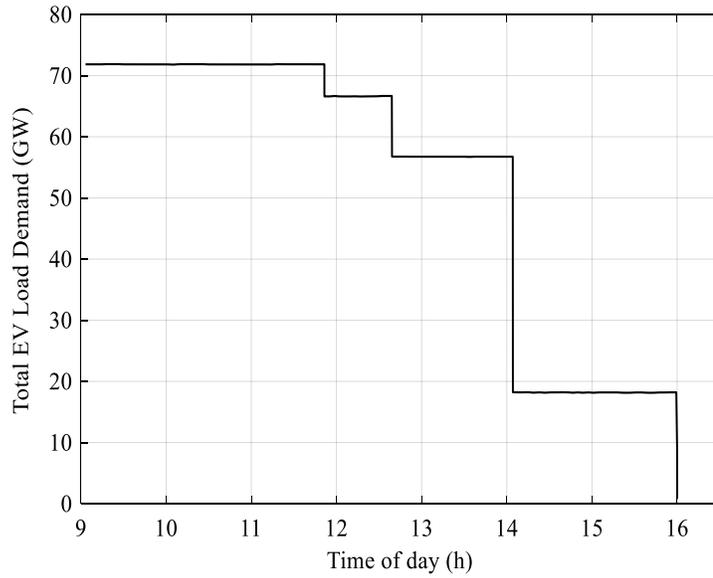
Fig. 3.3. Total load demand of EV battery chargers.
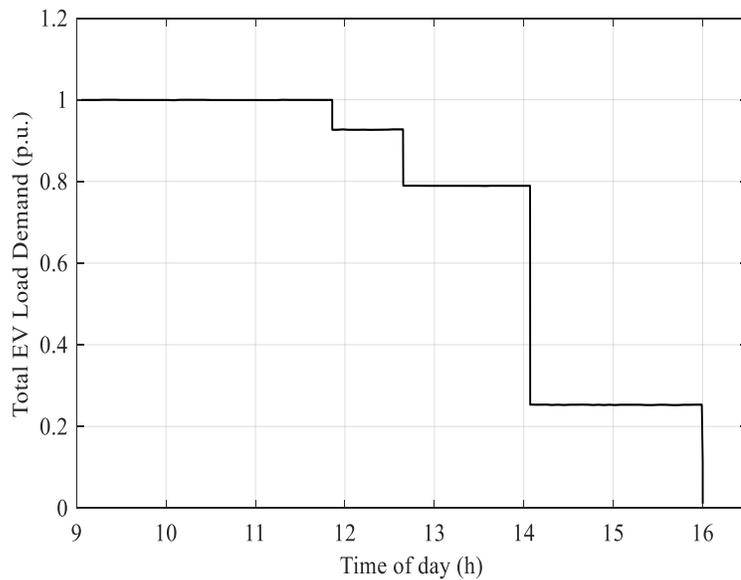
Fig. 3.4. Per-unit total load demand of EV battery chargers.

26
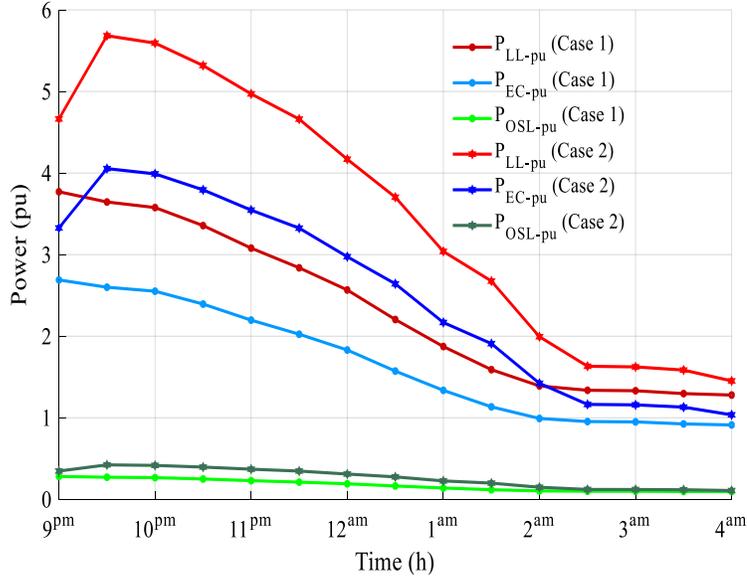
Fig. 3.5. Load loss, Eddy-current loss, and other stray loss.

Thermal analysis is then performed to study the losses impact on the DT. The top-oil rise over ambient temperature, and the hottest-spot conductor rise over top-oil temperature due to transformer losses are shown in Fig. 3.6. At 20% EV penetration, θ_{TO} rises from 79.8 °C to 111.7 °C, while θ_g increases from 8.7 °C to 12.4 °C due to maximum load loss occurring at 9:30 p.m.
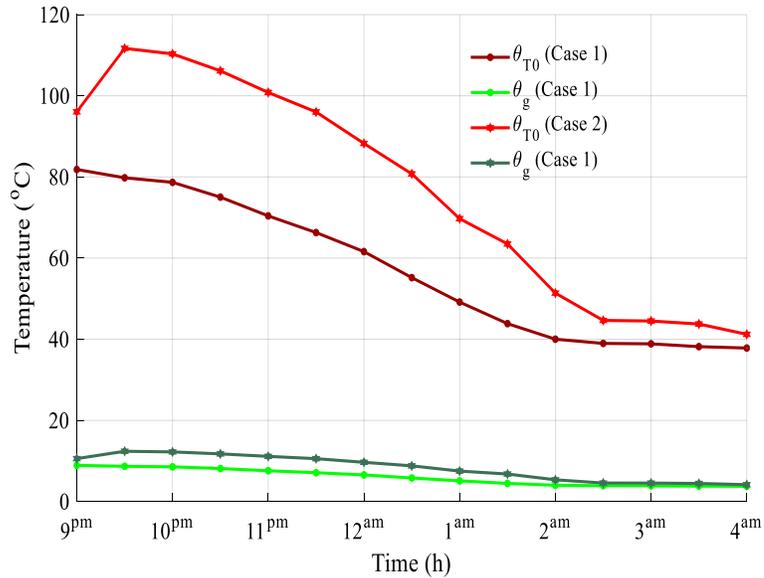
Fig. 3.6. Top-oil rise over ambient temperature and hottest-spot conductor rise over top-oil temperature.

This temperature rise results in an increase of hottest-spot conductor rise over ambient. As shown in Fig. 3.7, θ_{total} increases from 88.5 °C to 124.1 °C at the time corresponding to load loss peak caused by EV charging.

The impact of hottest-spot temperature is then evaluated on the transformer lifetime. First, the aging accelerated factor is determined in both cases, as presented in Fig. 3.8. Since the hottest-spot temperature is below 110 °C in Case 1, F_{AA} is always below one, which indicates that the accelerating rate of transformer insulation aging is normal. However, F_{AA} exceeds one during the period from 9:30 p.m. to 11:00 p.m., implying that the accelerating rate of the transformer insulation aging for the temperatures attained is greater than the one at the reference temperature of 110 °C. F_{AA} rises from 0.097 p.u. to approximately 4.006 p.u. when EV battery charging is introduced.

The transformer p.u. insulation life curve is modeled in Fig. 3.9. The values of this curve with zero EV penetration are very high and above 1.0 p.u. since the DT operates under temperature values that do not exceed the reference temperature. This implies that the insulation life of the transformer operating under these temperature values is not deteriorated. Insulation aging due to EV charging is observed, and the value of transformer insulation life at the maximum EV loading condition declines from 10.30 p.u. (Case 1) to 0.25 p.u. (Case 2) due to a winding hottest-spot temperature rise by 35.6 °C. The degree to which the rate of aging is accelerated is beyond normal in Case 2 due to temperature values exceeding 110 °C during high EV loading points.
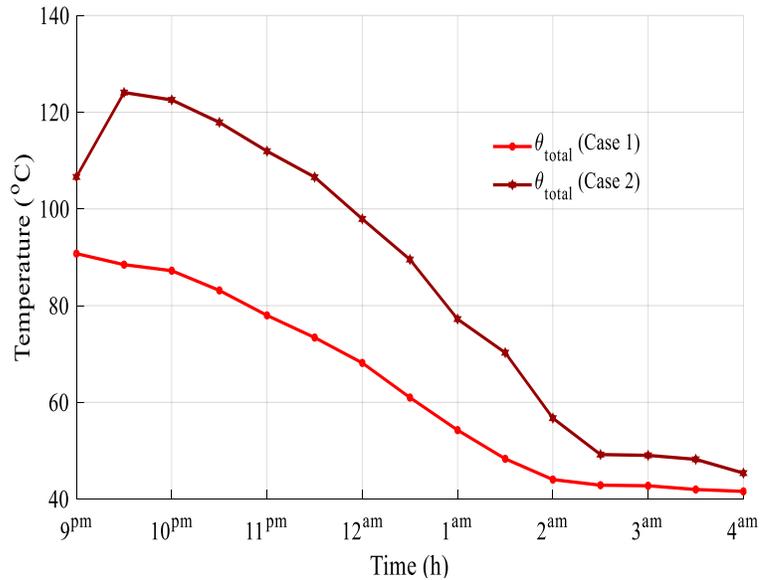
Fig. 3.7. Hottest-spot conductor rise over ambient.

28
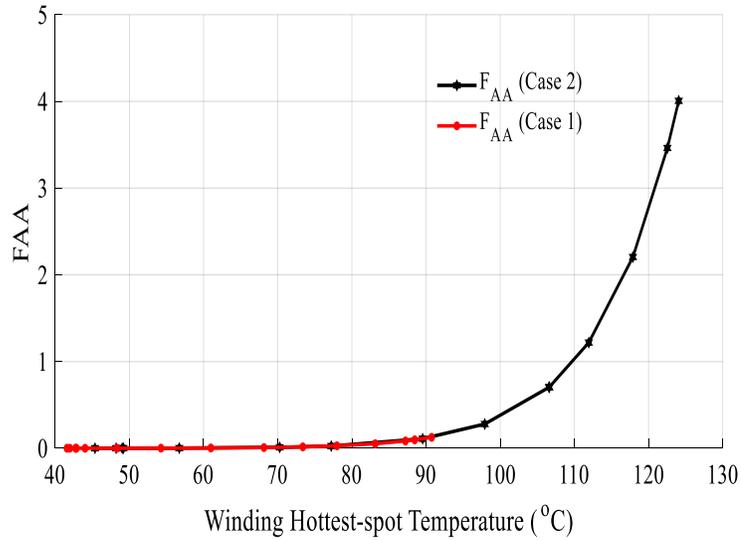
Fig. 3.8. Aging acceleration factor.
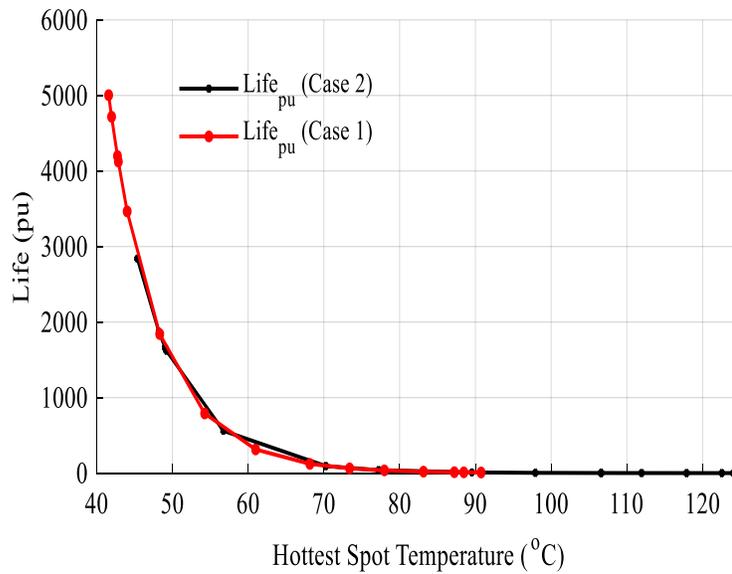
Fig. 3.9. Transformer per unit insulation life.

The percent loss of transformer life is obtained in Fig. 3.10 using the insulation p.u. life curve. The normal percent LOL of a transformer operating at the reference hottest-spot temperature for an entire day is 0.0133% [60]. The percent LOL in Case 1 is less than this normal percent LOL value, as the temperature values remain below 110 °C. $Loss_{Life-\%}$ increases from 0.00129% to 0.05341% at the maximum loading value of 1.01 p.u. It is also above the value of 0.0133% at loading conditions higher than 0.94 p.u., since the aging acceleration factor exceeds one.

29
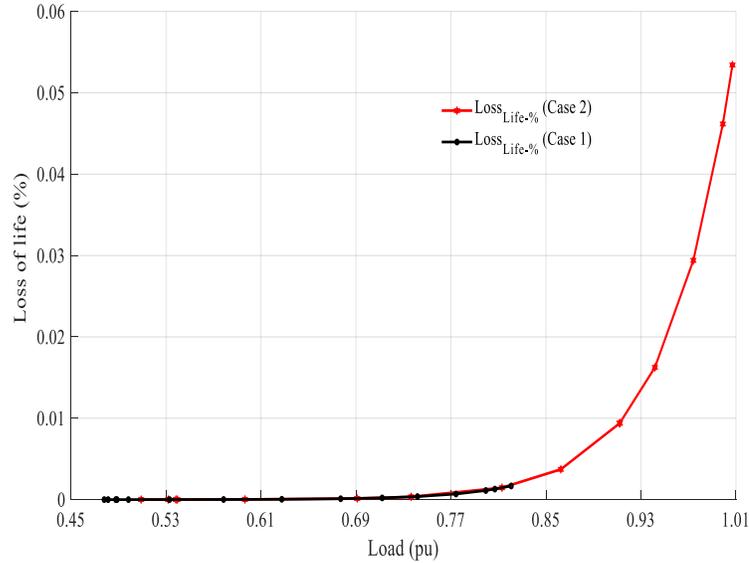
Fig. 3.10. Transformer percent loss of life.

The real-life of the transformer, presented in Fig. 3.11, can be calculated from F_{AA}. It can be noted that the normal transformer life is constant at 20.55 years in Case 1. However, the transformer starts to age when the loading value exceeds 0.94 p.u. At maximum loading of 1.01 p.u., the transformer life decreases from 20.55 years to approximately 5.13 years.

Based on the results, it can be observed that the introduction of EV loads induces a rise in transformer losses, temperature, and aging. The load loss increase due to harmonic currents produced by EV charging causes thermal tensions on the transformer, rising the winding hottest-spot temperature beyond the reference temperature of 110 °C during the period of 9:30 p.m. to 11 p.m. As a result, the aging acceleration factor is greater than one, indicating that the DT is not operating in the safe zone since its rate of aging is accelerated beyond normal. During this period, the per-unit life is below 1, also implying that the rate of aging is reduced above normal. The percent LOL is also less than the normal percent LOL value at the reference temperature. The transformer lifetime decreases from 20.55 years to 5.13 years at 9:30 p.m. The transformer is impacted the most during the period of 9:30 p.m. to 11 p.m. since EV charging load demand is high during this time. The effects are the most severe at 9:30 p.m. since EV charging load reaches its maximum value of 1.01 p.u. Despite charging occurring during the entire period from 9 p.m. till 4 a.m., the transformer operation remains in the safe zone during the period outside of 9:30 p.m. to 11 p.m. This is because EV battery charging demand becomes lower during these times [63].
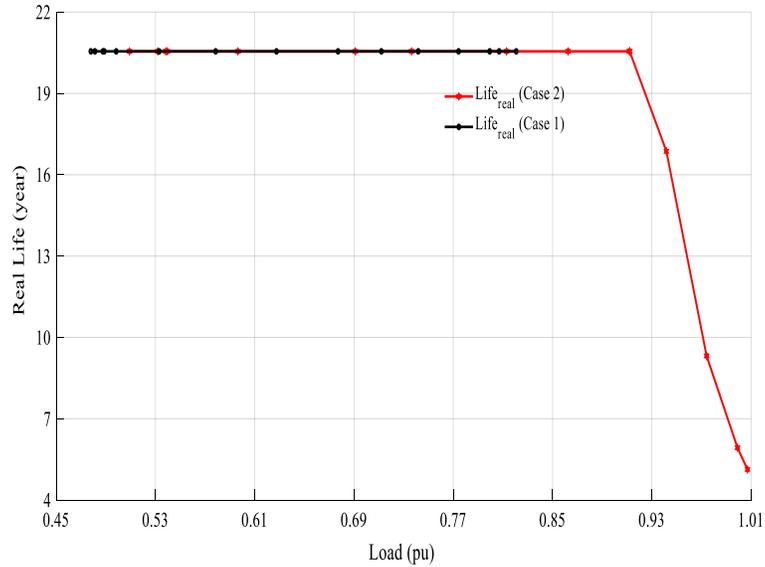
Fig. 3.11. Transformer real life.

3.3.2 Impact assessment of different levels of EV chargers on distribution transformers including SOC

Some existing charger topologies are designed to address the harmful impacts of charging on the power system; however, they are often complicated and lead to high costs. Level II charging has been a key interest to researchers and the desired charging method for users since it significantly reduces the charging time and can also be installed in most places [19]. On the other hand, Level II and Level III high-power charging can cause a rise in power demand and an increase in DT transformer losses, harmonic distortion, and temperature. As a result, the transformer lifetime, reliability, and performance could be threatened [64]. The impact of harmonic components produced by different levels of chargers on DTs, in addition to the harmonic spectrum of conventional household appliances is investigated. Current harmonic measurement data are taken at various time intervals throughout the charging cycle. Two harmonic spectrums are used to analyze the effects of Level I/II and Level III chargers on a sample 1,500 kVA DT. The transformer load loss, temperature rise, and loss of life are modeled and quantified in p.u. at various loading conditions throughout the day with 20% EV penetration.

The harmonic distribution of conventional loads at maximum loading conditions is shown in Table 3.2. Two sets of data are used to quantify the THD of a single-phase Level I/II charger and a three-phase Level III charger during a charge cycle, as presented in Tables

31

3.4 and 3.5. It can be observed from the data that the THD of charging current at the beginning of the cycle is smaller than the one at the end of the cycle. It can be noted, however, that the magnitude of the distorted current decreases during the charging cycle. The third through ninth harmonics of Level I/II and Level III charger levels are presented at various charging times in Tables 3.4 and 3.5, respectively [7].

TABLE 3.4. Harmonic Magnitudes for Level I/II Charger at Different Times of Charging.

$\dfrac{I_h}{I_1}$ (%)	h	Time in Charging Cycle (minutes)					
		3	46	61	79	94	102
	3	0.27	1.76	2.04	2.45	2.33	11.16
	5	1.62	1.56	2.01	1.83	2.12	11.87
	7	2.18	1.35	0.95	1.19	0.9	5.03
	9	0.53	0.77	0.65	0.95	1.56	5.98

TABLE 3.5. Harmonic Magnitudes for Single Phase of Level III Charger at Different Times of Charging.

$\dfrac{I_h}{I_1}$ (%)	h	Time in Charging Cycle (minutes)	
		7	17
	3	2.84	6.61
	5	2.96	6.27
	7	1.81	4.75
	9	2.28	4.65

Weighted arithmetic mean is performed on the time-variant harmonic magnitudes of Tables 3.4 and 3.5 for each harmonic order. The state-of-charge is considered in the THD data to improve the accuracy of the harmonic assessment. The general equation used to obtain the harmonic magnitude is expressed as

$$\frac{I_h^{\Delta t_{total}}}{I} = \frac{\left(\dfrac{I_h}{I}\right)^{t_{n1}} \Delta t_1 + \left(\dfrac{I_h}{I}\right)^{t_{n2}} \Delta t_2 + ... + \left(\dfrac{I_h}{I}\right)^{t_{max}} \Delta t_n}{\Delta t_{total}}(1+K) \qquad (3.23)$$

where ($I_h^{\Delta t_{total}}/I$) is the weighted arithmetic average of harmonic magnitudes at the hth harmonic order measured at different points of charging cycle of duration Δt_{total}, ($I_h^{t_{n1}}/I$) is the harmonic magnitude at the hth harmonic order for the first measured point at a charging cycle time corresponding to t_{n1}. $t_{n1, 2,...,max}$ indicates the time at which the harmonic magnitude is measured, and the total time interval of measurements is $\Delta t_{total} = \Delta t_1 + \Delta t_2 + ... + \Delta t_n$, with n equal to the maximum number of last time interval. K is a factor added to account for the harmonic magnitudes that are present but are not recorded in the

harmonic distribution. This factor K is estimated as 5% for Level I/II and 40% for Level III charging.

The sample 1500-kVA DT, whose characteristics are displayed in Table 3.3, is used to analyze the impacts of harmonic currents. The impacts of harmonic components in the grid on the transformer are then analyzed using the harmonic spectrums of Level I/II (Case 1) and Level III (Case 2) chargers. The harmonic loss factors F_{HL} and $F_{HL\text{-}STR}$ are calculated, and eddy-current loss, as well as other stray loss, are then obtained to determine the load loss in both cases as displayed in Fig. 3.12. It can be observed that the P_{EC} in Case 2 is greater than the one in Case 1 and that the curve representing P_{OSL} in the case of Level III charger is slightly higher than the one of Level I/II charger. The highest value of P_{EC} rises from 4.5024 p.u. (Case 1) to 5.2891 p.u. (Case 2). At the same loading condition, P_{OSL} slightly increases from 0.4524 p.u. (Case 1) to 0.5012 p.u. (Case 2). As a result, the load losses in Case 2 are higher than the ones in Case 1. The load losses peak reaches 6.1958 p.u. and 7.0874 p.u. respectively for Case 1 and Case 2.

Thermal analysis of DT due to loss increase is then computed, and θ_{TO} as well as θ_g are calculated as presented in Fig. 3.13. The peak top-oil rise over ambient temperature attains around 132 °C in Case 2, while it reaches approximately 119 °C in Case 1. Similarly, the hottest-spot conductor rise over top oil temperature is greater in Case 2, but with fewer discrepancies between the two scenarios. At the maximum loading condition, θ_g slightly increases from about 12 °C (Case 1) to approximately 13 °C (Case 2).
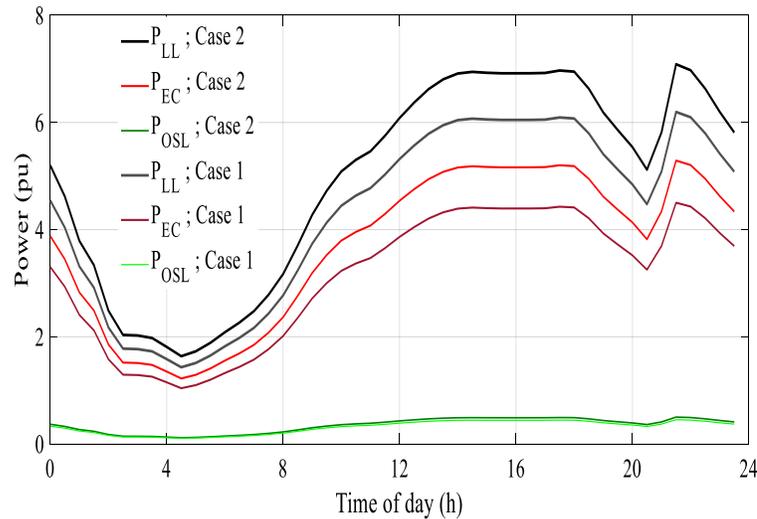
Fig. 3.12. Load losses, Eddy-current loss, and other stray losses in Cases 1 and 2.

33
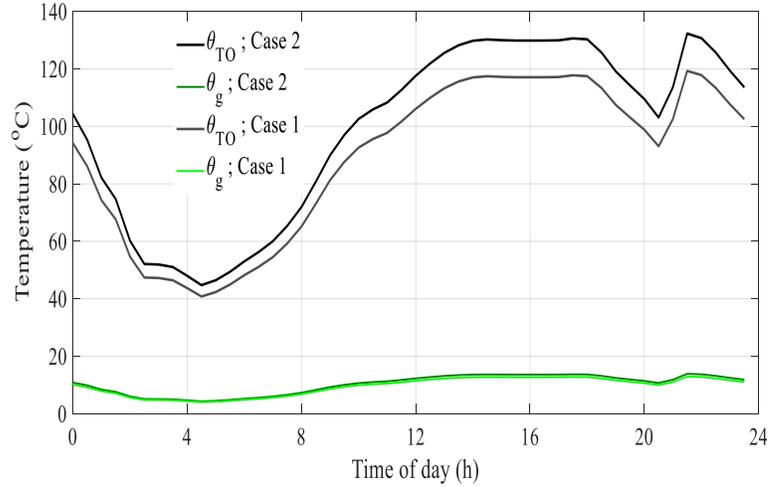
Fig. 3.13. Top-oil rise over ambient temperature and hottest-spot conductor rise over top oil temperature in Cases 1 and 2.

The hottest-spot conductor rise over ambient (θ_{total}) is shown in Fig. 3.14. It can be noted that the losses impact on θ_{total} is more significant in Case 2 than in Case 1. θ_{total} reaches a value of 132 °C in the case of a Level I/II charger, while this value attains 146 °C in the case of a Level III charger. During the charging period from 9 p.m. to 4 a.m., the hottest-spot conductor rise exceeds the reference value of 110 °C only during the period of 9 p.m. to 11:30 p.m. This is due to high EV load demand occurring during this time. However, θ_{total} is also greater than 110 °C and has a value of 115 °C at midnight in the case of a Level III charger.

Then, the thermal stress effect on transformer lifetime is evaluated by calculating aging acceleration factor (F_{AA}), per-unit life, percent loss of life, and DT real life. Based on the results of Fig. 3.15, F_{AA} remains smaller than one for hottest-spot temperature values not exceeding the reference temperature of 110 °C. At higher temperatures, this factor increases, implying that the rate of transformer insulation aging acceleration is higher than the normal rate at the reference temperature. This factor exceeds the value of one between the period of 9 p.m. and 11:30 p.m. in Case 1, reaching a maximum of 8.6 at 9:30 p.m. In the case of a Level III charger, this factor is also higher than one at midnight. It takes a value of 29.5 at 9:30 p.m.
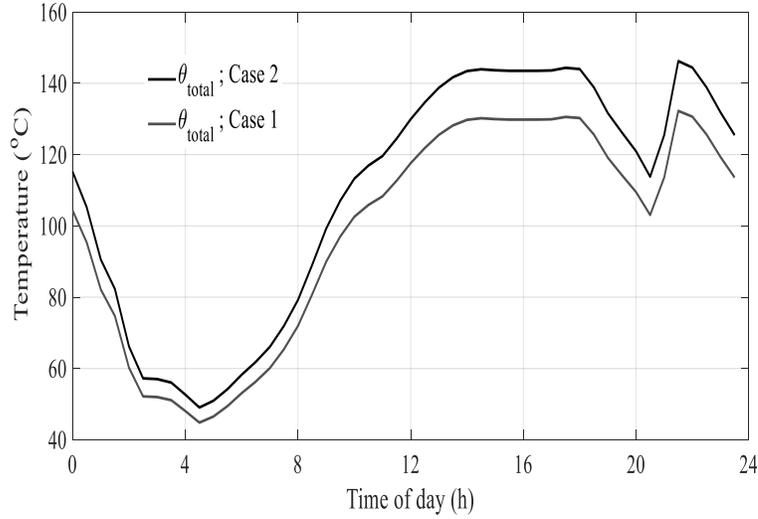
Fig. 3.14. Hottest-spot conductor rise over the ambient temperature in Cases 1 and 2.
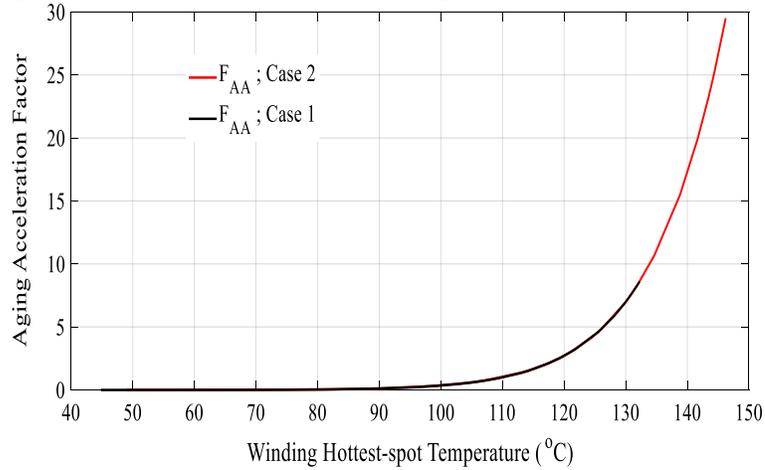
Fig. 3.15. Aging acceleration factor in Cases 1 and 2.

The transformer p.u. insulation life is then obtained as given in Fig. 3.16 for both harmonic spectrums. For hottest-spot temperatures below 110 °C, it can be noted that the per-unit life is high, indicating that the aging rate is reduced below normal. The p.u. life is equal to one at the reference temperature of 110 °C. When the hottest-spot temperature exceeds 110 °C, this per-unit life decreases. It decreases to 0.1163 at the maximum hottest-spot temperature of 132 °C that the transformer reaches due to Level I/II charging. As for Level III charging, this value decreases to 0.0339 at the highest hottest-spot temperature of 146 °C that the transformer attains. In both cases, the per-unit life is below 1 between the hours of 9 p.m. to 11:30 p.m., with the addition of 12 a.m. in Case 2. The value of life in per unit in Case 1 is 1.8075, while it is 0.5937 in Case 2. During the charging time from 12:30 a.m. to 4 a.m., the p.u. life increases in both cases due to decreasing charging load demand.

35
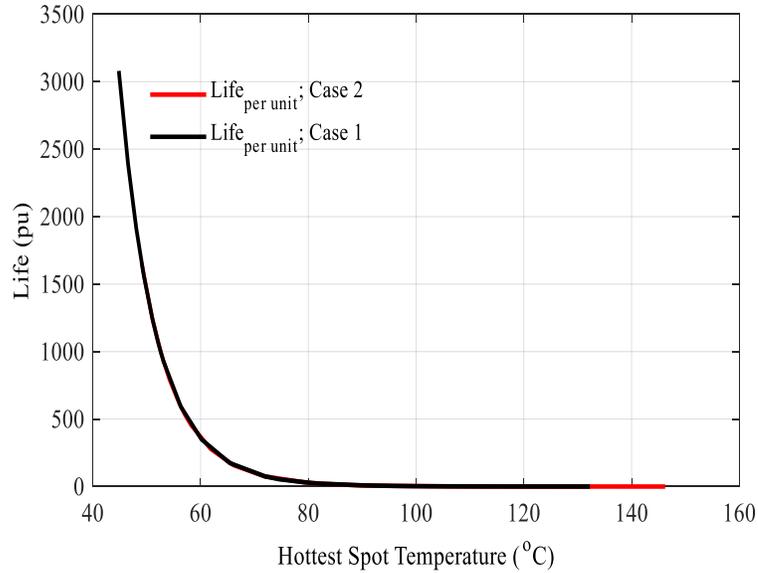
Fig. 3.16. Per-unit life in Cases 1 and 2.

The percent LOL is above the reference value of 0.0133% during the period of 9 p.m. to 11:30 p.m. At 9:30 p.m., it reaches the highest during the charging period; it is equal to 0.1147% at the hottest-spot temperature of 132 °C in Case 1. This value is greater in Case 2, reaching 0.3934% at the hottest-spot temperature of 147 °C.

This indicates that the transformer lifetime is impacted and decreases from the normal insulation life of 20.55 years during EV charging period, as presented in Fig. 3.18. In the case of a Level I/II charger, the transformer lifetime decreases to 14.27 years at 9 p.m. when charging starts. It decreases sharply to reach 2.39 years at 9:30 p.m. At midnight, the lifetime is not affected and continue being stable during the remaining charging cycle. For Level III charger, the transformer real-life decreases to 4.48 years at 9:00 p.m. when charging first starts, then sharply drops to 0.69 years at 9:30 p.m. The lifetime is also reduced at midnight to a value of 12.19 years. Starting from 12:30 a.m., it becomes stable due to low EV charging demand.

36
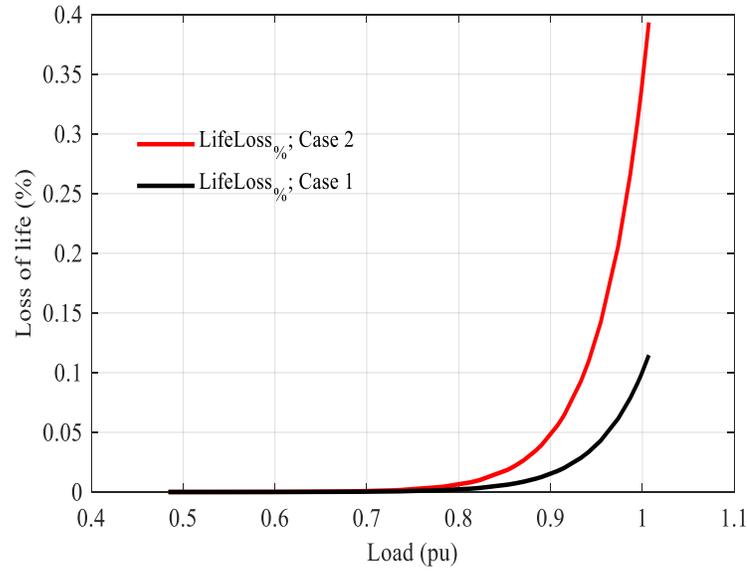
Fig. 3.17. Loss of life in Cases 1 and 2.
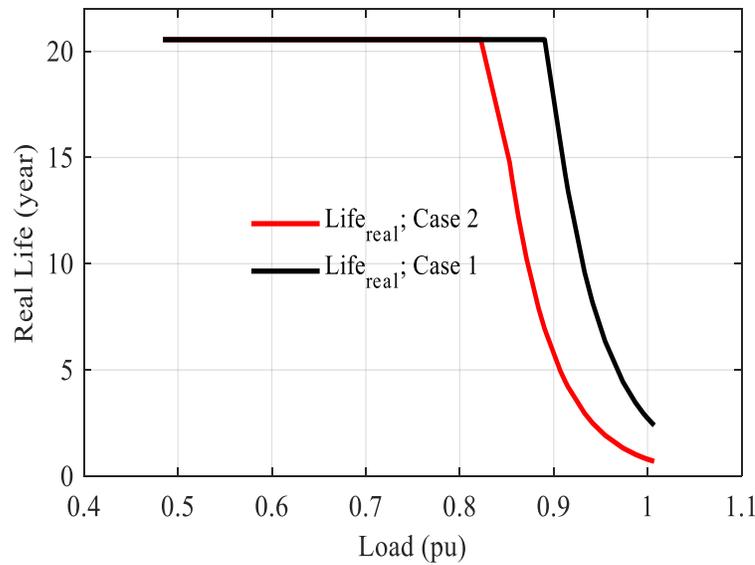
Fig. 3.18. Transformer real life in Cases 1 and 2.

It can be noted that the peak in losses, temperature rise, aging acceleration factor, and DT lifetime reduction occurs at 9:30 p.m. in this study, which is the period when the load demand of EV battery charging attains its maximum. The results also show that the harmonic components of Level III charging affect the transformer more severely than the harmonics of Level I/II charging [40].

37

CHAPTER 4

EV BATTERY CHARGING IMPACTS ON DISTRIBUTION SYSTEM

4.1 Introduction

Increased adoption of electrified vehicles and charging their batteries from the current distribution network without any plans of accommodating this extra load demand could result in critical quality issues related to the distribution of electric power [30]. Electrified vehicles offer a promising alternative to combustion engine driven automobiles to fight the growing concerns related to environmental pollution, climate change, and energy crisis, yet they impose harmful effects due to EV charging load on the operating parameters of the power system. DC charging infrastructures, demanding high charging currents, have adverse impacts on the grid operation. Reliability of the distribution network is an essential operating parameter, and its degradation can lead to consumers' inconvenience. The extra weight carried by EV loads on the network may affect the operating elements of the grid, including voltage stability, power loss, and harmonics [65]. To understand the new challenges that EVs impose on the power grid and to ensure that the power system is prepared to accommodate the increased load demand, it is important to conduct a comprehensive study of EV charging effects on the DS. Current harmonics injected by EV charging can lead to voltage deviation, voltage instability, voltage imbalance, power unbalance, system losses, as well as current and voltage harmonic distortions. Some components of the network, such as transformers and feeders can also experience overloading at high penetration levels of EVs [66].

Uncontrolled charging happens when consumers begin charging their EVs when they arrive home from work during the on-peak load hours, which can lead to serious overloading of the power grid. Overloading the transformer can have degrading effects on its life span. In low voltage distribution networks, voltage drop represents a critical concern and must remain as small as possible [67]. Uncoordinated charging of large-scale electrified cars can increase the presence of uncertain elements in the distribution network operation and result in technical and economic issues of the grid scheduling and control. EV charging load appears to be random compared to traditional power loads since users' preference of when and where to charge their EVs can vary. The impacts of charging loads become more harmful when charging occurs during on-peak load hours.

This section investigates the impacts of current harmonics due to EV charging loads on the distribution system in addition to other types of conventional loads. Power flow is firstly performed to provide a numerical analysis of the flow of electric power in normal steady-state operation and obtain AC power parameters including voltage magnitudes and phase angles at each bus, as well as real and reactive power flowing in each line. DHPF is a harmonic power flow method implemented in this section to estimate the harmonic distortion due to the presence of nonlinear devices such as EV battery charging. The problem is tested on the IEEE radial 33-bus distribution system in MATLAB.

4.2 Harmonic Power Flow Analysis

DHPF technique is popular due to its simplicity among other power flow methods. The procedure of this power flow solution is shown in the flow chart of Fig. 4.1. First, conventional power flow solution is obtained at the fundamental frequency for all loading conditions. The magnitudes of all values are expressed in per unit and the angles of complex quantities are given in radians. Then, these results are used to calculate the admittances of transmission lines and linear loads at higher-order harmonic frequencies. An admittance matrix is formulated for each harmonic order. EV parking lots are modeled as injecting harmonic current sources, and the current injected by each parking lot is calculated using the harmonic spectrum of a DC fast charger. Nodal equations are solved at each harmonic order to obtain the harmonic voltage profile at each bus.

The harmonic admittance of a linear load (γ_i^h) connected at a given bus i is presented in (4.1) and the harmonic admittance of a branch (γ_{ij}^h) connecting two buses i and j is given in (4.2):

$$\gamma_i^h = \frac{P_{D,i}}{\left|v_i^1\right|^2} - j\frac{Q_{D,i}}{h\left|v_i^1\right|^2} \tag{4.1}$$

$$\gamma_{ij}^h = \frac{1}{R_{ij} + jhX_{ij}} \tag{4.2}$$

where $P_{D,i}$ and $Q_{D,i}$ are the fundamental active and reactive load power demands at bus i, v_i^1 is the fundamental voltage at bus i, h is the harmonic order, R_{ij} is the branch resistance and X_{ij} is the branch reactance connected between buses i and j. The equivalent admittances, γ_i^h and γ_{ij}^h, are calculated using the conventional power flow results.

```
                    ┌─────────┐
                    │  h=1    │
                    └────┬────┘
                         ▼
        ┌────────────────────────────────────┐
        │  Conventional power flow solution of │
        │  system at maximum loading conditions│
        └────────────────┬───────────────────┘
                         ▼
                    ┌─────────┐
                    │  h=2    │
                    └────┬────┘
                         ▼
        ┌────────────────────────────────────┐
        │     Admittances of linear loads and  │
        │          transmission lines          │
        └────────────────┬───────────────────┘
                         ▼
        ┌────────────────────────────────────┐
        │  Harmonic admittance matrix Y^(h=2)  │
        └────────────────┬───────────────────┘
                         ▼
        ┌────────────────────────────────────┐
        │  Fundamental and 2nd harmonic currents│
        │  of PEV charging loads installed at bus i│
        │              of system               │
        └────────────────┬───────────────────┘
                         ▼
        ┌────────────────────────────────────┐
        │   Solve Decoupled Load Flow Equation:│
        │        V^h = (Y^h)^-1 I^h            │
        └────────────────┬───────────────────┘
                         ▼
                    ┌─────────┐
                    │  h=h+1  │
                    └────┬────┘
                         ▼
    No                ╱─────────╲
  ◄──────────────────◄ h < h_max ►
                      ╲─────────╱
                         │ Yes
                         ▼
        ┌────────────────────────────────────┐
        │   Voltage profile at each harmonic order│
        └────────────────────────────────────┘
```
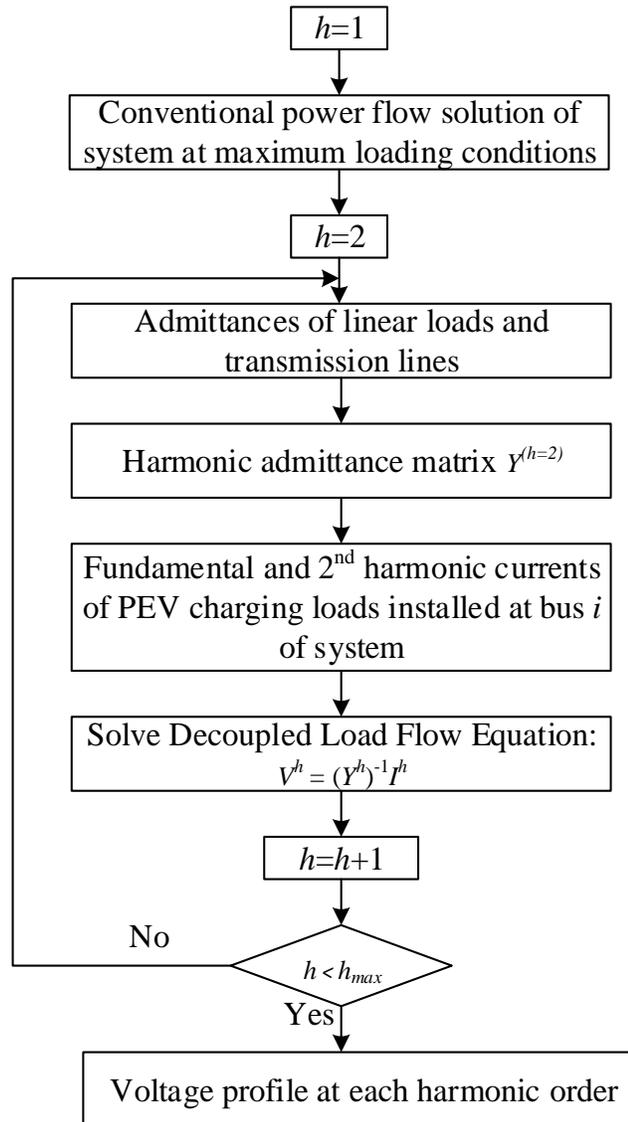
Fig. 4.1. Flowchart of the DHPF technique.

The power electronics circuit configuration of battery charging systems is formed by two converters: an AC/DC converter and a DC/DC converter. The AC/DC converter rectifies the AC voltage from the grid to a DC voltage and maintains a constant unity power factor. The DC/DC converter controls the delivered power to the battery pack, and the voltage rectification depends on the battery pack's voltage. Figure 4.2 shows the model of an EV battery charging system [68].

The EV loads are modeled with decoupled harmonic current sources. The fundamental

current I_i^1 and the hth harmonic order current I_i^h at bus i are given in (4.3) and (4.4), respectively.
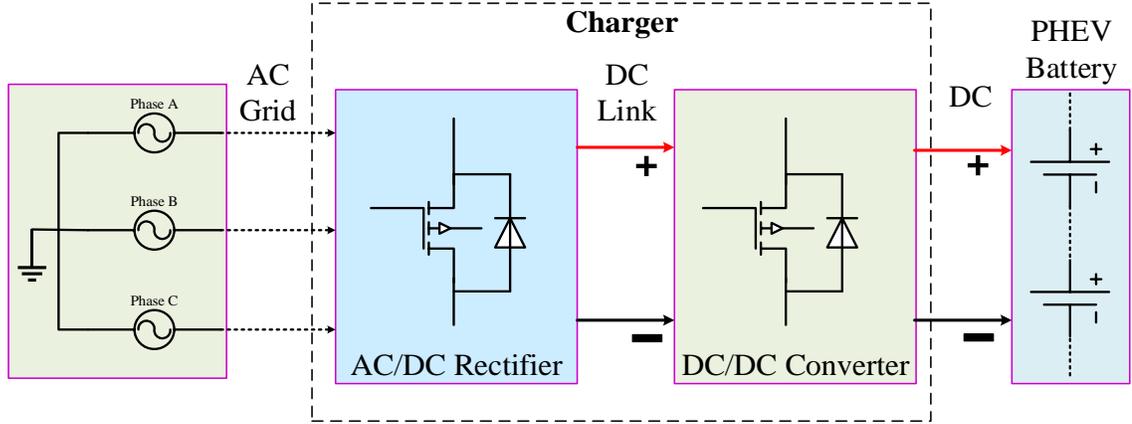
Fig. 4.2 EV battery charging system model.

$$I_i^1 = -\left[\frac{P_i + jQ_i}{|v_i^1|}\right]^*$$ (4.3)

$$I_i^h = \left(\frac{I_h}{I_1}\right)I_i^1$$ (4.4)

The harmonic voltages are determined by solving the decoupled load flow equation given in (4.5) [52]:

$$V_h = \left(Y^h\right)^{-1} I^h.$$ (4.5)

The THD due to EV battery charging is analyzed at the system level using the DHPF technique. Various types of linear loads, including residential, commercial and industrial loads, are connected at different buses of the IEEE 33-bus radial distribution system shown in Fig. 4.3, consisting of 33 buses and 37 branches (S1 – S37). The three types of power curves are shown in Fig. 4.4. EV charging loads, based on EV uncontrolled power profile shown in Fig. 4.4 [69], are installed at buses 15, 16, 22, and 24.

Residential loads are connected to each of buses #1, 2, 5, 9, 13, 14, 19, 23, 27, 29 and 32. Commercial loads are connected to buses #3, 6, 8, 10, 11, 18, 26, 28, 30 and 33. Industrial loads are connected to buses #4, 7, 12, 17, 20, 21 and 25 and 31. The total substation loads for the base configuration are 5084.26 kW and 2547.32 kVAr. The power flow data are obtained from Baran and Wu [70] and are loaded into MATPOWER, a package consisting of MATLAB M-files to solve power flow and optimal power flow problems. MATPOWER

41
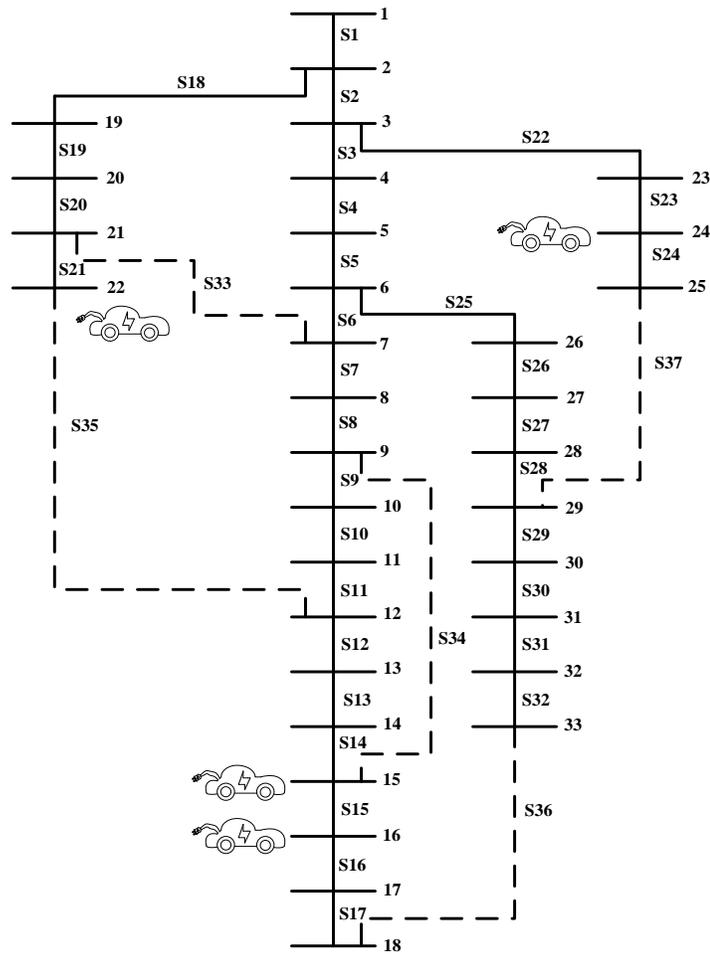
Fig. 4.3. The IEEE 33-bus radial distribution system with EV parking lots.

is a simulation tool used by researchers and instructors that is easy to understand and modify while providing the best performance possible. MATPOWER uses all the standard steady-state models typically used in power flow analysis [71]. The system data are given in Tables A.1 and A.2 of Appendix A, showing bus data and branch data, respectively. EV penetration level is taken as 15%, and the additional power demand required by each EV charger is calculated. Total complex power of the system is 4369.35 kVA. Since EV charging takes up 15% of the total load, i.e., 655.4 kVA, the power required for each EV load is 163.8 kVA, with four parking lots connected at each bus. This load is added to the existing power demand of buses #15, 16, 22, and 24. The power rating then becomes equal to 223.85 kW at each of buses #15 and 16. It is equal to 253.85 kW at bus #22 and equal to 583.85 kW at bus #24.

42
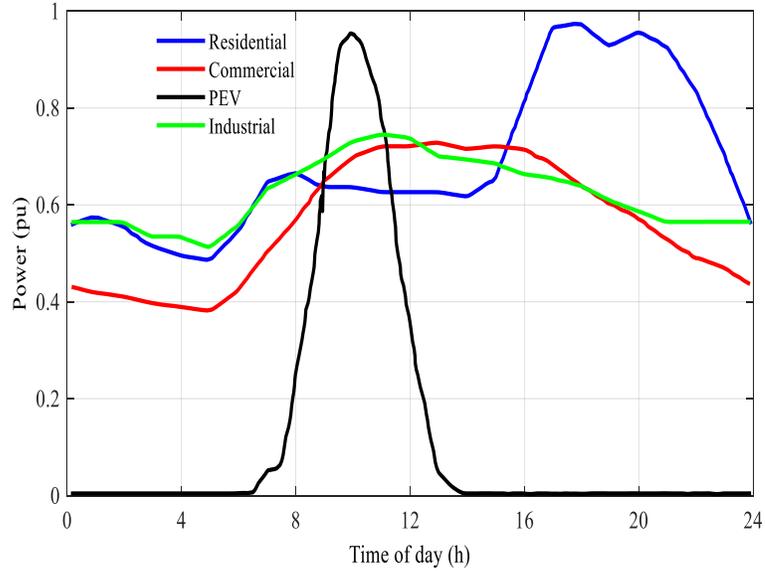
Fig. 4.4. Different types of load power profile.

4.3 Voltage Total Harmonic Distortion Profile for a Level III Charger

After running the conventional power flow results, the voltage magnitudes at each bus are obtained at the fundamental frequency at each hour within the day. The results are expressed in p.u. and shown in Fig. 4.5. The load admittance at each bus where a conventional load is connected is calculated using equation (4.1). This load admittance is equal to zero for buses #15, 16, 22 and 24 since an EV charging lot is connected at each bus and is represented by a current source. These quantities are also expressed in per unit. Next, the 32 by 32 harmonic admittance matrix consisting of diagonal elements and non-diagonal elements is formed at each order. A cell array is used to store 9 harmonic admittance matrices; one for each order. The fundamental current injected by EV chargers at buses #15, 16, 22 and 24 is obtained using (4.3). The fundamental current values at each bus where an EV charging lot is connected are given in Table 4.1 at different times within the day. Since EV charging does not occur during the periods from 1 a.m. till 7 a.m., and 1 p.m. till midnight, the fundamental current values are negligible.

43
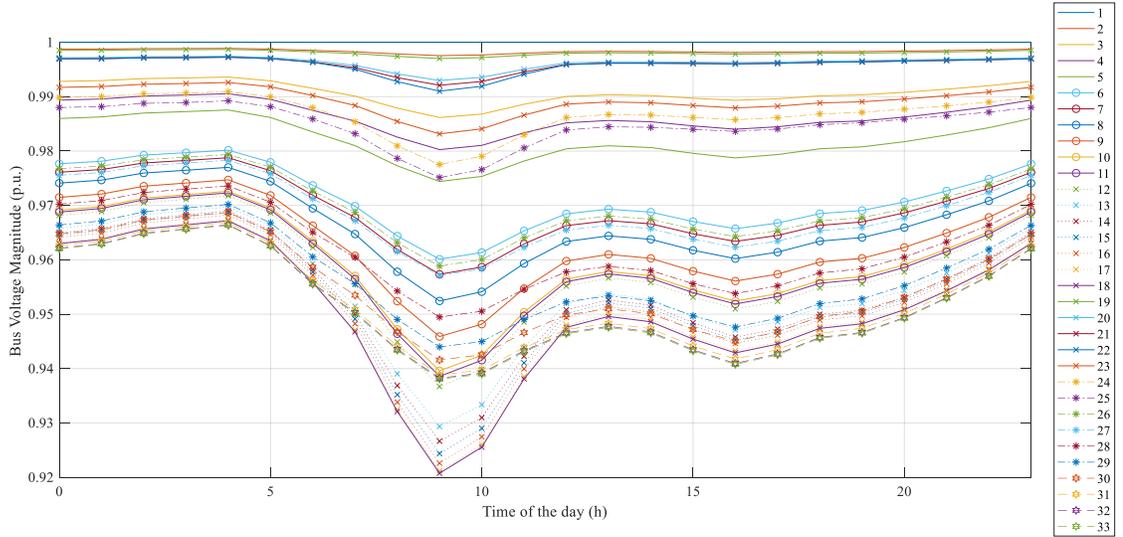
Fig. 4.5. Bus voltage magnitude profile at fundamental frequency.

TABLE 4.1. Fundamental Current at Each Bus during Charging Load Period.

Bus #	I (t=8 a.m.)	I (t=9 a.m.)	I (t=10 a.m.)	I (t=11 a.m.)	I (t=12 p.m.)
15	-0.0599	-0.1573	-0.2310	-0.1856	-0.0846
16	-0.0600	-0.1576	-0.2314	-0.1859	-0.0847
22	-0.0648	-0.1681	-0.2443	-0.1971	-0.0908
24	-0.1506	-0.3912	-0.5697	-0.4594	-0.2113

From the results, it can be observed that the fundamental current value at each bus from higher to lower occurs respectively at 10 a.m., 11 a.m., 9 a.m., 12 p.m. and 8 a.m. The fundamental current values rise when the charging load increases. Since the charging load at 10 a.m. reaches 0.95 p.u. and is at its highest, the fundamental current values are higher than those during other charging times.

The harmonic spectrum of a Level III EV charger is shown in Table 4.2 [7]. The hth harmonic order current is then found using (4.4).

TABLE 4.2. Harmonic Magnitudes for One Phase of Level III Charger.

Harmonic Order	Harmonic Ratio
3	0.0446
5	0.0441
7	0.0305
9	0.0332

The harmonic voltage at each bus is calculated after solving nodal equations. The harmonic voltage profile, at each bus and harmonic order, is computed using (4.5). The voltages previously obtained at the fundamental frequency are included in the voltage matrix storing

44

the harmonic voltage values. A for-loop is used to repeat the steps at a time interval of one hour throughout the day. The total harmonic distortion for voltage at each bus is estimated using equation (3.3). The maximum voltage THD for voltage occurs at bus #16 and is presented in Fig. 4.6 throughout 24 hours.
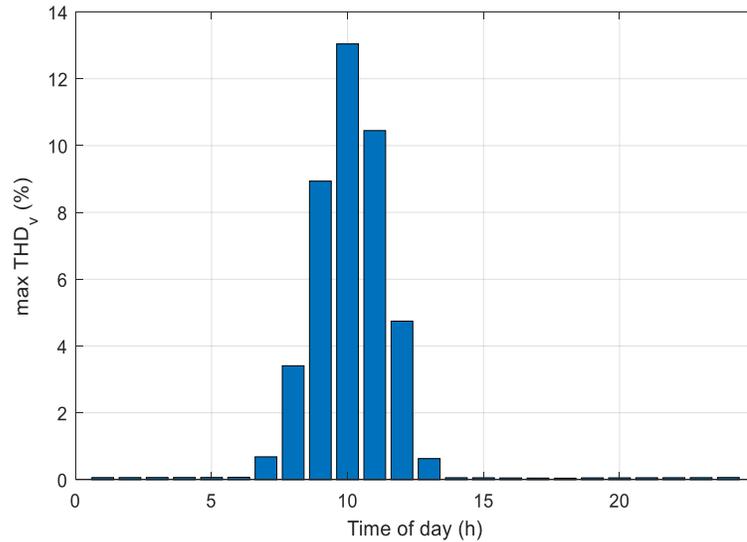
Fig. 4.6. THD for voltage at bus #16.

The THD for voltage values is very small from the period from 1 p.m. till 7 a.m. This is because EV charging load is negligible during this period. THD for voltage starts to rise at 8 a.m., reaching a value of 3.4%. At 9 a.m., it rises to 8.9%, attains its peak of 13.0% at 10 a.m., then decreases to 10.4% at 11 a.m., followed by a drop to 4.7% at 12 p.m. to decrease significantly once the charging period is over. The highest value of voltage THD occurs at 10 a.m. since EV charging load is at its peak value of 0.95 p.u. It can be noted that during the period of 9 a.m. until 11 a.m., the THD for voltage values violate the limit value of 5% set in IEEE 519 standards [72].

The second highest voltage disturbance occurs at bus #15. Figure 4.7 shows THD for voltage values obtained at bus #15 during one day.
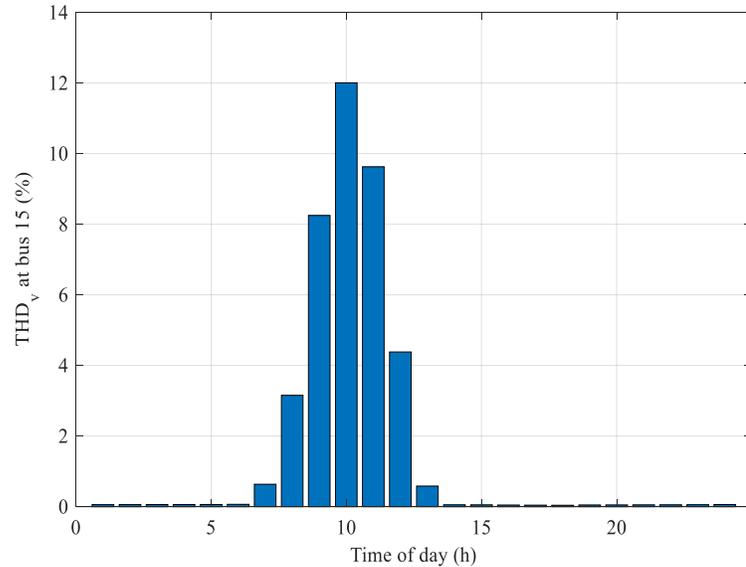
Fig. 4.7. THD for voltage at bus #15.

Similarly to the case of bus #16, the values are negligible from 1 p.m. till 7 a.m. This is because EV charging power curve is close to zero during this period. At 8 a.m., the value of THD for voltage attains 3.2%, followed by a rise to reach 8.2% at 9 a.m. THD for voltage at bus #15 is the highest at 10 a.m. with a value of 12.0%. This value then drops to 9.6% at 11 a.m., then decreases to 4.4% at 12 p.m. to drop significantly once the charging period is over. The THD for voltage values at bus #15 exceeds the limit value of 5% set in IEEE 519 during the time from 9 a.m. till 11 a.m.

The fourth highest voltage disturbance occurs at bus #24, at which a plug-in electric vehicle charging parking is connected. Figure 4.8 shows the THD for the voltage profile at this bus. The voltage disturbance at bus #24 is negligible during the time from 1 p.m. till 7 a.m. It slightly rises to 2.5% at 8 a.m., then to 6.5% at 9 a.m. It continues rising to reach 9.4% at 10 a.m., which is the highest value during the 24 hr cycle. It then decreases to 7.6% at 11 a.m. and 3.5% at noon, with the charging load decreasing to 0.77 p.u. and then to 0.36 p.u., respectively. The disturbance of voltage at bus #24 violates the limit of 5% set in IEEE 519 standards during the charging period from 9 a.m. till 11 a.m.

The fifth highest voltage disturbance takes place at bus #22 at which an EV charging lot is connected. The THD for voltage profile is given in Fig. 4.9 for this bus. The highest value

46
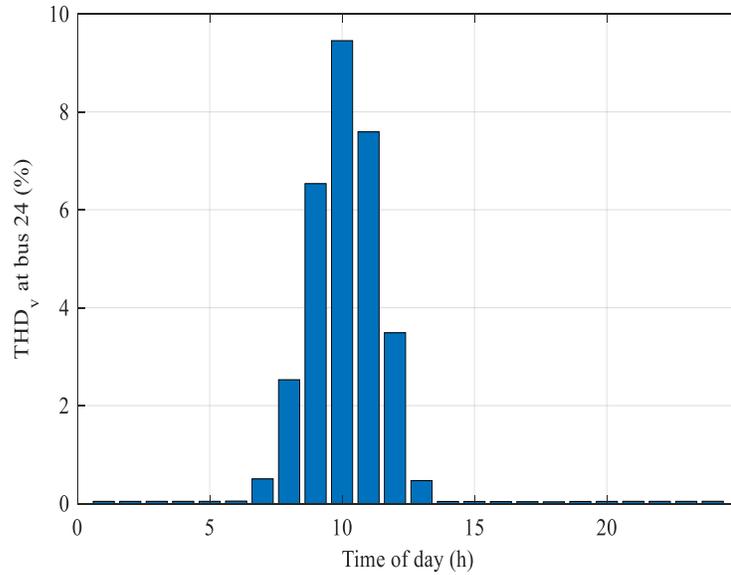
Fig. 4.8. THD for voltage at bus #24.

of THD for voltage happens at 10 a.m. and attains 8.8%. THD for voltage is negligible between the hours of 1 p.m. and 7 a.m. Once the charging power curve starts to rise at 8 a.m., THD for voltage rises to 2.4%, then to 6.1% at 9 a.m. From its maximum value of 8.8%, it decreases to 7.1% at 11 a.m., then sharply drops to 3.3% at noon. Similarly to the previous buses discussed, the disturbance values at this bus are beyond the limit value of 5% set in IEEE 519 during the period when the charging load is high.
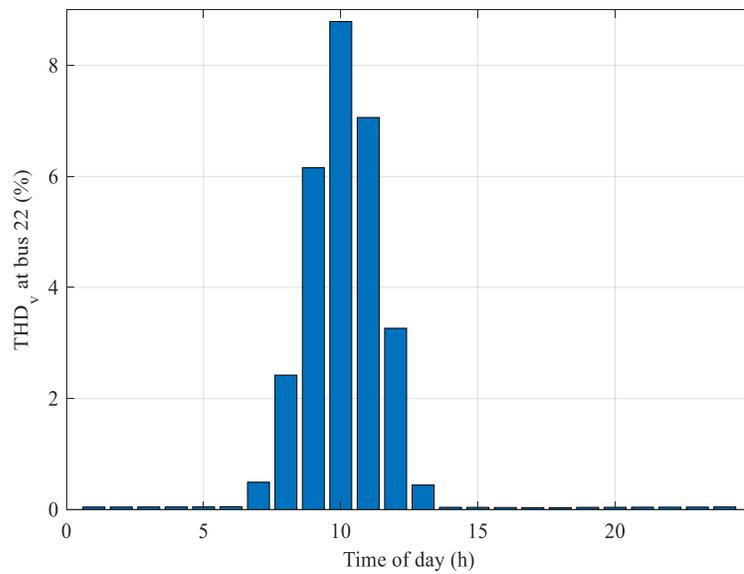
Fig. 4.9. THD for voltage at bus #22.

The disturbance of voltage is then evaluated at neighboring buses to where EV parking lots are located. Since the first charging parking is located at bus #15, the assessment is done at bus #14. The voltage THD at bus #14 is modeled and presented in Fig. 4.10. The disturbance at this bus attains the third highest. Despite not having an EV charging connected at this bus, the voltage disturbance at bus #14 exceeds the one occurring at each of buses #22 and 24, where EV parking lots are connected. This is because this bus is located near two charging lots located at buses #15 and 16. As the EV charging power curve starts to rise at 8 a.m., THD for voltage reaches 2.7%. It then increases to 6.9% at 9 a.m. with the increasing charging curve. At 10 a.m., it reaches 10.0%, then falls to 8.0% at 11 a.m. It sharply decreases to 3.7% at noon to become negligible during the period from 1 p.m. till 7 a.m.
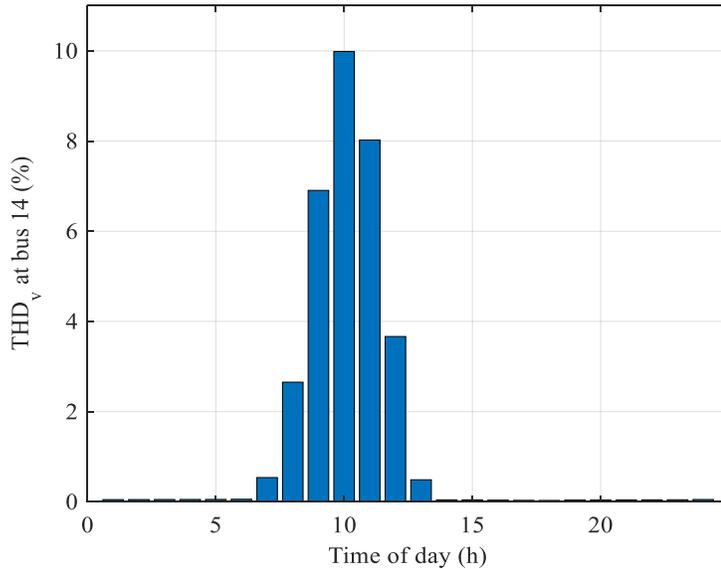
Fig. 4.10. THD for voltage at bus #14.

It can be further noted that during the peak charging load at 10 a.m., the voltage THD exceeding the limit of 5% occurs at the buses located at proximity to charging lots connected at buses #15 and 16. These buses are the following: 9, 10, 11, 12, 13, 16, and 17 (in addition to bus #14). These effects are due to having two charging lots connected at the same feeder. The two buses surrounding the parking lot connected at bus #24 are also affected. The THD for voltage values, however, remain below 5% at buses #23 (THD = 4.0% at 10 a.m.) and #25 (THD = 4.3% at 10 a.m.). Bus #21, located in close proximity to bus #22, experiences a voltage THD value of 4.9%, slightly below the 5% limit.

4.4 Current Total Harmonic Distortion Profile for a Level III Charger in addition to Conventional Loads

In addition to EV charging loads, conventional loads are connected at buses #15, 16, 22 and 24. The harmonic distribution of conventional loads is added to the harmonic spectrum of Level III charger. The total harmonic spectrum is shown in Table 4.3 [7].

TABLE 4.3. Total Harmonic Distribution of Conventional Loads and Level III Charging Load.

Harmonic Order	Harmonic Ratio
3	0.3947
5	0.2141
7	0.1506
9	0.1253
11	0.0710
13	0.0510
15	0.0430
17	0.0400
19	0.0390
21	0.0000
23	0.0320
25	0.0290

The same DHPF steps are repeated here. A cell array is used to store 24 matrices, each corresponding to a harmonic order.

The harmonic current at the main substation is then calculated as follows:

$$I_{ij}^{h} = \frac{(v_i^{h} - v_j^{h})}{z_{ij}^{h}} \tag{4.6}$$

$$= y_{ij}^{h}(v_i^{h} - v_j^{h})$$

$$= -Y_{ij}^{h}\left(v_i^{h} - v_j^{h}\right)$$

where I_{ij}^{h} is the current between buses i and j, v_i^{h} is the voltage at bus i, v_j^{h} is the voltage at bus j, z_{ij}^{h} and y_{ij}^{h} are respectively the impedance and the admittance of the feeder connecting buses i and j, Y_{ij}^{h} is the admittance matrix at harmonic order h.

The harmonic current at each order at the main substation at 10 a.m. is presented in Fig. 4.11. It can be observed that 3rd harmonic current is the highest among all the order, reaching a value of 0.1527 p.u. The 5th harmonic current is 0.0648 per unit and the 7th harmonic current is 0.0383. The harmonic current values continue to decrease with every harmonic order, except the 15th harmonic order, where the value increases slightly.
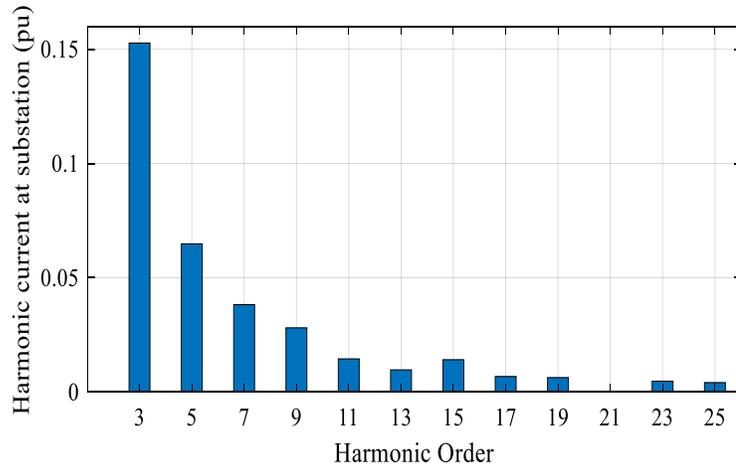
Fig. 4.11. Harmonic current at t = 10 a.m.

The current THD through the substation is then obtained using (3.4). The values at different times of the day are shown in Fig. 4.12.
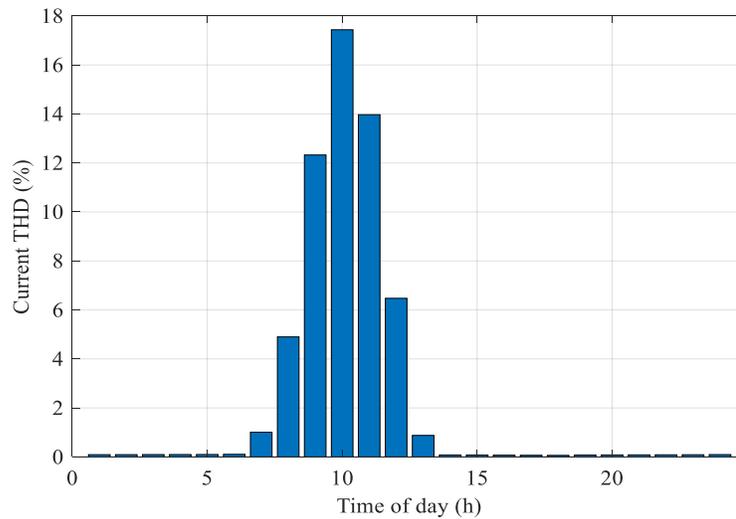
Fig. 4.12. Current THD profile through main substation.

From the figure, it can be observed that the current THD is negligible from 1 p.m. until 7 a.m. This is attributed to a very small EV charging load during this period. The disturbance rises to 12.3% at 9 a.m. At 10 a.m., the current disturbance is the highest, reaching a value of 17.4%. This happens when the EV charging profile is at its highest value of 0.9538 p.u. As the EV charging load value decreases to 0.7703 p.u. at 10 a.m. and then to 0.3557 p.u. at 11 a.m., the current THD declines to 14.0% and 6.5%, respectively.

According to the limits set by IEEE Std 519, the total demand distortion (TDD) limit for systems rated 120V through 69 kV with a $50 < \dfrac{I_{SC}}{I_L} < 100$ is specified as 12%, where I_{sc} is the maximum short-circuit current at PCC and I_L is the maximum demand load current at the PCC under normal load operating conditions. The TDD is defined as the ratio of the root mean square of the harmonic content, specified as a percent of the maximum demand current [72]. The current TDD is expressed in (4.7) [73]:

$$ I_{TDD} = \frac{\sqrt{I_3^2 + I_5^2 + I_7^2 + \ldots}}{I_L} \times 100\% . \tag{4.7} $$

The TDD occurs at 10 a.m. and exceeds the value of the limit set at 12%.

4.5 Voltage Total Harmonic Distortion Profile for a Level III Charger at Maximum Loading Conditions

At maximum loading conditions with $k_r = 0.97$, $k_c = 0.73$, $k_i = 0.74$, and $k_{ev} = 0.95$, where k_r, k_c, k_i, and k_{ev} correspond to the loading factors of the residential, commercial, industrial and EV loads, respectively, conventional power flow results are obtained. The power flow solution is stored in a structure that includes bus data, generator data, branch data, and generator cost data. Bus data including real power demand, reactive power demand, and voltage magnitude are displayed in p.u in Table 4.4. This data is inputted into DHPF methodology in higher-order harmonic frequencies. First, linear loads at each bus are represented as equivalent admittances to form a load admittance matrix. Next, admittances of the 37 branches at each harmonic order are obtained to form a branch admittance matrix. Using these results, a new 32*32 admittance matrix Y_{bus} is constructed with diagonal elements Y_{ii} and off-diagonal elements Y_{ij} given in (4.8) and (4.9), respectively:

$$ Y_{ii} = y_i + \sum_{k=1, k \neq i}^{N} y_{ik} \tag{4.8} $$

$$ Y_{ij} = Y_{ji} = -y_{ji} \tag{4.9} $$

In (4.8), y_{ik} exists when there is a physical connection between bus i and k. y_{ji} in (4.9) is the admittance of connecting buses i and j.

The general nodal admittance matrix form appears as given in (4.10).

$$Y_{bus} = \begin{pmatrix} Y_{11} & \cdots & Y_{1n} \\ \vdots & \ddots & \vdots \\ Y_{n1} & \cdots & Y_{nn} \end{pmatrix} \tag{4.10}$$

A cell array is then used to store the matrices at each harmonic order.

TABLE 4.4. Bus Data at Maximum Loading Conditions.

Bus #	Pd (p.u.)	Qd (p.u.)	Vm (p.u.)
1	0.000	0.000	1.000
2	0.097	0.058	0.997
3	0.066	0.029	0.984
4	0.089	0.060	0.978
5	0.058	0.029	0.971
6	0.044	0.015	0.954
7	0.149	0.074	0.951
8	0.146	0.073	0.946
9	0.058	0.019	0.938
10	0.044	0.015	0.931
11	0.033	0.022	0.930
12	0.045	0.026	0.928
13	0.058	0.034	0.920
14	0.117	0.078	0.917
15	0.214	0.000	0.914
16	0.214	0.000	0.913
17	0.045	0.015	0.911
18	0.066	0.029	0.911
19	0.088	0.039	0.997
20	0.067	0.030	0.993
21	0.067	0.030	0.992
22	0.242	0.000	0.991
23	0.088	0.049	0.981
24	0.557	0.000	0.976
25	0.313	0.149	0.973
26	0.044	0.018	0.953
27	0.058	0.024	0.951
28	0.044	0.015	0.942
29	0.117	0.068	0.935
30	0.146	0.437	0.932
31	0.112	0.052	0.929
32	0.204	0.097	0.928
33	0.044	0.029	0.928

The EV loads are modeled as harmonic current injecting sources using (4.3). Table 4.5 shows the fundamental current injected by each EV load.

TABLE 4.5. Fundamental Current Injected by EV Loads at Each Bus in P.U.

Bus #	I^1
15	-0.2335
16	-0.2340
22	-0.2444
24	-0.5708

Next, using equation (4.4), the hth harmonic order current is obtained for the 3rd, 5th, 7th, and 9th order, as given in Table 4.6.

TABLE 4.6. hth Harmonic Order Current at Each Bus in P.U.

Bus #	I (h=3)	I (h=5)	I (h=7)	I (h=9)
15	-0.0104	-0.0103	-0.0071	-0.0078
16	-0.0105	-0.0103	-0.0072	-0.0078
22	-0.0109	-0.0108	-0.0075	-0.0081
24	-0.0255	-0.0252	-0.0175	-0.0190

Nodal equations are solved for each harmonic order to obtain the harmonic voltage using (4.5). The harmonic voltage values are converted from rectangular to polar forms to calculate the voltage magnitudes. This harmonic voltage profile is given in Table 4.7.

Using (3.3), voltage THD is obtained at each bus, as shown in Fig. 4.13. The highest THD for voltage reaches a value of 11.9% at bus #16. The second highest THD for voltage reaches 10.6% and occurs at bus #15. The third highest THD for voltage occurs at bus #24 with a value of 9.3%. The fifth highest THD for voltage occurs at bus #22 with a value of 8.2%. These high THD values are caused by the non-linearity of EV chargers connected at each of the four buses. The fourth highest THD for voltage takes place at bus #14. This bus is affected due to its proximity to the two parking lots located at buses #15 and 16. IEEE 519 limits the total harmonic voltage distortion on power systems 69 kV and below to 5% [74]. Buses #10, 11, 12, 13, and 17 have voltage disturbance above the 5% limit. The remaining buses remain below this limit.

TABLE 4.7 Harmonic Voltage at Each Bus in P.U.

Bus #	V (h=3)	V (h=5)	V (h=7)	V (h=9)
1	0.0000	0.0000	0.0000	0.0000
2	0.0017	0.0019	0.0015	0.0019
3	0.0081	0.0096	0.0078	0.0097
4	0.0082	0.0092	0.0070	0.0083
5	0.0087	0.0094	0.0068	0.0077
6	0.0115	0.0122	0.0084	0.0088
7	0.0142	0.0155	0.0107	0.0112
8	0.0168	0.0183	0.0127	0.0133
9	0.0241	0.0271	0.0197	0.0217
10	0.0259	0.0299	0.0221	0.0248
11	0.0263	0.0303	0.0225	0.0253
12	0.0273	0.0315	0.0235	0.0264
13	0.0317	0.0375	0.0287	0.0332
14	0.0357	0.0432	0.0337	0.0398
15	0.0426	0.0533	0.0435	0.0537
16	0.0458	0.0586	0.0491	0.0623
17	0.0254	0.0279	0.0210	0.0248
18	0.0194	0.0199	0.0141	0.0157
19	0.0031	0.0037	0.0029	0.0035
20	0.0159	0.0190	0.0148	0.0178
21	0.0208	0.0250	0.0196	0.0235
22	0.0341	0.0440	0.0368	0.0468
23	0.0155	0.0201	0.0173	0.0225
24	0.0340	0.0471	0.0421	0.0558
25	0.0187	0.0223	0.0177	0.0213
26	0.0115	0.0121	0.0083	0.0087
27	0.0115	0.0121	0.0084	0.0088
28	0.0125	0.0132	0.0092	0.0099
29	0.0137	0.0146	0.0104	0.0115
30	0.0118	0.0122	0.0085	0.0091
31	0.0123	0.0118	0.0076	0.0075
32	0.0131	0.0124	0.0078	0.0077
33	0.0157	0.0153	0.0100	0.0104
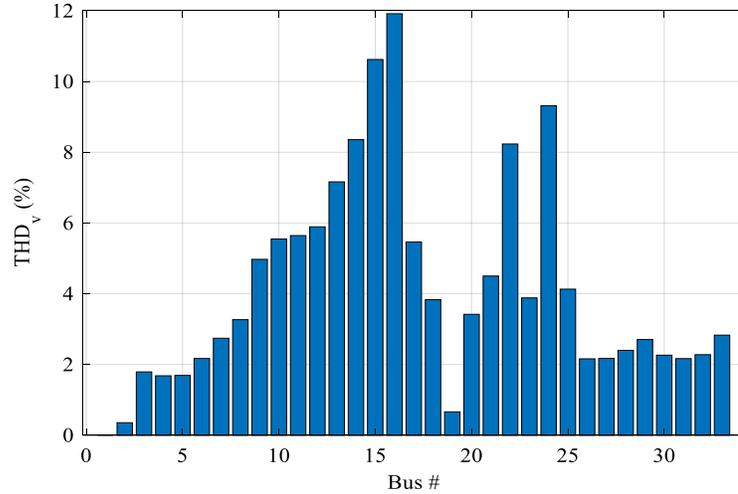
Fig. 4.13. THD for voltage at maximum loading conditions.

4.6 Voltage Total Harmonic Distortion Profile for a Level I/II Charger at Maximum Loading Conditions

The harmonic power flow is utilized to analyze the THD for voltage of a Level I/II battery charger at maximum loading conditions. Table 4.8 [7] shows the harmonic spectrum of the charger used in parking lots connected at the same buses as in the previous case study. First, the previously computed conventional network power flow results are used as inputs of the DHPF algorithm. Since the bus data results are equivalent to the previous case, load and branch admittances at each bus are equivalent to the ones of the previous case for every harmonic order. As a result, the Y_{bus} admittance matrix of the system at each harmonic order is equivalent to the admittance matrix found previously. The fundamental current injected by each EV load is also equivalent to the one previously calculated.

TABLE 4.8. Harmonic Magnitudes for Level I/II Charger.

Harmonic Order	Harmonic Ratio
3	0.0233
5	0.0282
7	0.0199
9	0.0128

Next, the hth harmonic order current is obtained in per unit for the 3rd, 5th, 7th, and 9th order, as presented in Table 4.9.

TABLE 4.9. *h*th Harmonic Order Current at Each Bus in P.U.

Bus #	I (h=3)	I (h=5)	I (h=7)	I (h=9)
15	-0.0054	-0.0066	-0.0046	-0.0030
16	-0.0054	-0.0066	-0.0047	-0.0030
22	-0.0057	-0.0069	-0.0049	-0.0031
24	-0.0133	-0.0161	-0.0114	-0.0073

After solving the nodal equations at each harmonic order, the harmonic voltage at each bus is calculated using (4.5). The values are then converted from rectangular to polar forms to find the voltage magnitudes, as shown in Table 4.10.

Using equation (3.3), voltage THD is obtained at each bus. This is shown in Fig. 4.14. The highest THD for voltage reaches a value of 6.5% at bus #16. The second highest THD for voltage has a value of 5.9% and occurs at bus #15. The third highest THD for voltage occurs at bus #24 with a value of 5.0%. The fifth highest THD for voltage occurs at bus #22 with a value of 4.5%. These THD values are caused by the non-linearity of EV parking lots connected at each of the four buses. The total harmonic distortion for voltage exceeding the limited value of 5%, set in IEEE 519 standards occurs at buses #15, 16, and 24, where the EVs are connected.

The remaining buses fall below this limit. When comparing the voltage disturbance caused by a Level III charger to the disturbance produced by a Level I/II charger, it is observed that the buses are more severely impacted by the current harmonics injected by a Level III charger. The total harmonic distortion for voltage is higher at every bus for a Level III charger than it is for a Level I/II charger. The ratio of the voltage THD occurring in a Level III charger compared to a Level I/II charger is between 1.75 and 1.84. The Level III charger has a higher disturbance than the Level I/II charger as the harmonic order currents are greater for the former one than the latter one. This occurs since the harmonic spectrum of a Level III charger has higher values than a Level I/II charger.

TABLE 4.10. Harmonic Voltage at Each Bus in P.U.

Bus #	V (h=3)	V (h=5)	V (h=7)	V (h=9)
1	0.0000	0.0000	0.0000	0.0000
2	0.0009	0.0012	0.0010	0.0007
3	0.0042	0.0061	0.0050	0.0037
4	0.0043	0.0059	0.0046	0.0032
5	0.0045	0.0060	0.0044	0.0030
6	0.0060	0.0078	0.0055	0.0034
7	0.0074	0.0099	0.0070	0.0043
8	0.0088	0.0117	0.0082	0.0051
9	0.0125	0.0173	0.0128	0.0083
10	0.0135	0.0191	0.0144	0.0095
11	0.0137	0.0194	0.0146	0.0097
12	0.0142	0.0201	0.0153	0.0101
13	0.0165	0.0240	0.0187	0.0127
14	0.0186	0.0276	0.0219	0.0153
15	0.0222	0.0340	0.0283	0.0206
16	0.0239	0.0374	0.0319	0.0239
17	0.0132	0.0178	0.0137	0.0095
18	0.0101	0.0127	0.0091	0.0060
19	0.0016	0.0023	0.0019	0.0013
20	0.0083	0.0121	0.0097	0.0068
21	0.0108	0.0159	0.0127	0.0090
22	0.0178	0.0281	0.0240	0.0180
23	0.0081	0.0129	0.0113	0.0086
24	0.0177	0.0301	0.0273	0.0214
25	0.0098	0.0142	0.0115	0.0082
26	0.0060	0.0077	0.0054	0.0034
27	0.0060	0.0077	0.0054	0.0034
28	0.0065	0.0084	0.0060	0.0038
29	0.0071	0.0093	0.0068	0.0044
30	0.0062	0.0078	0.0055	0.0035
31	0.0064	0.0075	0.0049	0.0029
32	0.0068	0.0079	0.0051	0.0030
33	0.0082	0.0098	0.0065	0.0040
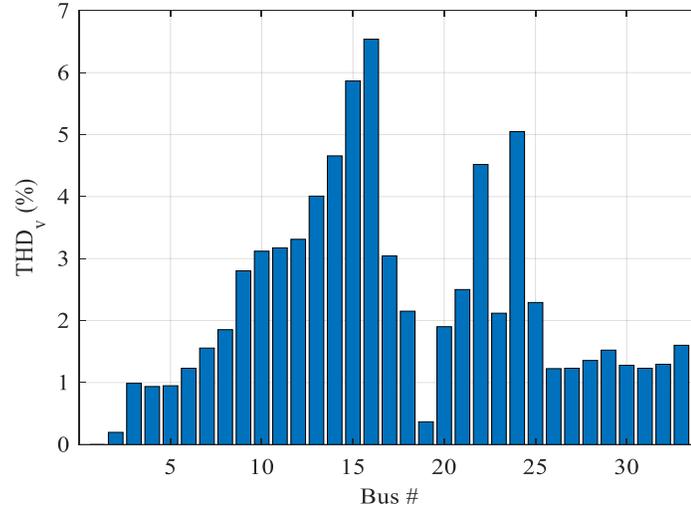
Fig. 4.14. THD for voltage at maximum loading conditions.

4.7 Voltage Total Harmonic Distortion Profile for a Level I/II Charger

Next, the results are computed for a cycle of 24 hours. The load admittances and branch admittance values remain the same as the ones for a Level III charger. As a result, the harmonic admittance matrix at each order is the same as the ones obtained in a Level III charger. In addition, the fundamental current values injected by each EV charger remain the same as a Level III charger. Since the harmonic spectrum is different for a Level I/II charger, the hth harmonic order current at each hour is different than it is in a Level III charger.

Since the highest THD for voltage occurs at bus #16, a plot of THD for voltage at this bus is presented in Fig. 4.15 at different times of the day. The values are negligible between the time period from 1 p.m. until 7 a.m. in the figure. During this time period, EV loads are very small, and thus, the effect on voltage distortion is negligible. The THD value slightly increases to 1.9% at the charging load of 0.25 p.u at 8 a.m. With an EV loading factor of 0.65 p.u., voltage distortion goes up to 4.9% at 9 a.m. It reaches the maximum value of 7.2% at 10 a.m. during the highest EV loading factor of 0.95 p.u., and drops to 5.7% as the EV loading point goes down to 0.77 p.u. at 11 a.m. The value drops once again to 2.6% at noon, with a loading factor of 0.35 p.u. The total harmonic distortion for a voltage limit of 5% is violated at bus #16 at 10 a.m. and 11 a.m. as per IEEE 519 standards.
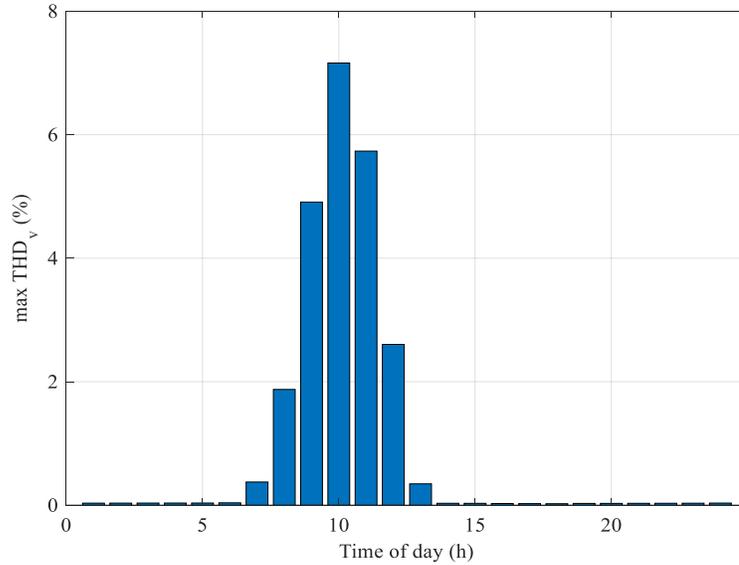
Fig. 4.15. THD for voltage at bus #16.

The second highest voltage disturbance at bus #15 is modeled in Fig. 4.16. The maximum THD for voltage occurs at 10 a.m. and reaches the value of 6.6%. From 1 p.m. until 7 a.m., the disturbance is minimal, since consumers do not charge their EVs during this period. Charging load increases at 8 a.m. resulting in a THD value of 1.7% then increases to 4.6% at 9 a.m. At 11 a.m., it decreases to 5.3% then drops to 2.4% at noon. Similarly to bus #16, the distortion for voltage exceeds the limit of 5% from 10 a.m. until 11 a.m. When comparing the disturbance caused by a Level III charger to the one of a Level I/II charger, it can be observed that bus #15 is more impacted in the first case than it is in the second case at all times. Furthermore, the limit at 9 a.m. is only violated in the first case, and the THD for voltage remains below the limit at this time in the second case.
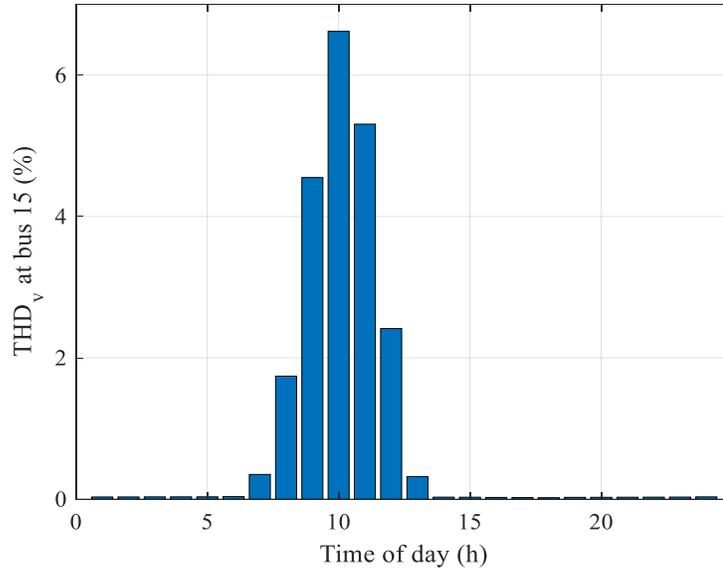
Fig. 4.16. THD for voltage at bus #15.

Bus #24 is the fourth most impacted by the current harmonics injected due to Level I/II charging. In Fig. 4.17, THD for voltage value is 5.1% at 10 a.m. This value remains below the limit at all other times; first starting at 1.4% at 8 a.m., increasing to 3.5% at 9 a.m., reaching its maximum at 10 a.m., followed by a drop to 4.1% at 11 a.m., and significantly dropping to 1.9% at noon. The disturbance remains below the 5% limit in this case at all times except 10 a.m. when using a Level III charger.
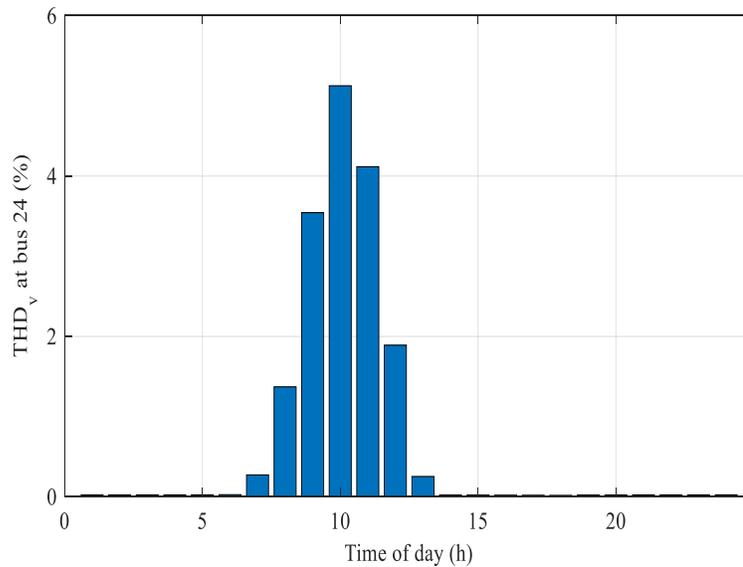
Fig. 4.17. THD for voltage at bus #24.

The voltage profile of bus #22 is shown in Fig. 4.18. This bus experiences the fifth-highest voltage disturbance among all buses. With a value of 4.8%, this bus remains below the limit of 5% at 10 a.m. Unlike the previous case of the Level III charger, this bus remains below the limit from 9 a.m. until 11 a.m.
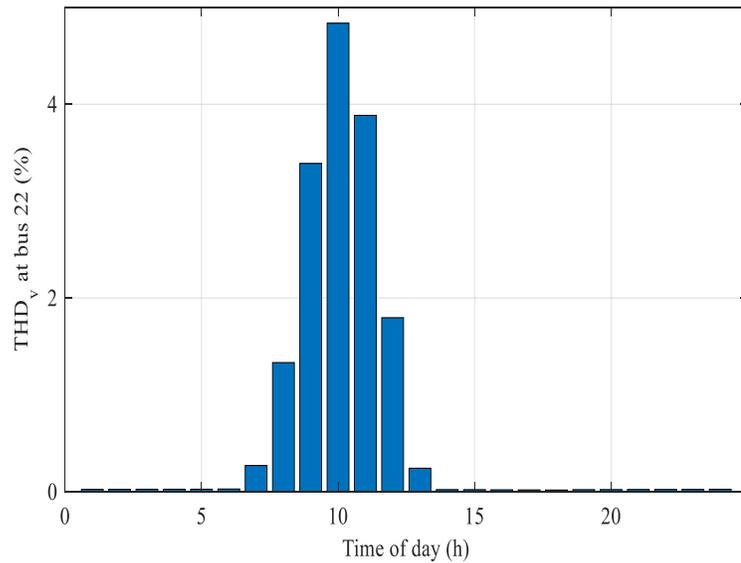
Fig. 4.18 THD for voltage at bus #22.

Despite not having any EVs connected at bus #14, it experiences the third-highest voltage disturbance. The THD at this bus has a value of 1.5% at 8 a.m., increases to 3.8% at 9 a.m., and reaches 5.5% at 10 a.m. The disturbance at 10 a.m. exceeds the limit of 5% at this bus. It falls to 4.4% at 11 a.m., then significantly drops to 2.0% at noon. This bus is more impacted by current harmonics than bus #22 and bus #24 at which an EV parking lot is connected. This is a result of its location close to two parking lots located at buses #15 and 16. This bus experiences the third-highest THD in this case and in the case of a Level III charger. However, THD is higher than the limit in this case only at 10 a.m. Although neighboring buses each have a THD exceeding the limit of 5% at 10 a.m. with a Level III charger, they remain below the limit in this case. In other words, buses #9, 10, 11, 12, 13, and 17 do not violate the standard limit of 5% here. The remaining buses are below the limit in both cases since they are located far from the non-linear loads. Figure 4.19 shows the THD profile at bus #14.
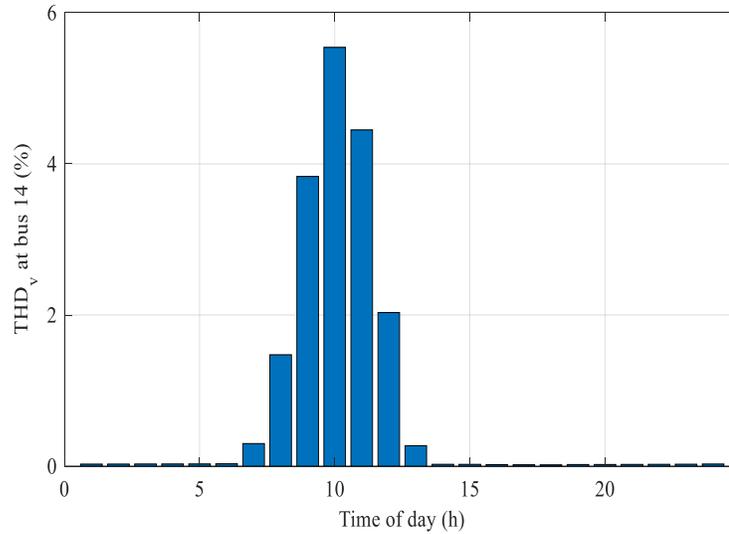
Fig. 4.19. THD for voltage at bus #14.

4.8 Current Total Harmonic Distortion Profile for a Level I/II Charger in addition to Conventional Loads

An assessment is performed to calculate the harmonic currents in the presence of traditional conventional loads. The total harmonic distribution of these loads for a Level I/II charger is shown in Table 4.11 below.

TABLE 4.11. Total Harmonic Distribution of Conventional Loads for Level I/II Charger.

Harmonic Order	Harmonic Ratio
3	0.3733
5	0.1982
7	0.1399
9	0.1048
11	0.0710
13	0.0510
15	0.0430
17	0.0400
19	0.0390
21	0.0000
23	0.0320
25	0.0290

After performing the DHPF algorithm and obtaining 24 matrices, the harmonic current is calculated at the main substation at the time the EV power curve reaches its maximum. This current is presented in Fig. 4.20 below.

62
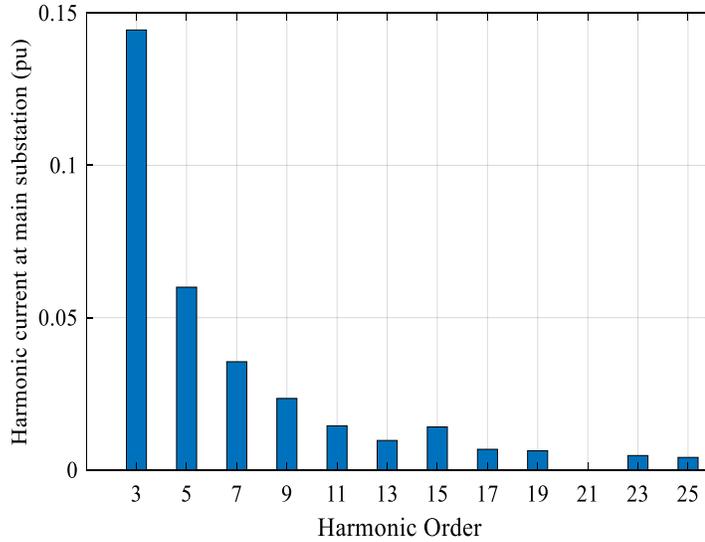
Fig. 4.20. Harmonic current at each order at t = 10 a.m.

The 3rd harmonic current takes the value of 0.1444 per unit. The 5th harmonic has a value of 0.0600 per unit. With every harmonic order, the value becomes smaller. After the 13th harmonic, the value increases to 0.0141 per unit at the 15th harmonic. It then continues to decrease to reach 0.0041 p.u. at the 25th harmonic. At every harmonic current, each order has a smaller value than the one produced with a Level III charger.

Next, the current THD through the main transformer is calculated using equation (3.4). The current THD profile is given in Fig. 4.21. The disturbance increases to 4.6% at 8 a.m. and reaches 11.6% at 9 a.m. The current disturbance is the highest at 10 a.m., reaching a value of 16.4%. This happens when the EV charging profile is at its highest value of 0.9538 per unit. As the EV charging load value decreases to 0.7703 p.u. at 11 a.m. and then to 0.3557 p.u. at 12 p.m., the current THD declines to 13.1% and 6.1%, respectively. In this case, the TDD exceeds the limit set by the standards [72]. The current disturbance with a Level III charger is higher than the current disturbance caused by Level I/II battery charger.
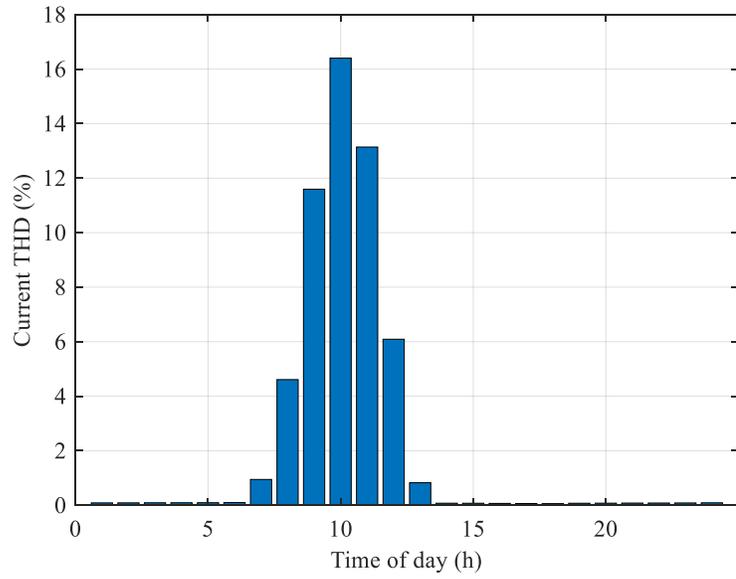
Fig. 4.21. Current THD profile through main substation.

CHAPTER 5

EV BATTERY CHARGING HARMONIC COMPENSATION THROUGH PV-BASED DISTRIBUTED GENERATION UNITS

5.1 Active Distribution Networks

Active distribution networks contribute to increasing the utilization level of renewable energy, and achieving a flexible intelligent distribution network management. ADN is a two-way power supply distribution network developed with large-scale distribution generators integrated into the power grid [75]. In addition to smart grids and microgrids, distributed generation and active distribution networks represent innovative tools to modernize the power system and ease the shift towards modern Power Distribution systems. Renewable energies constitute alternative resources to fossil fuels. The increased load demand, the phenomenon of climate change caused by greenhouse gas effects, and the high costs of oil are motivating factors to facilitate renewable energy generation. Renewable energy generation can lower carbon emissions and improve the air quality leading to a greener environment. Wind and solar power generation are increasing, especially in modern countries such as Japan, Sweden, and England. Distributed generators are small-size renewable energy power plants near loads that are integrated in the distribution network, modifying its topology from passive to active. Substations are the source of passive distribution networks which allow electrical power to flow through the feeder to reach the load. Power consumption and impedance of the connecting network are the only elements that affect the electrical current in passive networks. In addition, the injected power from distributed generators impacts the electrical current in active networks. The conventional distribution system is designed to allow uni-directional power flow, while distributed generators allow bi-directional power flow. ADNs can utilize distributed renewable generations, electrified vehicles, community energy storages, and demand responses to adaptively adjust their loads to meet the operation requirements [76]. A rise in the number of small-scale renewable energy sources such as photovoltaic arrays and wind turbines used in low-voltage distribution networks is predicted to lower greenhouse gas emissions and reduce harmful environmental problems. In places like Malaysia where high solar irradiance is present, PV arrays are widely used as renewable energy sources and PV penetration is anticipated to rise on the low-voltage networks as a

result of government incentives and plans [77]. In Germany, PV capacity has exceeded 35 GW, and most of it is distributed in the form of rooftop solar. Distributed generation attained over 50% in Denmark in 2014 with over 80% of heating supply provided by distributed combined heat and power. Distributed renewable generation is expected to rise with the development of distributed resources and energy policies encouraging demand side. A 20% carbon emission reduction goal by 2030 was set by the United States and China [78]. Distributed generators help improve the reliability of consumer power supply by increasing electric energy quality and reducing the load on the main grid [79].

5.2 Distributed Generation

The IEEE defines distributed generation as "the generation of electricity by facilities that are sufficiently smaller than central generating plants to allow interconnection at nearly any point in a power system" [8]. Distributed generation units can be classified based on the interface, output power, and energy source. The energy source can be fossil fuels such as diesel engines and micro-turbines, electro-chemical such as fuel cells, storage devices such as batteries and flywheels, or renewable energies such as solar, wind, and hydro. DGs can be categorized as dispatchable or non-dispatchable depending on the output power. Dispatchable DGs are divided into two groups: synchronous-machine based such as biomass and NGDG, and inverter-based such as fuel-cells and micro-turbines. The output power of these dispatchable DGs is assumed to be constant in normal operating mode [80].

Renewable resources do not have a unique model but are rather modeled using different topologies to describe their output. This is a result of their high level of uncertainty and variability. Renewable resources can be modeled using probabilistic analytical models, probabilistic chronological models, and time-series models. Renewable DGs have been regarded as a vital resource to overcome the challenges associated with power generation and the recent reorganization of energy systems [8]. For decades, power generation has mainly depended on large power stations such as coal, nuclear, and gas stations. Utilizing small and medium-sized generation units has become a non-pollutant key option since 1970. These distributed generators include Combined Heat and Power, small hydro, wind, and solar power generation and can be integrated into the distribution network near the consumers [81]. The integration of DGs raised in 1978 in response to the passage of the

PURPA, allowing qualifying facilities to install small generators in the utility system [82]. Installing DGs can offer many technical and economic advantages to the local distribution company and the consumers, including [81]:

- Reduced electrical losses due to shorter electricity travel path
- Increased reliability of power supply during power system failure
- Lower demands on high voltage transmission networks
- Improved power quality and reliability
- Increased energy security
- Improved voltage profile
- Reduced emissions of pollutants and enhanced environment air quality
- Deferral of transmission and distribution infrastructure investments
- Lower fuel costs due to increased overall efficiency

Numerous modern technologies use renewable energy resources. Technologies including biomass systems, photovoltaics, solar-thermal-electric-systems, WECS, and geothermal systems are promising for DG applications. DGs can range from a few kilowatts up to 100 MW. The smaller units, with rating ranging from a few kilowatts to a few megawatts, are normally connected to distribution networks [83].

5.3 PV Array Modelling

PV arrays consist of a string, several PV modules connected in series, and many strings connected in parallel to obtain a desired current and voltage. The equivalent circuit of a PV cell consists of a current source that is connected in parallel with a diode, as shown in Fig. 5.1.
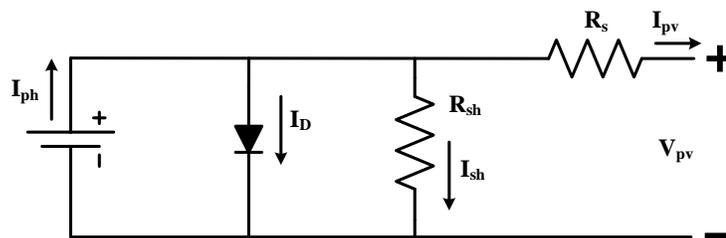
Fig. 5.1. Electrical equivalent circuit model of PV cell.

PV output current I_{PV} can be found using

$$I_{PV} = I_{PH} - I_D - I_{sh} \tag{5.1}$$

$$I_D = I_0 \left(e^{q\frac{(V_{PV} + I_{PV}R_S)}{\eta kT}} - 1 \right) \tag{5.2}$$

$$I_{sh} = \frac{V_{PV} + I_{PV}R_S}{R_{sh}} \tag{5.3}$$

where q, k, n, and T are the electronic charge, ideality factor of the diode, Boltzmann constant, and temperature in Kelvin, respectively. I_{ph} is photocurrent, I_0 is diode reverse saturation current, I_{PV} is the PV output current, and V_{PV} is the PV output voltage. Since R_{sh} has a very large value, its effect is negligible on the I-V characteristics of the PV array. Thus, equation (5.1) can be represented as follows:

$$I_{PV} = I_{ph} - I_0 \left(e^{q\frac{(V_{PV} + I_{PV}R_S)}{\eta kT}} - 1 \right) \tag{5.4}$$

Equation (5.5) is used to model a PV array consisting of N_s series and N_p parallel-connected PV modules [84]:

$$I_{PV} = N_p \left\{ I_{ph} - I_0 \left(e^{q\frac{(V_{PV} + I_{PV}R_S)}{\eta kT}} - 1 \right) \right\} \tag{5.5}$$

The grid-connected PV system consists of PV arrays, inverters, and controllers. The inverter constitutes an important element that provides output control of the PV system. The grid-connected PV system can be divided into single-stage and two-stage systems. A single-stage system is composed of PV array, a dc/ac inverter, a controller, a static switch, and local loads. The main function of a single-stage system is to convert the DC current produced by the PV array to an AC current with the inverter and feed it into the grid. In addition to the PV array, dc/ac inverter, controller, static switch, and the local loads, a two-stage grid-connected PV system is formed of a dc/dc converter and energy storage system. In the case of this system, the direct current produced by the PV array is transformed to another voltage level before being converted to an AC current through inverter feeding into the grid. The inverter is an important interface between the PV array and the utility grid. The control performance of the inverter is an important element that affects the current

quality injected into the grid. It also affects the DG operation, performance, and harmonic interactions with the grid [85].

5.4 Background of DG Primary Controller

Grid-side converters possess a control structure that is formed of two cascaded loops: a current loop that regulates the grid current and solves power quality problems, and a dc-link voltage controller that is responsible for maintaining the stability of the system. Control strategies can be divided into different groups based on the reference frame that they utilize. In this section, synchronous reference frame control and stationary reference frame control are discussed.

5.4.1 Synchronous reference frame control

In synchronous reference frame control, also known as *dq* control, a reference frame transformation module is used to change the grid voltage and current waveforms into a reference frame that rotates synchronously with the grid voltage. Since this reference frame results in DC control variable values, filtering, and controlling become easier to implement. Proportional-integral (PI) controllers are usually used in this control structure due to their satisfactory behavior during DC variable regulation.

The matrix transfer function of the controller is given in *dq* coordinates as in (5.6):

$$G_{PI}^{(dq)}(s) = \begin{bmatrix} K_p + \dfrac{K_i}{s} & 0 \\ 0 & K_p + \dfrac{K_i}{s} \end{bmatrix} \tag{5.6}$$

Where K_p and K_i are the proportional gain and the integral gain of the controller, respectively. Cross-coupling terms are usually implemented to compensate the couplings due to the output filter. Cross-couplings and voltage feedforward are normally used to enhance the PI controller performance. PI controllers do not offer an efficient harmonic compensation method of low-order harmonics, which represents the main disadvantage in grid-connected system applications. The PI controller is not able to suppress the steady-state error when controlling sinusoidal waveforms. Thus, other types of controllers should be used for sinusoidal control variables.

5.4.2 Stationary reference frame control

Stationary reference frame represents another control strategy frame in which the grid currents are changed into stationary reference frame using an $abc \rightarrow \alpha\beta$ module. With the presence of sinusoidal controlled variables, the PI controller cannot be implemented. Proportional Resonant (PR) Controllers have gained popularity in the last decade due to their ability to effectively control grid-currents in DG systems. They function accurately through their ability to track converter reference sinusoidal currents in this frame without steady-state magnitude and phase error. This is a result of their capacity for attaining a very high gain around the resonance frequency.

The matrix transfer function of the controller is given in the stationary reference frame as in (5.7):

$$
G_{PR}^{(\alpha\beta)}(s) = \begin{bmatrix} K_p + \dfrac{K_i s}{s^2 + w^2} & 0 \\ 0 & K_p + \dfrac{K_i s}{s^2 + w^2} \end{bmatrix} \tag{5.7}
$$

where ω is the resonance frequency of the controller.

The quality of the distributed power in grid-tied systems is crucial and is the subject of many standards. The current THD injected in the grid must not exceed the value of 5% according to the standards. A current controller can be implemented to compensate the grid harmonics and enhance the power quality. A PR controller can be used to achieve harmonic compensation. Several generalized integrators can be cascaded and tuned to resonate at the desired frequency value. As a result, harmonic compensation at different frequencies is produced. When using a PI controller, each harmonic order requires harmonic compensators for the positive and negative sequences under unbalanced conditions. This increases the complexity of the control algorithm. In contrast to PI controllers, the harmonic compensator of a PR controller operates on both sequences of the selected harmonic order.

The transfer function of a harmonic compensator designed to compensate the third, fifth and, seventh harmonic orders is given as in (5.8):

$$
G_h(s) = \sum_{h=3,5,7} K_{ih} \frac{s}{s^2 + (\omega \cdot h)^2} \tag{5.8}
$$

The PR controller is a good candidate in applications where high dynamic and harmonic compensation is required such as low-order harmonics in distributed generation power systems. This is a result of the ability of the harmonic compensator to strictly react to the frequencies that are very close to the resonance frequency; conserving the dynamics of the PR controller [86].

5.5 Harmonic Compensation Using PV-Based DGs

The increased non-linear loads draw concerns for today's power system grid and for utilities. Passive or active filters are integrated to reduce the harmonic distortions injected by non-linear loads such as EV battery charging. Since many DGs such as PV, wind, and fuel cells are equipped with DG-grid interfacing converters, they can be integrated in residential areas to enhance power quality and compensate the harmonics. An increased load in renewable energy-based distributed generation units are integrated in the power distribution system, causing the power industry to undergo a shift. The installation of rooftop PV systems in residential regions has risen. PV arrays are connected via DG-grid interfacing inverters to the grid. The DG-grid interfacing inverters convert the voltage level from the energy source to a voltage level that can be connected to the grid. They are also used to transport real power to the grid. DG-grid interfacing converters can provide system harmonic compensation [87]. Among the renewable energy sources, PV has drawn a lot of attention since it is safe, clean, has no fuel cost, produces no noise or air pollution, and has negligible running and maintenance cost [84].

The increased nonlinear loads draw power quality concerns in the residential distribution grid. Compensating the harmonics due to nonlinear loads could be complicated since these loads have a scattered nature in the grid. The increased implementation of roof-top PV inverters in residential grids can be utilized to address the power quality issues. These systems can be implemented to compensate for the harmonics of the grid. The increase of nonlinear loads in the grid leads to increased harmonic currents and harmonic voltages in the grid. Creating a technique to compensate the harmonics produced by these scattered nonlinear loads in the residential distribution grid is important. Harmonic compensation can be achieved by designing and implementing passive filters. The adoption of passive filters to mitigate the harmonics produced by nonlinear loads has been widely used in literature. However, the performance of these systems is affected by the system impedance.

Active filters, including series and parallel structures, constitute another harmonic compensation tool that is more flexible than the passive filters. However, they must be implemented in proximity with nonlinear loads to measure their current. This presents a challenge since the nonlinear loads are spread across the distribution network, and thus, this compensation tool becomes very expensive and complicated. Resistive active power filters can be employed to reduce the harmonics of the grid voltage through sensing the grid voltage. However, a resistive active power filter should be dispersed overall in the feeder due to the relationship between the electrical length of the feeder and the wavelength of any frequency element [88].

5.5.1 Genetic algorithm applications in power engineering

In this proposed research, PV-based DGs are connected at certain buses of an IEEE network to compensate harmonic currents produced by EV battery charging. The harmonic spectrums of the DGs are optimally determined using the GA to reduce the voltage THD and minimize the current THD at the main substation. Genetic algorithms are a common nonlinear optimization approach used in many applications for power engineering. Conventional optimization approaches normally start with initial points and perform mathematical operations in each iteration until a local optimal solution is obtained. In a genetic algorithm, a population of randomly generated individuals is evolved to reach the fittest solutions. A genetic algorithm is an optimization tool applied to solve problems in harmonic passive filter planning in radial distribution systems and to minimize the voltage THD. Factors such as filter location, sizing, and power loss minimization are optimally considered in passive harmonic filter design for electric distribution systems in [89], [90]. A genetic algorithm can solve optimization problems that standard optimization algorithms cannot address with the objective function being discontinuous, nondifferentiable, stochastic, or highly non-linear. In this research, the objective functions — voltage THD and current THD — are highly non-linear. After the randomly created initial population, the GA produces a set of new populations using the individuals in the current generation at each step. The population evolves after successive generations, reaching an optimal solution [91]. A description of the GA approach is presented in Fig. 5.2.

In literature, renewable resources have been integrated into distribution systems to reduce the impacts of EVs on harmonic distortion. Wind generators constitute a source of

harmonic currents which have harmonic profiles in common with EVs and thus can be utilized to reduce the impacts on harmonic distortions. In [92], a harmonic decoupled power flow model is implemented, including EV loads and wind generators to evaluate the impacts of EVs on harmonic distortions. A genetic algorithm is then developed to determine the optimal sizing of wind generators to reduce the voltage and current THDs. The study concludes that the integration of wind generators into the power system aids in lowering the voltage and total current harmonic distortions produced by EVs. In [93], the optimal distributed generator placement and sizing are determined to reduce real power losses and total harmonic distortion for voltage by using a combination of a Hybrid Genetic Algorithm and Particle Swarm Optimization search. The results show the efficiency of the proposed technique to minimize the losses and THD for voltage.
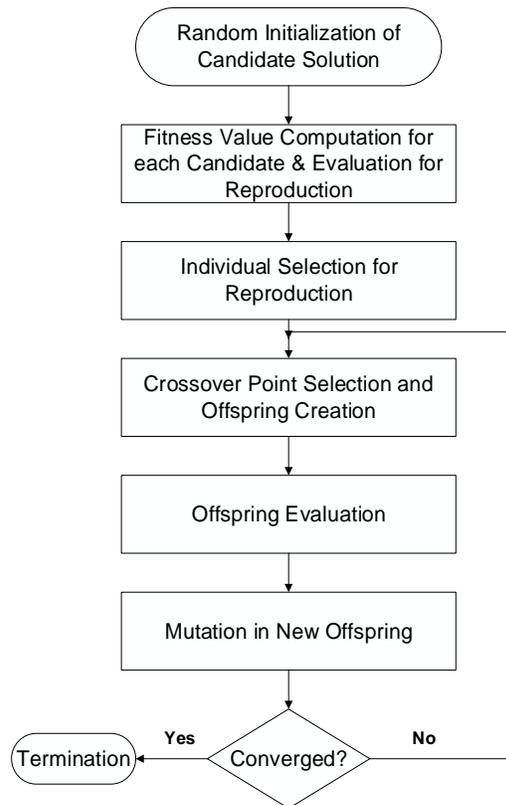
Fig. 5.2. Genetic algorithm flowchart.

Three PV-based DGs are connected to the 33-bus radial system at buses #14, 20, and 25. These locations are chosen to distribute the PVs among the feeders (one PV per feeder) and place them close to the EV loads. Figure 5.3 shows the distribution system under study with EV loads and PV-based DGs integrated.
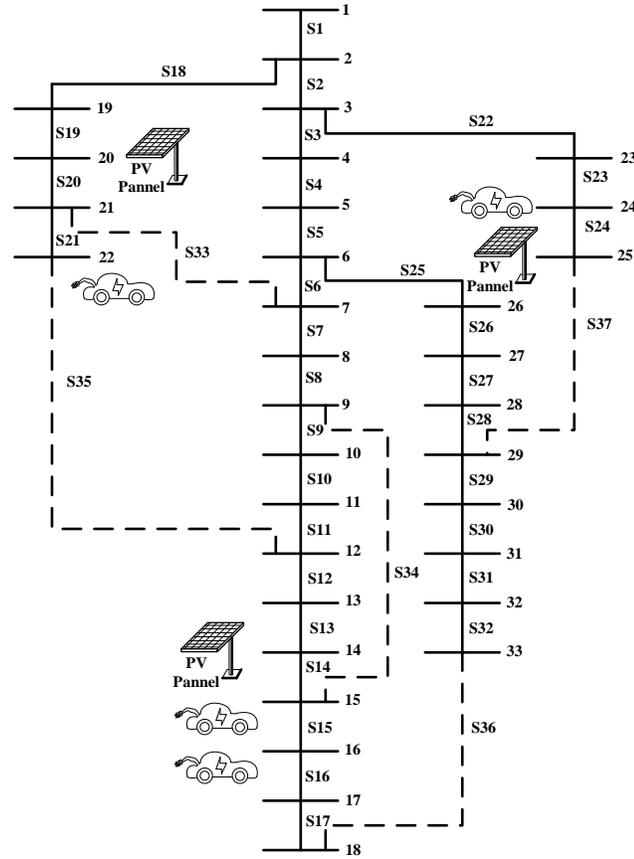
Fig. 5.3. The IEEE 33-bus radial distribution system with EV parking lots and PV-based DGs.

The PV penetration level is kept at 15% with a power rating of 655.5 kVA to match the EV penetration level. Since there are three PV-based DGs connected at each bus, the power generated by each PV source is equal to 218.47 kVA. The additional power ratings are added to buses #14, 20, and 25. The power ratings become 338.47 kW, 308.47 kW, and 638.47 kW at buses #14, 20, and 25, respectively.

The conventional power flow is computed this time, including PV-based DGs. The parameters are then obtained from the power flow solution at the fundamental frequency, including real and reactive power demands at certain buses. Bus voltage magnitudes, resistances, and reactances are declared as global variables. Since PV-based DGs are modeled by harmonic current sources, the load admittance value at buses #14, 20, and 22 are taken as zero. The admittance of each branch is computed, and the bus admittance matrix is obtained. The fundamental current generated by each PV-based DG is calculated using (5.9).

$$I_{PV,i}^1 = \left[\frac{P_{PV,i}^{inv} + jQ_{PV,i}^{inv}}{\left| v_i^1 \right|} \right]^* \tag{5.9}$$

The same harmonic spectrum for a Level III charger is used, and the hth harmonic order current is equivalent to the one previously obtained. The harmonic spectrum of each PV-based DG is presented in terms of x as follows:

$$\left(\frac{I_h}{I_1} \right)_{PV_1} = \left[1, 0, x(1), 0, x(2), 0, x(3), 0, x(4) \right]$$

$$\left(\frac{I_h}{I_1} \right)_{PV_2} = \left[1, 0, x(5), 0, x(6), 0, x(7), 0, x(8) \right] \tag{5.10}$$

$$\left(\frac{I_h}{I_1} \right)_{PV_3} = \left[1, 0, x(9), 0, x(10), 0, x(11), 0, x(12) \right]$$

where x(1), x(5), and x(9) correspond to the third harmonic; x(2), x(6), and x(10) correspond to the fifth harmonic; x(3), x(7), and x(11) correspond to the seventh harmonic, and x(4), x(8), and x(12) correspond to the ninth harmonic of the PV-based DGs.

The hth harmonic order current at each bus where a PV-based DG is connected is given as follows [52]:

$$I_{PV_1,i}^h = \left(\frac{I_h}{I_1} \right)_{PV_1} I_{PV,i}^1$$

$$I_{PV_2,i}^h = \left(\frac{I_h}{I_1} \right)_{PV_2} I_{PV,i}^1 \tag{5.11}$$

$$I_{PV_3,i}^h = \left(\frac{I_h}{I_1} \right)_{PV_3} I_{PV,i}^1$$

Next, (4.5) is used to calculate the bus harmonic voltages at each harmonic order. Total harmonic distortion for voltage and current are also calculated.

5.5.2 Voltage total harmonic distortion minimization

A. Objective function

A single objective optimization technique, formulated as a constrained non-linear integer optimization problem, is presented to reduce disturbances on the distribution system in the presence of EVs. The main objective is to reduce the total harmonic distortion of voltage

at the bus, where the maximum disturbance occurs. An objective function $F_{THDv}{}^{max}$ is formulated to minimize the total harmonic distortion voltage in the system.

The objective function is given as follows:

$$F_{THD_v^{\max}} = \min(THD_v^{\max}) \tag{5.12}$$

where

$$THD_v^{\max}(\%) = \frac{\sqrt{\sum_{h=2}^{h_{\max}} \left|v_{\max}^h\right|^2}}{\left|v_{\max}^1\right|} \times 100,$$

$THD_v{}^{max}$ is the voltage THD at the bus that experiences the highest disturbance, i.e. bus #16, $v_{max}{}^h$ is the harmonic voltage magnitude at the hth harmonic order at the same bus number, and $v_{max}{}^1$ is the voltage magnitude at the same bus number at the fundamental frequency.

B.   Equality constraints

The real and reactive power balance constraints at the fundamental frequency for each system bus i are given as follows:

$$
\begin{aligned}
&P_{G,i} + P_{PV,i}^{inv} - P_{D,i} \\
&= \sum_{j=1}^{N_{bus}} \left|v_i^1\right|\left|v_j^1\right|\left|\gamma_{i,j}^1\right|\cos\left(\theta_{i,j}^1 - \delta_i^1 + \delta_j^1\right)
\end{aligned}
\tag{5.13}
$$

$$
\begin{aligned}
&Q_{G,i} + Q_{PV,i}^{inv} - Q_{D,i} \\
&= \sum_{j=1}^{N_{bus}} \left|v_i^1\right|\left|v_j^1\right|\left|\gamma_{i,j}^1\right|\sin\left(\theta_{i,j}^1 - \delta_i^1 + \delta_j^1\right)
\end{aligned}
\tag{5.14}
$$

where $P_{G,i}$ is the fundamental real power generation at bus i; $Q_{G,i}$ is the fundamental reactive power generation at bus i; $\gamma_{i,j}{}^1$ is the magnitude of $(i, j)^{th}$ element of the fundamental bus admittance matrix; $\theta_{i,j}{}^1$ is the angle of $(i, j)^{th}$ element of the fundamental bus admittance matrix; and $\delta_i{}^1$ is the fundamental voltage angle at bus i.

The harmonic power flow constraint is given as follows [52]:

$$Y^h V^h = I^h \tag{5.15}$$

C.   Inequality constraints

C.1. Bus voltage limits

The rms voltage magnitude at every bus i is bound by a given lower limit and a given upper limit as shown:

$$v_{\min} \le \sqrt{\left|v_i^1\right|^2 + \sum_{h=2}^{h_{\max}} \left|v_i^h\right|^2} \le v_{\max} \tag{5.16}$$

where v_{min} is the lower rms voltage limit and v_{max} is the upper rms voltage limit with $v_{\min} = 0.9$ p.u. and $v_{\max} = 1.1$ p.u [94] .

C.2. Total harmonic distortion limits

The voltage THD value at each bus i is limited by IEEE-519 standards as follows:

$$THD_{v,i}(\%) = \frac{\sqrt{\sum_{h=2}^{h_{\max}} \left|v_i^h\right|^2}}{\left|v_i^1\right|} \times 100 \le THD_v^{\lim it} \tag{5.17}$$

where $THD_v^{\max}$ is the maximum permissible total voltage harmonic distortion set in IEEE-519 standards. It is set at 5% [72].

C.3. Individual harmonic distortion limits

Individual voltage harmonic distortion value at every bus i is limited by IEEE-519 standard as follows:

$$IHD_{v,i}^h(\%) = \frac{\left|v_i^h\right|}{\left|v_i^1\right|} \times 100 \le IHD_v^{\lim it,h} \tag{5.18}$$

where $IHD_v^{limit,h}$ is the maximum allowable voltage harmonic distortion level at harmonic order h. It is specified as 3% [72].

Individual current harmonic distortion at each bus i is limited by IEEE-519 standards as follows:

$$IHD_{i,i}^h(\%) = \frac{\left|I_i^h\right|}{\left|I_i^1\right|} \times 100 \le IHD_i^{\lim it,h} \tag{5.20}$$

where $LB_i < IHD_i^{\lim it,h} < UB_i$, $LB_i = -10\%$ and $UB_i = 10\%$, and $IHD_I^{limit,h}$ is the maximum allowable current harmonic distortion level at harmonic order h [52], [72].

C.4. Current limit constraint

The current flowing through each branch is calculated using (4.6) at the fundamental frequency (where $h = 1$). It is assumed that the current limit is equal to twice the branch current during the rated load, i.e.,

$$I_{ij}^{\lim it} = 2 \times I_{ij} \tag{5.21}$$

Therefore, the current limit constraint is given by

$$I_{ij} < I_{ij}^{\lim it} \tag{5.22}$$

This current constraint is added to the objective function as a penalty factor:

$$F_{obj}^{new} = F_{THD_v^{max}} + P_f \tag{5.23}$$

where $P_f = 0$ when there is no violation, and $P_f = 1e^8$ when a violation occurs.

A function handle is passed to the fitness function as the first argument to the GA function to minimize it. In the second argument, the number of variables is specified as 12, since there are 12 unknown variables associated with the PV harmonic currents.

The GA algorithm returns the values of the unknown control variables resulting in minimizing the THD for voltage. These values determine the harmonic spectrum of each PV-based DG, as shown in Fig. 5.4.
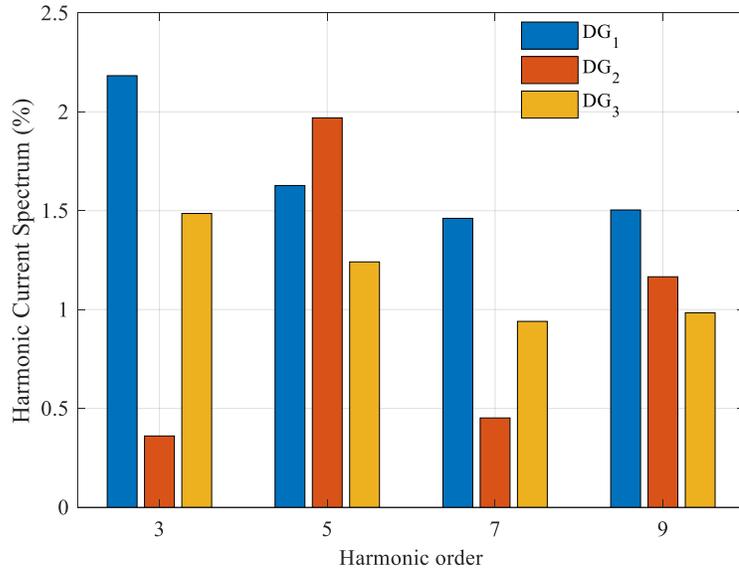
Fig. 5.4. Harmonic current spectrum of each PV-based DGs.

The harmonic spectrum associated with each PV, along with the presence of EVs results in the THD voltage profile at bus #16 presented in Fig. 5.5.
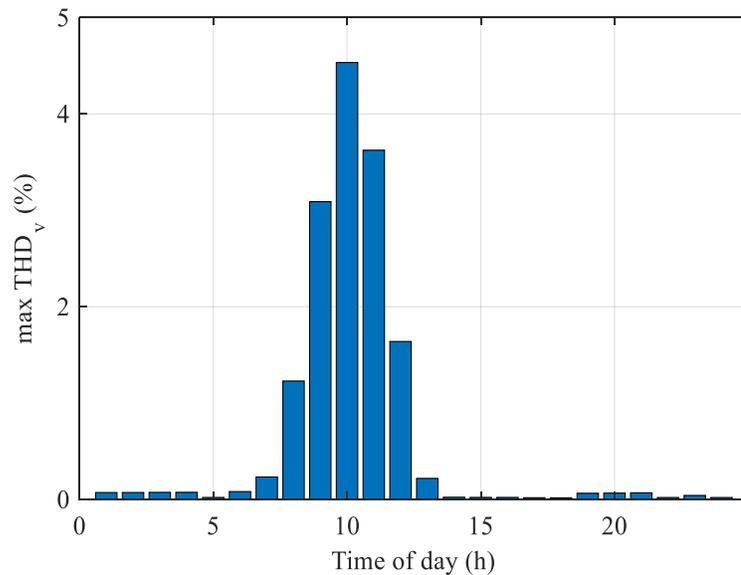
Fig. 5.5. THD for voltage after PV compensation.

The voltage disturbance values are lower after integrating PV-based DGs. The highest value of THD reaches 4.5% at 10 a.m. This value remains below the 5% allowable limit set by the standards. At this specific time, the GA algorithm results in a reduction of THD by a factor of 2.89. THD values are also reduced from 8.9% to 3.1% at 9 a.m. and from 10.4% to 3.6% at 11 a.m. as a result of the integration of PV-based DGs into the system.

Using the harmonic spectrum of PV-based DGs, the voltage THD along with the harmonic distribution of EV loads and conventional loads is minimized. Next, the harmonic current through the substation transformer is obtained using (4.6). The harmonic spectrum through the substation transformer resulting from both EV and PV loads at the maximum loading conditions is shown in Fig. 5.6.

Using the harmonic spectrum shown in Fig. 5.6, the distribution transformer lifetime is obtained and presented in Fig. 5.7. The transformer lifetime is constant at 20.55 years at all loading conditions resulting from the integration of PV-based DGs.
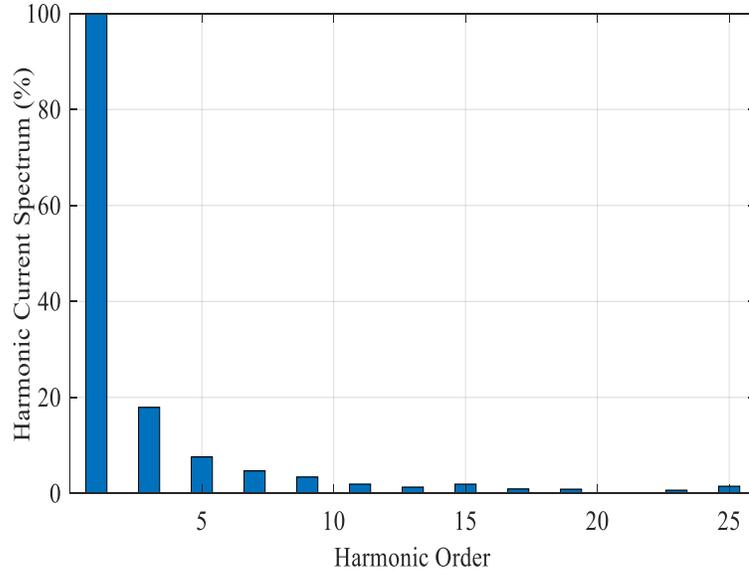
Fig. 5.6. Harmonic current spectrum through substation transformer after PV compensation.
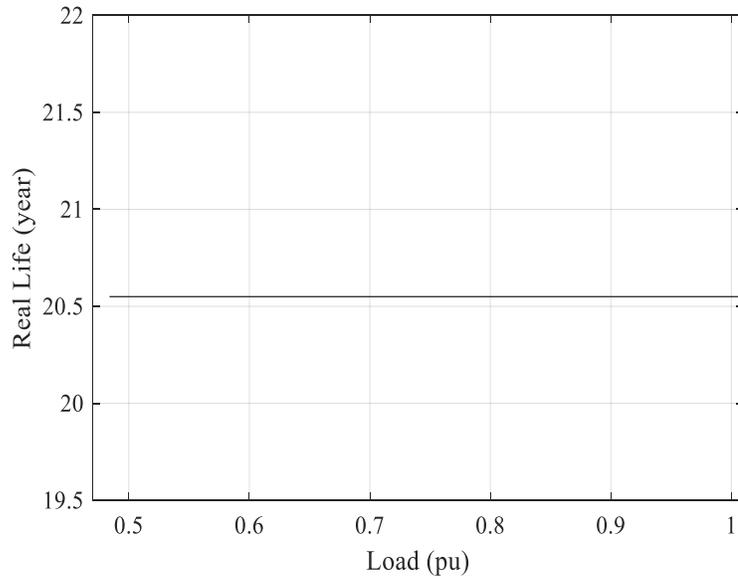
Fig. 5.7. Transformer real life after PV compensation.

5.5.3 Current total harmonic distortion minimization

A.   Objective function

A second single objective optimization technique, formulated as a constrained non-linear integer optimization problem, is presented to minimize the total harmonic distortion for current through the main substation transformer. An objective function F_{THDI}^{sub} is formulated to achieve this goal and given by

$$F_{THD_I^{sub}} = \min(THD_I^{(1,2)}) \tag{5.24}$$

where
$$THD_I^{(1,2)}(\%) = \frac{\sqrt{\sum_{h=2}^{h_{max}} \left| i_{(1,2)}^h \right|^2}}{\left| i_{(1,2)}^1 \right|} \times 100 \ ,$$

in which, $THD_I^{(1,2)}$ is the current THD through the substation transformer, connecting buses 1 and 2, $i_{(1,2)}^h$ is the harmonic current at the hth harmonic order through the substation transformer, and $i_{(1,2)}^1$ is the current through the substation transformer at the fundamental frequency.

B.   Equality constraints

The real and reactive power balance constraints at the fundamental frequency for each bus i are given as in (5.13) and (5.14).

The harmonic power flow constraint is given in (5.15).

C.   Inequality constraints

C.1. Total harmonic distortion limits

The rms voltage magnitude at every bus i is bound by lower and upper limits as given in (5.16).

C.2. Total harmonic distortion limits

The current THD value at each bus i, THD_i, is limited by the IEEE-519 standards as follows:

$$THD_i(\%) = \frac{\sqrt{\sum_{h=2}^{h_{max}} \left| i_i^h \right|^2}}{\left| i_i^1 \right|} \times 100 \leq TDD_i^{\lim it} \tag{5.25}$$

where TDD_i^{limit} is the maximum permissible total current demand distortion, and is set at 12%.

C.3. Individual harmonic distortion limits

Individual current harmonic distortion value at every bus i is limited by IEEE-519 standard as follows:

$$IHD_{i,i}^h(\%) = \frac{\left| i_i^h \right|}{\left| i_i^1 \right|} \times 100 \leq IHD_i^{\max,h} \tag{5.26}$$

where IHD$_i^{max,h}$ is the maximum allowable current harmonic distortion at the harmonic order h, and bounded by $LB_i \leq IHD_i^{max,h} \leq UB_i$, $LB_i = -20\%$, and $UB_i = 20\%$. The lower and upper bounds, LB_i and UB_i, are relaxed in this problem to enhance the minimization the current THD.

C.4. Current limit constraint

The current constraint is expressed as in (5.22) and added to the objective function as a penalty factor.

The harmonic spectrum used for EV loads is combined with conventional loads here. The equation for the harmonic currents through the main substation is used. The GA algorithm applied returns the values of the unknown control variables resulting in a minimized THD for current. The harmonic spectrum of each PV-based DG unit is presented in Fig. 5.8.
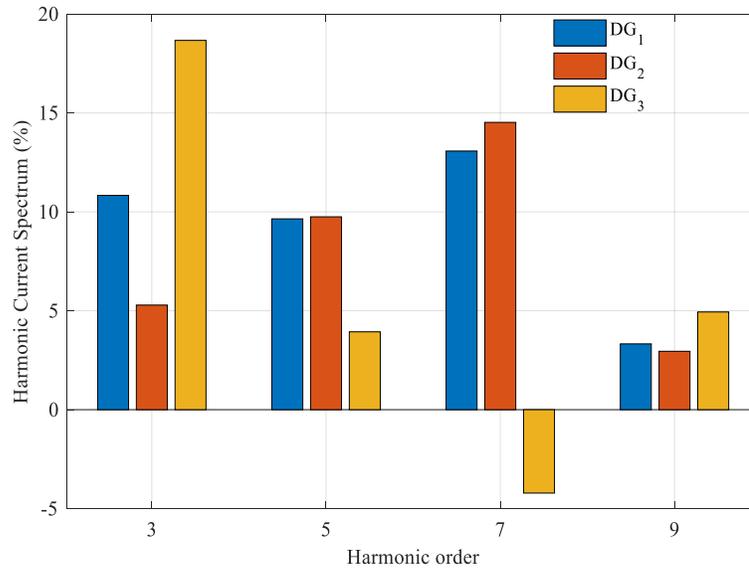
Fig. 5.8. Harmonic current spectrum of each PV-based DG.

After integrating the PV-based DGs with the presence of EV loads, the THD for current is measured throughout a 24 hr cycle, as shown in Fig. 5.9. The maximum current disturbance takes place at 10 a.m. with a value of 11.6 %. This value is below the maximum current THD set in IEEE standards. The current THD decreases to 7.96% at 11 a.m. and falls to 1.4% at noon. After obtaining the harmonic spectrum of PV-based DGs that minimize the current THD, the harmonic current through the substation transformer is calculated using (4.6).

The harmonic spectrum through the substation transformer resulting from both EV and PV loads at the maximum loading conditions is obtained and shown in Fig. 5.10.
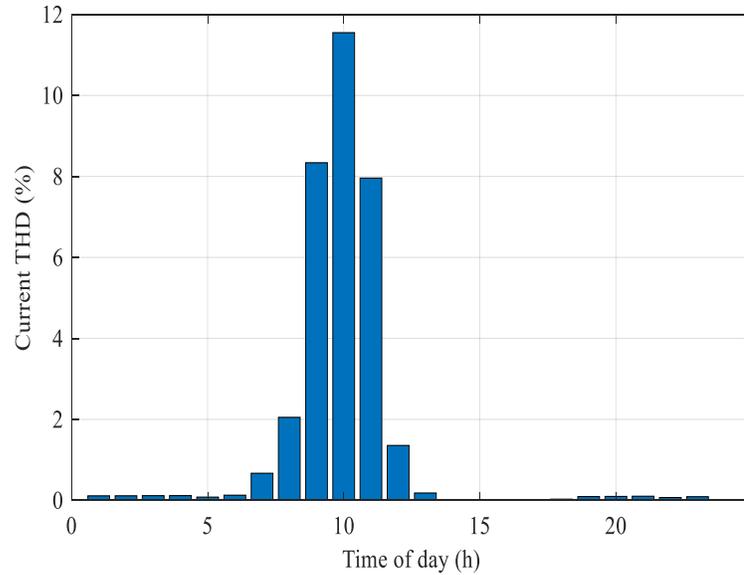
Fig. 5.9. THD for current after PV compensation.

After obtaining the harmonic spectrum of PV-based DGs that minimize the current THD, the harmonic current spectrum through the substation transformer is calculated using (4.6). This spectrum was used to calculate the transformer lifetime. The results are shown in Fig. 5.11. The transformer lifetime remains constant at 20.55 years at all loading conditions. These results confirm the effectiveness of the proposed optimal harmonic power flow in compensating the EV impacts on DTs.
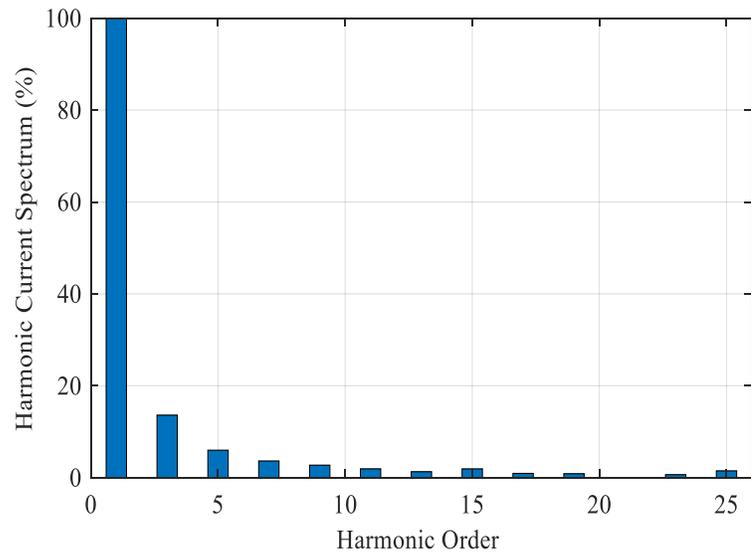
Fig. 5.10. Harmonic current spectrum through substation transformer after PV compensation.
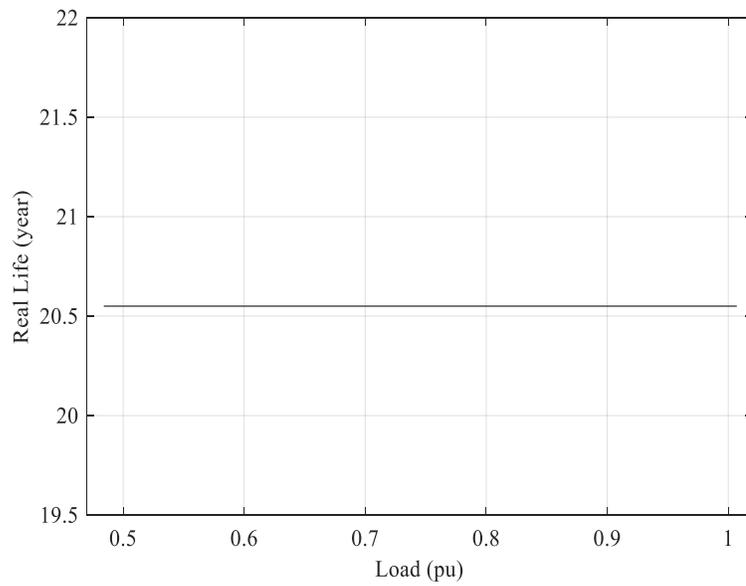
Fig. 5.11. Transformer real life after PV compensation.

CHAPTER 6

CONCLUSIONS AND FUTURE WORK

6.1 Conclusions

This study consists of a comprehensive evaluation of the impacts of electric vehicle battery charging on the power system and its components. The first phase of the evaluation is performed at the device level of the power system: the distribution transformer. A per-unit model of the transformer losses, temperature rise, and lifetime is proposed to show the effects of current harmonics produced as a result of EV battery charging. The assessment is investigated on a sample 1,500 kVA DT under 20% EV penetration with the harmonic distribution of conventional and EV loads used. These results are compared with the ones obtained in the absence of EV loads.

The results show that the extra EV load demand causes a rise in load losses of the transformer. As a result, the transformer temperature rise increases, and lifetime degrades. The highest load losses, temperature rise, and lifetime degradation occur at 9:30 p.m. when EV load is at its maximum. The load loss rises from 3.65 p.u. to 5.68 p.u. after introducing EV loads into the grid. This rise in load loss is caused by an increase in eddy-current and other stray losses. The hottest-spot conductor rise over ambient increases from 88.5 °C to 124.1 °C. This is caused by the rise in top-oil over ambient temperature and hottest-spot conductor over top-oil temperature due to transformer losses. In the absence of EV loads, the hottest-spot temperature always remains below 110 °C. Consequently, the aging acceleration factor is always below one, indicating that the accelerating rate of the transformer insulation aging is normal. However, with the introduction of EVs, this aging acceleration factor exceeds one between 9:30 p.m. and 11:00 p.m., which indicates that the transformer is not operating in safe conditions. This factor increases from 0.097 p.u. to 4.006 p.u. as a result of EV charging. Other indices are calculated to analyze the lifetime of the transformer. With temperature values below the reference temperature of 110 °C in the case of 0% EV penetration, the transformer p.u. insulation life is higher or equal to one, implying that the insulation life is not degraded. Insulation aging caused by EV charging is observed from 9:30 p.m. to 11:00 p.m., falling to 0.25 p.u. at 9:30 p.m. The percent loss of life value in the absence of EVs is less than the normal LOL value of 0.0133%. This value rises to 0.05341% at 9:30 p.m. due to EV charging. After obtaining the aging

acceleration factor, the real life of the transformer is modeled and quantified. It is observed that it decreases from 20.55 years to approximately 5.13 years at 9:30 p.m.

A study is conducted involving current harmonic spectrums of different charging levels to understand the impacts associated with the users' charger choice. Since the state of charge has an impact on the harmonic currents, current harmonic measurement data is recorded at various time intervals throughout the charging cycle. Weighted arithmetic mean is applied on the time-variant harmonic magnitudes to obtain the harmonic magnitudes of the spectrum. Including the effect of the state of charge on the total harmonic distortion of charging current improves the accuracy of the assessment. Two harmonic spectrums — one of a Level I/II charger and the other of a Level III charger — are used to model and quantify the effects of harmonic components on the distribution transformer. Based on the results, it is concluded that the load losses, temperature rise, and lifetime reduction with a Level III charger are greater than the impacts caused by a Level I/II charger. Thus, a Level III charger current harmonics affect the transformer more severely than the harmonics of a Level I/II charger.

The assessment is extended to the system level, where case studies are performed on a practical 33-bus radial system consisting of a combination of residential, commercial, and industrial loads. Four EV parking lots are supplied from certain buses of the system. DHPF technique is applied to measure the system distortion resulting from EV charging with a penetration level of 15%. This algorithm returns the bus voltage profile at each harmonic order. The harmonic voltage values are used to calculate the voltage THD when using a Level III charger. Since the highest voltage THD occurs at bus #16 at which an EV parking lot is supplied, the voltage THD is obtained for 24 hours. During the period from 9 a.m. till 11 a.m., the voltage THD values are beyond the limit of 5% set by IEEE 519 standards. This is a result of the EV charging load being high during this time period. The voltage THD reaches 13.0% at 10 a.m. and is at its highest. The THD limit is violated at each bus where an EV charging lot is connected from 9 a.m. till 11 a.m. It is also observed that the buses located at proximity with the EV charging lots also undergo high voltage disturbance. The harmonic currents through the substation are estimated to measure the current disturbance on the substation transformer due to EV charging and other conventional load

producing harmonics. It is noted that the highest value of the harmonic disturbance occurs at 10 a.m., when the EV load is at its peak. Then, the disturbance is measured at maximum loading conditions to display the voltage THD at each bus. It is observed from the voltage THD profile that the highest value happens at bus #16, followed by bus #15, and finally, 24 where EV loads are connected. Bus #14 experiences the third most voltage disturbance since its location is close to two parking lots connected to the same feeder. The same analysis is repeated for a Level I/II charger. Similarly to the Level III charger, the highest voltage disturbance during maximum loading conditions takes place at bus #16. However, only buses #15, 16, and 24 experience a disturbance higher than the 5% limit at certain times. Based on the voltage THD values, it is concluded that Level I/II chargers have a less severe effect on the system than Level III chargers do. This is a result of the smaller harmonic current values in Level I/II chargers compared to Level III chargers. The algorithm is used to obtain a 24 hr THD profile. At the maximum EV loading of 0.95 p.u., the voltage THD is 7.1% at 10 a.m. at bus #16. The voltage limit of 5% is only violated at 10 a.m. and 11 a.m. in this case at buses #16, 14, 15, and 24. Bus #22 voltage THD does not violate the limit of 5% with a Level I/II charger. The remainder of the buses remains below this limit. The current THD through the substation has lower values with a Level I/II charger than with a Level III charger.

Next, a harmonic compensation technique that involves the integration of PV-based DGs into the system is proposed. DGs can provide an ultimate solution to solve many issues associated with the power system since they are smaller electrical power generation units that are readily available, easy to install, relocate, operate, and are affordable. The benefits associated with the presence of DGs, have led to their increase in popularity in distribution networks. A positive impact of DGs on power systems is that they enhance the overall system performance by improving voltage profiles and power quality [93]. An optimization problem is formulated to find the harmonic current ratio of each PV-based DG connected at a certain bus of the network. The total harmonic distortion for voltage at the bus where the maximum distortion occurs and the current THD through the main substation are taken as the objectives that should be minimized. The GA algorithm returns the harmonic spectrums of PVs that result in the minimum voltage THD at bus #16 for a Level III charger. The maximum voltage THD value occurs at 10 a.m. and reaches 4.5% which does

not violate the limit set by the standards. The values at the other times are also reduced by PV integration.

The second objective of minimizing current THD through the main transformer is addressed. The harmonic spectrums of conventional loads and EV loads are combined in the DHPF algorithm. The GA is performed and returns the harmonic spectrum of each PV-based DG that leads to minimum current disturbance.

6.2 Future Works

This research can be further extended to enhance the performance of power systems and their components. The two objective functions proposed in chapter 5 can be combined into a single fitness function in order to minimize the voltage THD and the current THD simultaneously. This would help determine an optimal single harmonic spectrum for each PV-based DG. Since distribution transformers constitute important components of the electric power system that connect the primary system to the secondary system, extending their life expectancy is beneficial to maintain the reliability of power distribution. The optimization problem of the proposed GA algorithm can be extended to minimize the loss of life of distribution transformers. In addition, the optimal placement of DGs is a factor that should be addressed to maximize the benefits of DG integration in the network. Non-optimal placement and sizing of DGs can lead to a rise in system power losses and costs. Appropriate size and location of DGs can enhance the results of achieving minimum voltage and current disturbance [93]. In addition to the integration of PVs, active harmonic filters can be designed and implemented to lower harmonics produced by non-linear devices and provide highly dynamic reactive power that meets the requirements. Parallel connected active harmonic filters offer many advantages resulting from their simplicity to retrofit and scale, and their direct effectiveness in mitigating the harmonic voltage. The available active filters can filter harmonics up to the 50th order and offer dynamic reactive power compensation [95].

REFERENCES/BIBLIOGRAPHY

[1]   "Climate Change Action Plan." [Online]. Available: https://www.ontario.ca/page/climate-change-action-plan. [Accessed: 14-Sep-2016].

[2]   T. H. E. Energy, "Stuck in Neutral 9+17," no. December, 2017.

[3]   N. Tanaka, "Technology Roadmap: Electric and plug-in hybrid electric vehicles," *Int. Energy Agency*, no. June, p. 52, 2011.

[4]   M. Kazerooni and N. C. Kar, "Impact analysis of EV battery charging on the power system distribution transformers," *2012 IEEE Int. Electr. Veh. Conf. IEVC 2012*, pp. 1–6, 2012.

[5]   M. S. Taci, M. H. Sarul, and G. Yildirmaz, "The effects of the harmonic components upon transformer active losses in case of (non)sinusoidal sources and (non)linear loads," in *Proceedings of IEEE International Conference on Industrial Technology 2000 (IEEE Cat. No.00TH8482)*, 2000, vol. 1.

[6]   A. Chidurala, T. K. Saha, N. Mithulananthan, and R. C. Bansal, "Harmonic emissions in grid connected PV systems: A case study on a large scale rooftop PV site," *IEEE Power Energy Soc. Gen. Meet.*, vol. 2014-Octob, no. October, pp. 1–5, 2014.

[7]   R. Bass and N. Zimmerman, "Impacts of Electric Vehicle Charging on Electric Power Distribution Systems," 2013.

[8]   M. Shaaban, "Accommodating a High Penetration of Plug-in Electric Vehicles in Distribution Networks," p. 166, 2014.

[9]   B. Frieske, M. Kloetzke, and F. Mauser, "Trends in vehicle concept and key technology development for hybrid and battery electric vehicles," *World Electr. Veh. J.*, vol. 6, no. 1, pp. 9–20, 2013.

[10]   N. Carey and J. White, "Ford plans $11 billion investment, 40 electrified vehicles by 2022," 2018. [Online]. Available: https://www.reuters.com/article/us-autoshow-detroit-ford-motor/ford-plans-11-billion-investment-40-electrified-vehicles-by-2022-idUSKBN1F30YZ.

[11]   T. Alagarsamy and B. Moulik, "A Review on Optimal Design of Hybrid Electric Vehicles and Electric Vehicles," *2018 3rd Int. Conf. Converg. Technol. I2CT 2018*, pp. 1–5, 2018.

[12]   D. Wu, D. C. Aliprantis, and K. Gkritza, "Electric energy and power consumption by light-duty plug-in electric vehicles," *IEEE Trans. Power Syst.*, vol. 26, no. 2, pp. 738–746, 2011.

[13]   A. Kumar and L. B. Prasad, "Issues, challenges and future prospects of electric vehicles: A review," *2018 Int. Conf. Comput. Power Commun. Technol. GUCON 2018*, pp. 1060–1065, 2019.

[14] B. Sarlioglu, C. T. Morris, D. Han, and S. Li, "Driving Toward Accessibility: A Review of Technological Improvements for Electric Machines, Power Electronics, and Batteries for Electric and Hybrid Vehicles," *IEEE Ind. Appl. Mag.*, vol. 23, no. 1, pp. 14–25, 2017.

[15] A. Emadi, Y. J. Lee, and K. Rajashekara, "Power electronics and motor drives in electric, hybrid electric, and plug-in hybrid electric vehicles," *IEEE Trans. Ind. Electron.*, vol. 55, no. 6, pp. 2237–2245, 2008.

[16] L. Parsa and H. A. Toliyat, "Fault-tolerant interior-permanent-magnet machines for hybrid electric vehicle applications," *IEEE Trans. Veh. Technol.*, vol. 56, no. 4 I, pp. 1546–1552, 2007.

[17] C. C. Chan, "The state of the art of electric, hybrid, and fuel cell vehicles," *Proc. IEEE*, vol. 95, no. 4, pp. 704–718, 2007.

[18] Q. Li, W. Chen, Y. Li, S. Liu, and J. Huang, "Energy management strategy for fuel cell/battery/ultracapacitor hybrid vehicle based on fuzzy logic," *Int. J. Electr. Power Energy Syst.*, vol. 43, no. 1, pp. 514–525, 2012.

[19] M. Yilmaz and P. T. Krein, "Review of battery charger topologies, charging power levels, and infrastructure for plug-in electric and hybrid vehicles," *IEEE Trans. Power Electron.*, vol. 28, no. 5, pp. 2151–2169, 2013.

[20] S. Haghbin *et al.*, "Integrated chargers for EV's and PHEV's: Examples and new solutions," *19th Int. Conf. Electr. Mach. ICEM 2010*, 2010.

[21] T. Thiringer, M. Grenier, and M. G. H. Aghdam, "Design of on-board charger for plug-in hybrid electric vehicle," pp. 152–152, 2010.

[22] B. Singh *et al.*, "A Review of Three-Phase Improved Power Quality AC – DC Converters," *IEEE Trans. Ind. Electron.*, vol. 51, no. 3, pp. 641–660, 2004.

[23] M. A. Fasugba and P. T. Krein, "Gaining vehicle-to-grid benefits with unidirectional electric and plug-in hybrid vehicle chargers," *2011 IEEE Veh. Power Propuls. Conf. VPPC 2011*, pp. 1–6, 2011.

[24] X. Zhou, G. Wang, S. Lukic, S. Bhattacharya, and A. Huang, "Multi-function bi-directional battery charger for plug-in hybrid electric vehicle application," *2009 IEEE Energy Convers. Congr. Expo. ECCE 2009*, pp. 3930–3936, 2009.

[25] C. Botsford and O. Ev, "Fast Charging vs . Slow Charging : Pros and cons for the New Age of Electric Vehicles 20 Years of EV History 1989 to 2009," pp. 1–9, 2009.

[26] M. E. Initiative, "Electrification of the Transportation System," *MIT Energy Initiat.*, 2010.

[27] M. Etezadi-Amoli, K. Choma, and J. Stefani, "Rapid-charge electric-vehicle stations," in *IEEE Transactions on Power Delivery*, 2010, vol. 25, no. 3, pp. 1883–1887.

[28] D. C. Erb, O. C. Onar, and A. Khaligh, "Bi-directional charging topologies for plug-in hybrid electric vehicles," *Conf. Proc. - IEEE Appl. Power Electron. Conf. Expo. - APEC*, pp. 2066–2072, 2010.

[29] S. W. Hadley and A. A. Tsvetkova, "Potential Impacts of Plug-in Hybrid Electric Vehicles on Regional Power Generation," *Electr. J.*, vol. 22, no. 10, pp. 56–68, 2009.

[30] R. Liu, L. Dow, and E. Liu, "A survey of PEV impacts on electric utilities," *IEEE PES Innov. Smart Grid Technol. Conf. Eur. ISGT Eur.*, pp. 1–8, 2011.

[31] M. F. Shaaban, Y. M. Atwa, and E. F. El-Saadany, "PEVs modeling and impacts mitigation in distribution networks," *IEEE Trans. Power Syst.*, vol. 28, no. 2, pp. 1122–1131, 2013.

[32] M. Di Paolo, "Analysis of harmonic impact of electric vehicle charging on the electric power grid, based on smart grid regional demonstration project - Los angeles," *2017 IEEE Green Energy Smart Syst. Conf. IGESSC 2017*, vol. 2017-Novem, pp. 1–5, 2018.

[33] M. J. Rutherford and V. Yousefzadeh, "The impact of electric vehicle battery charging on distribution transformers," *Conf. Proc. - IEEE Appl. Power Electron. Conf. Expo. - APEC*, pp. 396–400, 2011.

[34] R. Godina, N. G. Paterakis, O. Erdinc, E. M. G. Rodrigues, and J. P. S. Catalao, "Electric vehicles home charging impact on a distribution transformer in a Portuguese Island," in *Proceedings - 2015 International Symposium on Smart Electric Distribution Systems and Technologies, EDST 2015*, 2015, pp. 74–79.

[35] Y. Assolami and W. G. Morsi, "Mitigating the impact of charging second generation plug-in battery electric vehicles on distribution transformer's insulation life using TOU prices," *2015 IEEE Electr. Power Energy Conf. Smarter Resilient Power Syst. EPEC 2015*, pp. 32–35, 2016.

[36] M. Agah and A. Abbasi, "The Impact of Charging Plug-In Hybrid Electric Vehicles on Residential Distribution Transformers," *2012 2nd Iran. Conf. Smart Grids*, pp. 1–5, 2012.

[37] M. Utakrue and K. Hongesombut, "Impact Analysis of Electric Vehicle Quick Charging to Power Transformer Life Time in Distribution System," *ITEC Asia-Pacific 2018 - 2018 IEEE Transp. Electrif. Conf. Expo, Asia-Pacific E-Mobility A Journey from Now Beyond*, pp. 1–5, 2018.

[38] J. C. Gómez and M. M. Morcos, "Impact of EV battery chargers on the power quality of distribution systems," *IEEE Trans. Power Deliv.*, vol. 18, no. 3, pp. 975–981, 2003.

[39] S. Argade, V. Aravinthan, and W. Jewell, "Probabilistic modeling of EV charging and its impact on distribution transformer loss of life," *2012 IEEE Int. Electr. Veh.*

Conf. IEVC 2012, pp. 1–8, 2012.

[40] D. Alame, M. Azzouz, and N. C. Kar, "Impact assessment of electric vehicle charging on distribution transformers including state-of-charge," *Midwest Symp. Circuits Syst.*, vol. 2018-Augus, no. 2, pp. 607–610, 2019.

[41] Z. Zhang, H. D. Chiang, and T. Wang, "Harmonic analysis of power system with wind generations and plug-in electric vehicles," *2013 IEEE Electr. Power Energy Conf. EPEC 2013*, pp. 1–6, 2013.

[42] R. C. Leou, C. L. Su, and C. N. Lu, "Stochastic analyses of electric vehicle charging impacts on distribution network," *IEEE Trans. Power Syst.*, vol. 29, no. 3, pp. 1055–1063, 2014.

[43] E. Voumvoulakis, E. Leonidaki, G. Papoutsis, and N. Hatziargyriou, "Evaluation of the impact of plug-in electric vehicles in Greek distribution network," *CIRED - Open Access Proc. J.*, vol. 2017, no. 1, pp. 2270–2274, 2017.

[44] N. Leemput, F. Geth, J. Van Roy, A. Delnooz, J. Buscher, and J. Driesen, "Impact of electric vehicle on-board single-phase charging strategies on a flemish residential grid," *IEEE Trans. Smart Grid*, vol. 5, no. 4, pp. 1815–1822, 2014.

[45] R. Scharrenberg, B. Vonk, and P. H. Nguyen, "EV stochastic modelling and its impacts on the Dutch distribution network," *2014 Int. Conf. Probabilistic Methods Appl. to Power Syst. PMAPS 2014 - Conf. Proc.*, pp. 1–6, 2014.

[46] A. Dubey and S. Santoso, "Electric Vehicle Charging on Residential Distribution Systems: Impacts and Mitigations," *IEEE Access*, vol. 3, pp. 1871–1893, 2015.

[47] M. R. A. Ashish Kumar Karmaker, Sujit Roy, "Analysis of the impacts of Electric Vehicle Charging Station in Bangladesh," *ECCE, IEEE Conf.*, pp. 7–9, 2019.

[48] S. Shafiee, M. Fotuhi-Firuzabad, and M. Rastegar, "Investigating the impacts of plug-in hybrid electric vehicles on power distribution systems," *IEEE Trans. Smart Grid*, vol. 4, no. 3, pp. 1351–1360, 2013.

[49] M. K. Gray and W. G. Morsi, "Power quality assessment in distribution systems embedded with plug-in hybrid and battery electric vehicles," *IEEE Trans. Power Syst.*, vol. 30, no. 2, pp. 663–671, 2015.

[50] E. F. Fuchs and M. A. S. Masoum, *Power Quality in Power Systems and Electrical Machines*. .

[51] A.Ulinuha, M. A. S. Masoum, and S. M. Islam, "Decoupled Harmonic Power Flow for Large Power System with Multiple Nonlinear Loads ," *Seventh Postgrad. Electr. Eng. Comput. Symp.*, 2006.

[52] V. Ravikumar Pandi, H. H. Zeineldin, and W. Xiao, "Determining optimal location and size of distributed generation resources considering harmonic and protection coordination limits," *IEEE Trans. Power Syst.*, vol. 28, no. 2, pp. 1245–1254, 2013.

[53] A. R. Abulawafa, A. Elagarably, and W. A. F. Mohamed, "Impacts of uncoordinated and coordinated integration of electric vehicles on distribution systems performance," *2017 19th Int. Middle-East Power Syst. Conf. MEPCON 2017 - Proc.*, vol. 2018-Febru, no. December, pp. 337–346, 2018.

[54] M. R. Sarker, D. J. Olsen, and M. A. Ortega-Vazquez, "Co-Optimization of Distribution Transformer Aging and Energy Arbitrage Using Electric Vehicles," *IEEE Trans. Smart Grid*, vol. 8, no. 6, pp. 2712–2722, 2017.

[55] V. L. Nguyen, T. Tran-Quoc, and S. Bacha, "Harmonic distortion mitigation for electric vehicle fast charging systems," *2013 IEEE Grenoble Conf. PowerTech, POWERTECH 2013*, pp. 1–6, 2013.

[56] J. P. A. E. Santo, R. Godina, E. M. G. Rodrigues, E. Pouresmaeil, and J. P. S. Catalao, "EV charging effect on a distribution transformer supplying a factory with local PV generation," *2017 IEEE Manchester PowerTech, Powertech 2017*, 2017.

[57] S. Sachan and N. Kishor, "A Probabilistic Approach for DG with Electric Vehicles," *2018 IEEE Int. Conf. Power Electron. Drives Energy Syst.*, no. i, pp. 1–4, 2019.

[58] T. Committee, I. Power, and E. Society, *IEEE Recommended Practice for Establishing Liquid-Filled and Dry-Type Power and Distribution Transformer Capability When Supplying Nonsinusoidal Load Currents*, vol. 2008, no. August. 2008.

[59] M. I. Samesima, J. Wilson Resende, and S. C. N. Araujo, "Analysis of transformer loss of life driving nonlinear industrial loads by the finite elements approach," pp. 2175–2179, 2002.

[60] IEEE, *IEEE Std C57.91^{TM}-2011 (Revision of IEEE Std C57.91-1995) Guide for Loading Mineral- Oil-Immersed Transformers and Step-Voltage Regulators*, vol. 2011, no. March. 2012.

[61] J. D. Glover, M. S. Sarma, and T. J. Overbye, *Power System Analysis & Design*, Fifth. .

[62] D. M. Said, K. M. Nor, and M. S. Majid, "Analysis of distribution transformer losses and life expectancy using measured harmonic data," *BT - 14th Int. Conf. Harmon. Qual. Power, ICHQP 2010*, pp. 0–5, 2010.

[63] D. Alame, M. A. Azzouz, and N. C. Kar, "Assessing the Impacts of Electric Vehicle Battery Charging on Distribution Transformers and on Distribution Systems," in *Proceedings of 2018 Energy & Sustainability Symposium*, 2018, pp. 1–8.

[64] J. Mullan, D. Harries, T. Bräunl, and S. Whitely, "Modelling the impacts of electric vehicle recharging on the Western Australian electricity supply system," *Energy Policy*, vol. 39, no. 7, pp. 4349–4359, 2011.

[65] S. Deb, K. Kalita, and P. Mahanta, "Impact of electric vehicle charging stations on reliability of distribution network," in *2017 International Conference on*

Technological Advancements in Power and Energy (TAP Energy), 2017, vol. 1, pp. 1–6.

[66]   H. Ramadan, A. Ali, and C. Farkas, "Assessment of plug-in electric vehicles charging impacts on residential low voltage distribution grid in Hungary," *Proc. - 2018 6th Int. Istanbul Smart Grids Cities Congr. Fair, ICSG 2018*, pp. 105–109, 2018.

[67]   M. Nour, H. Ramadan, A. Ali, and C. Farkas, "Impacts of plug-in electric vehicles charging on low voltage distribution network," *Proc. 2018 Int. Conf. Innov. Trends Comput. Eng. ITCE 2018*, vol. 2018-March, pp. 357–362, 2018.

[68]   V. Monteiro, H. Gonalves, J. C., and J. L., "Batteries Charging Systems for Electric and Plug-In Hybrid Electric Vehicles," *New Adv. Veh. Technol. Automot. Eng.*, pp. 149–168, 2012.

[69]   M. A. Azzouz, M. F. Shaaban, and E. F. El-Saadany, "Real-Time Optimal Voltage Regulation for Distribution Networks Incorporating High Penetration of PEVs," *IEEE Trans. Power Syst.*, vol. 30, no. 6, pp. 3234–3245, Nov. 2015.

[70]   M. F. Baran, "Network Reconfiguration in Distribution Systems for Loss Reduction and Load Balancing," *IEEE Trans. Power Deliv.*, vol. 4, pp. 1401–1407, 1989.

[71]   R. D. Zimmerman and C. E. Murillo-S´anchez, "MATPOWER 6.0 User ' S Manual," *PSerc*, no. December, pp. 1–47, 2016.

[72]   E. Society, "IEEE Std 519-2014 (Revision of IEEE Std 519-1992), IEEE Recommended Practice and Requirements for Harmonic Control in Electric Power Systems," *IEEE Std 519-2014 (Revision IEEE Std 519-1992)*, vol. 2014, pp. 1–29, 2014.

[73]   T. Hoevenaars, K. Ledoux, and M. Colosino, "Interpreting IEEE Std 519 and Meeting Its Harmonic Limits in VFD Applications," in *IEEE Industry Applications Society 50th Annual Petroleum and Chemical Industry Conference*, 2003, pp. 145–150.

[74]   "IEEE Recommended Practices and Requirements for Harmonic Control in Electric Power Systems, "IEEE std 519-1992," *Ieee*, pp. 1–9, 1992.

[75]   X. Hua, C. Yuxi, W. Jian, and V. Agelidis, "Design of energy dispatch strategy of active distribution network using chance-constrained programming," *Asia-Pacific Power Energy Eng. Conf. APPEEC*, vol. 2016-Janua, 2016.

[76]   G. Liu, R. Huang, T. Pu, and Z. Yang, "Design of energy management system for Active Distribution Network," *China Int. Conf. Electr. Distrib. CICED*, vol. 2014-Decem, no. Ciced, pp. 561–564, 2014.

[77]   S. Morris, Yun Seng Lim, and Jianhui Wong, "Self-intelligent active management system for electrical distribution networks with photovoltaic systems," no. Lv, pp. 2.06-2.06, 2013.

[78]   J. Lin *et al.*, "Situation awareness of active distribution network: Roadmap, technologies, and bottlenecks," *CSEE J. Power Energy Syst.*, vol. 2, no. 3, pp. 35–42, 2016.

[79]   Y. N. Bulatov, A. V. Kryukov, and N. Van Huan, "Automatic Prognostic Regulators of Distributed Generators," *2018 Int. Multi-Conference Ind. Eng. Mod. Technol. FarEastCon 2018*, pp. 1–4, 2019.

[80]   W. El-Khattam and M. M. A. Salama, "Distributed generation technologies, definitions and benefits," *Electr. Power Syst. Res.*, vol. 71, no. 2, pp. 119–128, 2004.

[81]   W. Shang and M. A. Redfern, "Control Schemes for Distributed Generators Connected to Distribution Networks," *44th Int. Univ. Power Eng. Conf.*, pp. 1–5, 2009.

[82]   R. E. Brown, Jiuping Pan, Xiaorning Feng, and K. Koutlev, "Siting distributed generation to defer T&D expansion," vol. 00, no. M, pp. 622–627, 2002.

[83]   P. Chiradeja and R. Ramakumar, "An approach to quantify the technical benefits of distributed generation," *IEEE Trans. Energy Convers.*, vol. 19, no. 4, pp. 764–773, 2004.

[84]   N. Shah and R. Chudamani, "Grid interactive PV system with harmonic and reactive power compensation features using a novel fuzzy logic based MPPT," *2012 IEEE 7th Int. Conf. Ind. Inf. Syst. ICIIS 2012*, vol. 1, pp. 1–6, 2012.

[85]   Y. K. Yeh, G. W. Chang, Y. J. Liu, T. K. Nguyen, Y. R. Chang, and Y. D. Lee, "A Study on Control Strategy of PV inverter for Harmonic Mitigation in A Microgrid," *IEEE Power Energy Soc. Gen. Meet.*, vol. 2018-Augus, no. 1, pp. 1–5, 2018.

[86]   F. Blaabjerg, R. Teodorescu, M. Liserre, and A. V. Timbus, "Overview of control and grid synchronization for distributed power generation systems," *IEEE Trans. Ind. Electron.*, vol. 53, no. 5, pp. 1398–1409, 2006.

[87]   S. Md. Munir and Y. W. Li, "Residential distribution system harmonic compensation using PV interfacing inverter," *IEEE Trans. Smart Grid*, vol. 4, no. 2, pp. 816–827, 2013.

[88]   E. Zangeneh Bighash, S. M. Sadeghzadeh, E. Ebrahimzadeh, and F. Blaabjerg, "Adaptive-harmonic compensation in residential distribution grid by roof-top PV Systems," *IEEE J. Emerg. Sel. Top. Power Electron.*, vol. 6, no. 4, pp. 2098–2108, 2018.

[89]   Ying-Yi Hong and Wei-Fen Huang, "Interactive multiobjective passive filter planning with fuzzy parameters in distribution systems using genetic algorithms," *IEEE Trans. Power Deliv.*, vol. 18, no. 3, pp. 1043–1050, 2003.

[90]   F. M. P. Pamplona and B. Souza, "Distribution Systems Using Genetic Algorithms," *IEEWPES Transm. iS Distrib. Conf. i% Expo. Lat. Am. Harmon.*, pp. 1–6, 2004.

[91] "What Is the Genetic Algorithm?" [Online]. Available: https://www.mathworks.com/help/gads/what-is-the-genetic-algorithm.html.

[92] R. Misra and S. Paudyal, "Analysis and reduction of total harmonic distortions in distribution system with electric vehicles and wind generators," *IEEE Power Energy Soc. Gen. Meet.*, vol. 2015-Septe, pp. 1–5, 2015.

[93] D. Kavitha, P. Renuga, and S. M. Priya, "Optimal placement and location of distributed generators in distorted distribution system," *2014 Int. Conf. Circuits, Power Comput. Technol. ICCPCT 2014*, pp. 533–539, 2014.

[94] "Fuzzy approach for optimal placement and sizing of capacitor banks in the presence of harmonics," *IEEE Trans. Power Deliv.*, vol. 19, no. 2, pp. 822–829, 2004.

[95] L. Motta and N. Faúndes, "Active / passive harmonic filters: Applications, challenges & trends," *Proc. Int. Conf. Harmon. Qual. Power, ICHQP*, vol. 2016-Decem, no. 1, pp. 657–662, 2016.

APPENDICES

Appendix A

TABLE A. 1. Bus Data for 33-bus Radial Distribution System.

Bus #	Type	Pd (kW)	Qd (kVAr)
1	3	0	0
2	1	100	60
3	1	90	40
4	1	120	80
5	1	60	30
6	1	60	20
7	1	200	100
8	1	200	100
9	1	60	20
10	1	60	20
11	1	45	30
12	1	60	35
13	1	60	35
14	1	120	80
15	1	60	10
16	1	60	20
17	1	60	20
18	1	90	40
19	1	90	40
20	1	90	40
21	1	90	40
22	1	90	40
23	1	90	50
24	1	420	200
25	1	420	200
26	1	60	25
27	1	60	25
28	1	60	20
29	1	120	70
30	1	200	600
31	1	150	70
32	1	210	100
33	1	60	40

Buses are classified into three types in power systems: PQ bus, PV bus and Slack bus. PQ bus is known as Load Bus in which the real power and reactive power are given. PV bus is known as Generator Bus in which the real power and the voltage magnitude are specified. Slack bus, also known as Reference or Swing Bus, is used to balance the active and reactive power in the system. Its voltage magnitude is taken as 1 p.u. In Table A.1, all of the buses

are of type 1, except for bus #1. Type 1 refers to PQ bus that are used to find the bus voltage and angle. Bus #1 is of Type 3, denoting that is a slack bus that serves as an angular reference for all other buses in the system.

TABLE A. 2. Branch Data for 33-bus Radial Distribution System.

Branch #	From bus #	To bus #	R (ohms)	x (ohms)
1	1	2	0.0922	0.0470
2	2	3	0.4930	0.2511
3	3	4	0.3660	0.1864
4	4	5	0.3811	0.1941
5	5	6	0.8190	0.7070
6	6	7	0.1872	0.6188
7	7	8	0.7114	0.2351
8	8	9	1.0300	0.7400
9	9	10	1.0440	0.7400
10	10	11	0.1966	0.0650
11	11	12	0.3744	0.1238
12	12	13	1.4680	1.1550
13	13	14	0.5416	0.7129
14	14	15	0.5910	0.5260
15	15	16	0.7463	0.5450
16	16	17	1.2890	1.7210
17	17	18	0.7320	0.5740
18	2	19	0.1640	0.1565
19	19	20	1.5042	1.3554
20	20	21	0.4095	0.4784
21	21	22	0.7089	0.9373
22	3	23	0.4512	0.3083
23	23	24	0.8980	0.7091
24	24	25	0.8960	0.7011
25	6	26	0.2030	0.1034
26	26	27	0.2842	0.1447
27	27	28	1.0590	0.9337
28	28	29	0.8042	0.7006
29	29	30	0.5075	0.2585
30	30	31	0.9744	0.9630
31	31	32	0.3105	0.3619
32	32	33	0.3410	0.5302
33	21	8	2.0000	2.0000
34	9	15	2.0000	2.0000
35	12	22	2.0000	2.0000
36	18	33	0.5000	0.5000
37	25	29	0.5000	0.5000

Appendix B
Permission for using IEEE publications

Copyright Clearance Center **RightsLink®**

IEEE Requesting permission to reuse content from an IEEE publication

Title:	Impact Assessment of Electric Vehicle Charging on Distribution Transformers Including State-of-Charge
Conference Proceedings:	2018 IEEE 61st International Midwest Symposium on Circuits and Systems (MWSCAS)
Author:	Dima Alame
Publisher:	IEEE
Date:	Aug. 2018

Copyright © 2018, IEEE

Thesis / Dissertation Reuse

The IEEE does not require individuals working on a thesis to obtain a formal reuse license, however, you may print out this statement to be used as a permission grant:

Requirements to be followed when using any portion (e.g., figure, graph, table, or textual material) of an IEEE copyrighted paper in a thesis:

1) In the case of textual material (e.g., using short quotes or referring to the work within these papers) users must give full credit to the original source (author, paper, publication) followed by the IEEE copyright line © 2011 IEEE.
2) In the case of illustrations or tabular material, we require that the copyright line © [Year of original publication] IEEE appear prominently with each reprinted figure and/or table.
3) If a substantial portion of the original paper is to be used, and if you are not the senior author, also obtain the senior author's approval.

Requirements to be followed when using an entire IEEE copyrighted paper in a thesis:

1) The following IEEE copyright/ credit notice should be placed prominently in the references: © [year of original publication] IEEE. Reprinted, with permission, from [author names, paper title, IEEE publication title, and month/year of publication]
2) Only the accepted version of an IEEE copyrighted paper can be used when posting the paper or your thesis on-line.
3) In placing the thesis on the author's university website, please display the following message in a prominent place on the website: In reference to IEEE copyrighted material which is used with permission in this thesis, the IEEE does not endorse any of [university/educational entity's name goes here]'s products or services. Internal or personal use of this material is permitted. If interested in reprinting/republishing IEEE copyrighted material for advertising or promotional purposes or for creating new collective works for resale or redistribution, please go to http://www.ieee.org/publications_standards/publications/rights/rights_link.html to learn how to obtain a License from RightsLink.

If applicable, University Microfilms and/or ProQuest Library, or the Archives of Canada may supply single copies of the dissertation.

BACK   CLOSE WINDOW

VITA AUCTORIS

NAME: Dima Alame

PLACE OF BIRTH: Windsor, ON

YEAR OF BIRTH: 1994

EDUCATION: Ecole secondaire E.J. Lajeunesse, Windsor, ON,
                                 2012

                                 University of Windsor, B.Sc., Windsor, ON, 2016

                                 University of Windsor, M.Sc., Windsor, ON, 2019